



KTH Engineering Sciences

Master Thesis

A Monte Carlo Approach to Feynman Diagrammatic Series and its Boldification

Emil Blomquist

Statistical Physics Group, Department of Physics,
School of Engineering Sciences
Royal Institute of Technology, SE-106 91 Stockholm, Sweden

Stockholm, Sweden 2017

Typeset in L^AT_EX

TRITA-???
ISSN ???
ISRN ???

© Emil Blomquist, September 2017
Printed in Sweden by Universitetsservice US AB, Stockholm September 2017

Abstract

The single-particle temperature Green's function of the Fröhlich polaron is simulated at zero temperature using three different types of diagrammatic Monte Carlo schemes. Using bare schemes both the Green's function and the corresponding proper self-energy are simulated. The Green's function obtained through Dyson equation from the proper self-energy is then observed to be consistent with the directly simulated Green's function. A bold-line scheme simulation is also carried out, the results of which are in close agreement with what was obtained from the bare scheme simulations. Complications due to noise prone statistics are discussed and an improvement is suggested. Finally the ground state energy E_0 and the Z_0 -factor of the polaron are extracted through the asymptotic behavior of the Green's function.

Sammanfattning

Temperaturgreenfunktionen av en Fröhlichpolaron simuleras vid noll grader Kelvin med hjälp av tre olika varianter av diagrammatisk Monte Carlo. Genom *bar*-typ simulering beräknas både Greenfunktionen samt dess motsvarande självenergi. Greenfunktionen som erhålls från denna självenergi visas sedan, genom användandet av Dysons ekvation, överensstämma med den direkt simulerade. Även en så kallad *klädd*-typ simulering utförs och resultaten från denna visas vara i god överensstämmelse med resultaten från de tidigare nämnda simuleringarna. Svårigheter med brus i statistiken diskuteras och en förbättring föreslås. Slutligen beräknas polaronens grundtillståndsenergi E_0 samt Z_0 -faktorn genom det asymptotiska beteendet hos Greenfunktionen.

Preface

This thesis is the result of 10 months of work between December 2016 and September 2017, for the degree of Master of Science in Engineering, in the Physics Department of KTH Royal Institute of Technology, Sweden.

Acknowledgements

I would like to thank my supervisor Prof. Egor Babaev for giving me the opportunity to carry out my degree project in the Statistical Physics group. Your encouragement and support have been greatly appreciated, as well as your patience for results from my, sometimes extremely bug prone, code. I would also like to extend my deepest gratitude to Johan Carlström who, as an expert in the field, has provided excellent guidance throughout the project. Furthermore I would like to thank Prof. Nikolay Prokof'ev from University of Massachusetts Amherst for helping me sort out problems no one else was able to. Last but not least I would like to express my gratitude towards my fellow master degree students as well as to my soon-to-be fellow Ph.D students at the Physics Department for helping me with various issues.

Units

Throughout this text $k_B = \hbar = 1$ has been used. With this notation there is no difference between wave vectors and momentum, which is the reason why they are sometimes used interchangeably.

Definitions

At a few instances the symbol Δ appears. This is an invented shorthand notation defined as $\Delta x \equiv \Delta x/2$ used to make certain expressions appear less cluttered.

Contents

Abstract	iii
Sammanfattning	iii
Preface	v
Contents	vii
1 Introduction	1
2 Background material	3
2.1 Quantum field theories	3
2.1.1 Single- and many-particle quantum mechanics	3
2.1.2 Second-quantization	4
2.1.3 Field operators	5
2.2 A few words on finite temperature formalism	5
2.2.1 Green's function	6
2.2.2 Bare single-particle Green's function	9
2.3 Derivation of the Fröhlich Hamiltonian	9
2.3.1 Classical picture	10
2.3.2 Quantization	15
2.4 Perturbation theory	18
2.4.1 Diagrammatic analysis	19
2.4.2 Dyson equation	23
2.5 Monte Carlo Methods	26
2.5.1 Markov processes, detailed balance and ergodicity	26
2.5.2 Metropolis-Hastings algorithm	27
3 Diagrammatic Monte Carlo	29
3.1 General idea	29
3.2 Bare scheme for simulating \mathcal{G}	34
3.2.1 Implementation	35
3.2.2 Update procedures	36
3.2.3 Results	44

3.3	Bare scheme for simulating Σ^*	48
3.3.1	Update procedures	48
3.3.2	The divergent diagram	50
3.3.3	Results	52
3.3.4	Numerically implementing Dyson equation	54
3.4	Bold-line scheme	56
3.4.1	Skeleton diagrams	57
3.4.2	Implementation and update procedures	60
3.4.3	Results	61
3.5	Numerical Results of E_0 and Z_0	73
4	Summary and conclusions	77
	Bibliography	79

Chapter 1

Introduction

A piece of solid material, small enough to fit in the palm of a hand, contains of the order of 10^{23} particles. It is obvious that these particles interact with one another, if not they would simply start roaming about and the solid would disintegrate. The theoretical treatment of interactions between such a humongous number of particles belongs to the field of many-body physics. In order to accurately model the interplay between so many particles, a quantum mechanical framework referred to as quantum field theory is used. The collective behavior of particles is then described, in a quantum mechanical setting, as quasiparticles. Like the name suggests, a quasiparticle is not a fundamental particle, but rather an emergent phenomenon with similarities to a particle. An example would be the collective excitation associated with vibrations of atoms in a lattice structure which is nothing but a quantum of a sound wave, known as a phonon.

There exist several other quasiparticles besides the phonon, one of which is the polaron [1]. This quasiparticle describes the dynamic which comes about when an electron interacts with the polarization in its surroundings. One particular scenario is that of a low energy electron brought into a continuously modeled ionic crystal. This situation is described by the Fröhlich Hamiltonian [2–4] and the resulting polaron is appropriately referred to as the (large) Fröhlich polaron. When propagating through the crystal, the introduced electron will still behave as if it were free, but with an enhanced effective mass due to it being accompanied by the surrounding polarization. Since the polarization arises due to deformations of the lattice, which in turn may be described by phonons, one could say that the electron is dressed in a cloud of phonons. This collective behavior of the electron together with the phonon cloud is what constitutes the Fröhlich polaron.

For a long time properties of quasiparticles have been calculated analytically using perturbation theory. This is an extremely time-consuming process which is not guaranteed to work in all circumstances. Fortunately however, today there exist computer intensive methods for calculating properties of the quasiparticles. One such method is the diagrammatic Monte Carlo (DMC) method developed by

Prokof'ev et al. [5] which has proved to be successful [6–9]. This is a Metropolis-Hastings based Monte Carlo method which performs a random walk between Feynman diagrams of a perturbation series in order to simulate the quantity this series represents.

In particular, the DMC method could be implemented to calculate the electronic single-particle Green's function of the Fröhlich Hamiltonian from which quantities of the polaron then might be extracted. Perhaps not so surprisingly to the reader, this is exactly what is investigated in this thesis. Three different variants, two bare schemes and one bold-line scheme, are implemented in a self made c++ program and the result obtained is presented in this thesis. Without further ado, let's jump into all the technicalities!

Chapter 2

Background material

First up in this chapter is a brief summary of quantum field theories, both at zero and finite temperature, followed by a rather detailed derivation of the Fröhlich Hamiltonian. After this follows an illustration of how one can treat an interacting theory perturbatively in terms of pictorial Feynman diagrams. Finally there will be a short introduction to Monte Carlo methods.

2.1 Quantum field theories

2.1.1 Single- and many-particle quantum mechanics

In quantum mechanics the state of a particle $|\psi\rangle$ can be projected onto the position basis $|\mathbf{x}\rangle$ to form a wave function $\langle\mathbf{x}|\psi\rangle = \psi(\mathbf{x})$. In the Schrödinger picture, the dynamics is contained within the states $|\psi\rangle = |\psi(t)\rangle$ so that $\psi(\mathbf{x}) = \psi(\mathbf{x}, t)$ the time evolution of which is governed by the Schrödinger equation (in the non-relativistic limit). The quantity $\psi^*(\mathbf{x}, t)\psi(\mathbf{x}, t)$ is real, and according to the Copenhagen interpretation of quantum mechanics [10] it is to be interpreted as the probability density function. From this, the expectation value of some quantity, e.g. the position of the particle, is acquired through

$$\begin{aligned}\langle\mathbf{x}(t)\rangle &= \int \mathbf{x} \psi^*(\mathbf{x}, t) \psi(\mathbf{x}, t) d^3x \\ &= \int \mathbf{x} \langle\psi(t)|\mathbf{x}\rangle \langle\mathbf{x}|\psi(t)\rangle d^3x \\ &= \langle\psi(t)| \left[\int \mathbf{x} |\mathbf{x}\rangle \langle\mathbf{x}| d^3x \right] |\psi(t)\rangle \\ &= \langle\psi(t)| \hat{\mathbf{x}} \left[\int |\mathbf{x}\rangle \langle\mathbf{x}| d^3x \right] |\psi(t)\rangle \\ &= \langle\psi(t)| \hat{\mathbf{x}} |\psi(t)\rangle.\end{aligned}\tag{2.1}$$

To reach the final equality utilization has been made of the fact that the position basis is an eigenbasis of the position operator $\hat{\mathbf{x}}|\mathbf{x}\rangle = \mathbf{x}|\mathbf{x}\rangle$ and also that this basis is orthonormal and complete so that the unity operator may be expressed as $\hat{1} = \sum_{\mathbf{x}} |\mathbf{x}\rangle\langle\mathbf{x}|$.

What has been described so far is a quantum mechanical system of a single particle. In order to describe a system of more than one particle, this formalism need to be generalized to a many-particle description. When doing this, attention needs to be paid to the statistics of indistinguishable particles. That is, the state of the entire system must be symmetric with respect to the interchange of two indistinguishable bosons and antisymmetric to the interchange of two indistinguishable fermions. In the many-particle quantum mechanics formalism, this can be rather cumbersome even when dealing with a noninteracting system. Another shortcoming with this description of quantum mechanics is that the number of particles of each species must be fixed. Hence it is not possible to have particle creation or particle annihilation, which is necessary for certain processes.

2.1.2 Second-quantization

The second quantization [11, 12] is a Hamiltonian based method for constructing a quantum field theory. Such a theory does not have the shortcomings of having a fixed set of particles as in the case of the many-particle description of quantum mechanics.

Again the state of the total system will be described by individual single-particle states. However, instead of having explicit all the permutations of the indistinguishable single-particle states in order to incorporate the statistics, the total system state will now be expressed using occupation numbers. That is, in this representation the only information given is for each species of particle, what number of particles occupies which states. For example, given the following set of single-particle states $\{|\nu_i\rangle\}$ where $i = 0, 1, 2, \dots$, the expression describing a state in which $|\nu_0\rangle$ and $|\nu_2\rangle$ are occupied by three and two particles respectively would then be $|3, 0, 0, 2, 0, 0, \dots\rangle$.

In order to allow for the number of particles to be variable the Fock space is used. This space is a combination of Hilbert state spaces for any number of particles; from the empty vacuum state to a state with infinite particles. In order to create and annihilate a particle of a certain quantum number, creation \hat{c}_ν^\dagger and annihilation \hat{c}_ν operators are used. It can be shown that they are the Hermitian conjugates of one another which motivates the notation. These operators incorporate the underlying statistics of the particle at hand by a set of commutation relations. For bosons they are

$$[\hat{a}_i, \hat{a}_j^\dagger] = \delta_{ij}, \quad [\hat{a}_i, \hat{a}_j] = [\hat{a}_i^\dagger, \hat{a}_j^\dagger] = 0. \quad (2.2)$$

These commutation relations are, for each single-particle state, identical to those of the ladder operators of a harmonic oscillator. For fermions the commutation relations are identical, but the commutator is exchanged in favor of the anticommutator

in order to make the state antisymmetric, i.e.

$$\{\hat{b}_i, \hat{b}_j^\dagger\} = \delta_{ij}, \quad \{\hat{b}_i, \hat{b}_j\} = \{\hat{b}_i^\dagger, \hat{b}_j^\dagger\} = 0. \quad (2.3)$$

The second-quantized Hamiltonian may be constructed by translating single- and many-particle quantum mechanical operators into the second-quantized description. In the case of a one-body operator this translation is rather intuitive. Here the second-quantization operator \hat{O} is given by [11]

$$\hat{O} = \sum_{\mu, \nu} \langle \mu | O | \nu \rangle \hat{c}_\mu^\dagger \hat{c}_\nu, \quad (2.4)$$

where O is the first-quantized operator, μ and ν are quantum numbers labeling the set of orthonormal single-particle states $\{|\mu\rangle\}$ and $\hat{c}_\mu^\dagger, \hat{c}_\mu$ being the corresponding second-quantized creation and annihilation operators.

2.1.3 Field operators

When having utilized the second-quantization formalism, the quantum mechanical system is described by a quantum field. That is, rather than being an operator as in single- and many-particle quantum mechanics, the position is now a parameter, just like time.

Field operators are creation and annihilation operators just like any other. They have gained their special name simply because they change the occupation number of single-particle eigenstates of the position operator. That is, they create or annihilate a particle at a particular position in space. Using the set of complete orthonormal single-particle wave functions $\{\psi_\nu(\mathbf{x})\}$ along with the corresponding creation and annihilation operators $\hat{c}_\nu^\dagger, \hat{c}_\nu$, these field operators may be constructed by the following superpositions [11],

$$\hat{\psi}(\mathbf{x}) \equiv \sum_\nu \hat{c}_\nu \psi_\nu(\mathbf{x}), \quad \hat{\psi}^\dagger(\mathbf{x}) \equiv \sum_\nu \hat{c}_\nu^\dagger \psi_\nu^*(\mathbf{x}). \quad (2.5)$$

The $\hat{\psi}(\mathbf{x})$ will annihilate a particle at position \mathbf{x} whilst the Hermitian conjugate $\hat{\psi}^\dagger(\mathbf{x})$ will do the opposite and create a particle at position \mathbf{x} .

2.2 A few words on finite temperature formalism

In a zero temperature quantum field theory, the Heisenberg picture is normally used when calculating observables, i.e. $O = \langle \Psi_0 | \hat{O}_H | \Psi_0 \rangle$. In this picture the operators are responsible for the time evolution of the observables whilst the state vectors are made time independent. This is achieved by letting the time evolution of the Schrödinger state vector $|\Psi_0(t)\rangle = e^{-i\hat{H}t} |\Psi_0\rangle$ be absorbed into the Heisenberg operator $\hat{O}_H(t) \equiv e^{i\hat{H}t} \hat{O}_S e^{-i\hat{H}t}$. Since the temperature $T = 0$ in such a theory,

one does not need to be concerned about thermodynamics when calculating an observable, even if the ground state is not the vacuum one.

For a finite temperature quantum field theory and a general system, this no longer holds true. In order to incorporate the thermodynamics, the observables are no longer calculated by the expectation value of merely one ground state but instead as an ensemble average. In the case of a system with a variable number of particles, the grand canonical ensemble should be used. The partition function is then given by $Z_G = \text{Tr} e^{-\beta(\hat{H} - \mu\hat{N})} = \text{Tr} e^{-\beta\hat{K}}$ where β is the inverse temperature, \hat{H} is the Hamiltonian, \hat{N} is the number operator, μ is the chemical potential and the trace is taken over a complete set of states. Introduced was also the grand canonical Hamiltonian $\hat{K} \equiv \hat{H} - \mu\hat{N}$. In accordance with the partition function, the statistical operator is then defined as $\hat{\rho}_G = e^{-\beta\hat{K}}/Z_G$ so that

$$O = \sum_{\nu} \langle \Psi_{\nu} | \hat{\rho}_G \hat{O}_H | \Psi_{\nu} \rangle \equiv \text{Tr} \{ \hat{\rho}_G \hat{O}_H(t) \}. \quad (2.6)$$

The operator product sandwiched between the state vectors in the equation above contains both real and imaginary exponents originating from the thermodynamics and quantum mechanics respectively. Following the Matsubara formalism [11–13], one proceeds by introducing a new picture in order to treat the two types of exponents on an equal footing. This is a modified Heisenberg picture where a Wick rotation in time $\tau = it$ is preformed, and the Hamiltonian is exchanged in favor of the grand canonical Hamiltonian. An operator in this picture is then related to the corresponding one in the Schrödinger picture as

$$\hat{O}_K(\tau) \equiv e^{\hat{K}\tau} \hat{O}_S e^{-\hat{K}\tau}. \quad (2.7)$$

2.2.1 Green's function

The single-particle Green's function, also known as the propagator, plays a crucial role in quantum field theory. At zero temperature, in position and time representation, the single-particle Green's function is defined as

$$iG_{\alpha\beta}(x, x') \equiv \frac{\langle \Psi_0 | T[\hat{\psi}_{H\alpha}(x) \hat{\psi}_{H\beta}^{\dagger}(x')] | \Psi_0 \rangle}{\langle \Psi_0 | \Psi_0 \rangle} \quad (2.8)$$

and gives the probability amplitude of a particle traveling from one point in space and time to another one. Here $|\Psi_0\rangle$ is the ground state vector in the Heisenberg picture, $\hat{\psi}_{H\alpha}(x)$ is the α -th component of a field operator also in the Heisenberg picture, $T[\dots]$ orders the operators according to their time while x and x' are position-time four-vectors. This Green's function contains observable properties such as the ground state energy and the excitation spectrum of the system. Using the Lehman representation, the expectation value of any single-particle operator in the ground state of the system might also be extracted.

Above zero temperature, now working with an imaginary time τ , the Green's function of interest is the temperature Green's function. In the imaginary time and position representation, the corresponding single-particle temperature Green's function is defined through

$$\mathcal{G}_{\alpha\beta}(x, x') \equiv \text{Tr}\{\hat{\rho}_G T_\tau[\hat{\psi}_{K\alpha}(x)\hat{\psi}_{K\alpha}^\dagger(x')]\}. \quad (2.9)$$

Here $\psi_{K\alpha}(x)$ is the α -th component of a field operator in the modified Heisenberg picture, $T_\tau[\dots]$ orders the operators according to their value of τ , $\text{Tr}\{\rho_G \dots\}$ is the same weighted sum of inner products as mentioned before while x and x' are position-imaginary time four-vectors. Since the temperature single-particle Green's function is not a function of time, it is only possible to directly extract from it observables which do not depend on time, that is, thermodynamic observables. In order to obtain time dependent properties, one must first relate the temperature Green's function to a real-time Green's function. This is something which will not be of importance to this thesis and thus will not be discussed any further. From here on only the finite temperature formalism will be considered and whenever a Green's function is mentioned it will be understood that the single-particle temperature Green's function is the one that is referred to.

Assuming the Hamiltonian is time independent and translationally invariant, the Green's function will depend only on the difference $\mathbf{x} - \mathbf{x}'$ and $\tau - \tau'$ as soon shall be shown. By further imposing spin independency onto the Hamiltonian, the spin dependency of the Green's function may be factored out as $\mathcal{G}_{\alpha\beta}(\mathbf{x} - \mathbf{x}', \tau - \tau') = \delta_{\alpha\beta} \mathcal{G}(\mathbf{x} - \mathbf{x}', \tau - \tau')$. Thus, from this point and forward, when referring to a Green's function the spin dependency will be omitted.

In the case of a cubic system with a finite volume $V = l^3$, accompanied by periodic boundary conditions, the single-particle wave functions

$$\psi_{\mathbf{k}}(\mathbf{x}) = \frac{e^{i\mathbf{k}\cdot\mathbf{x}}}{\sqrt{V}} \quad (2.10)$$

correspond to eigenstates of the momentum operator with eigenvalues given by

$$k_i = \frac{2\pi}{l} n_i; \quad n_i = 0, \pm 1, \pm 2, \dots \quad (2.11)$$

Constructing the field operators (2.5) in terms of these, the expression for the Green's function may be transformed as

$$\begin{aligned} \mathcal{G}(\mathbf{x} - \mathbf{x}', \tau - \tau') &= \sum_{\mathbf{k}, \mathbf{p}} \psi_{\mathbf{k}}(\mathbf{x}) \psi_{\mathbf{p}}^*(\mathbf{x}') \text{Tr}\{\hat{\rho}_G T_\tau[\hat{c}_{\mathbf{k}}(\tau) \hat{c}_{\mathbf{p}}^\dagger(\tau')]\} \\ &= \sum_{\mathbf{k}, \mathbf{p}} \psi_{\mathbf{k}}(\mathbf{x}) \psi_{\mathbf{p}}^*(\mathbf{x}') \delta_{\mathbf{k}, \mathbf{p}} \text{Tr}\{\hat{\rho}_G T_\tau[\hat{c}_{\mathbf{k}}(\tau - \tau') \hat{c}_{\mathbf{k}}^\dagger(0)]\} \\ &= \frac{1}{V} \sum_{\mathbf{k}} e^{i\mathbf{k}\cdot(\mathbf{x} - \mathbf{x}')} \text{Tr}\{\hat{\rho}_G T_\tau[\hat{c}_{\mathbf{k}}(\tau - \tau') \hat{c}_{\mathbf{k}}^\dagger(0)]\} \\ &= \int \frac{d^3k}{(2\pi)^3} e^{i\mathbf{k}\cdot(\mathbf{x} - \mathbf{x}')} \text{Tr}\{\hat{\rho}_G T_\tau[\hat{c}(\mathbf{k}, \tau - \tau') \hat{c}^\dagger(\mathbf{k}, 0)]\}, \end{aligned} \quad (2.12)$$

where in the last equality the limit $l \rightarrow \infty$ has been taken. In order to shift the time, the hermiticity of \hat{K} allowed for the trace to be expressed in terms of its complete set of eigenstates $\{|\nu_{\mathbf{k}}\rangle\}$. Then, since the Hamiltonian is time independent it will commute with itself at any two given times, implying that $\exp\{\hat{K}\tau - \hat{K}\tau'\} = \exp\{\hat{K}\tau\}\exp\{-\hat{K}\tau'\}$. On the other hand, in the limit of an infinite system, the Green's function in momentum space is obtained through the Fourier transform

$$\mathcal{G}(\mathbf{x}, \tau) = \int \frac{d^3k}{(2\pi)^3} e^{i\mathbf{k}\cdot\mathbf{x}} \mathcal{G}(\mathbf{k}, \tau). \quad (2.13)$$

Hence it must be the case that

$$\mathcal{G}(\mathbf{k}, \tau) = \text{Tr}\{\hat{\rho}_{\text{G}} T_{\tau}[\hat{c}(\mathbf{k}, \tau)\hat{c}^{\dagger}(\mathbf{k}, 0)]\}. \quad (2.14)$$

Assuming the ground state ensemble to be the vacuum state, i.e. $\text{Tr}\{\hat{\rho}_{\text{G}} \cdots\} \rightarrow \langle \text{vac} | \cdots | \text{vac} \rangle$, this expression further simplifies into

$$\mathcal{G}(\mathbf{k}, \tau) = \langle \text{vac} | \hat{c}(\mathbf{k}, \tau) \hat{c}^{\dagger}(\mathbf{k}, 0) | \text{vac} \rangle, \quad \tau \geq 0 \quad (2.15)$$

and is for all other imaginary times identically zero.

In order to demonstrate some important properties of $\mathcal{G}(\mathbf{k}, \tau)$ the unity operator $\hat{\mathbb{1}} = \sum_{\nu} |\nu\rangle\langle\nu|$, constructed in terms of the complete set of eigenstates $\{|\nu(\mathbf{k})\rangle\}$ of the grand canonical Hamiltonian $\hat{K} |\nu(\mathbf{p})\rangle = \xi_{\nu}(\mathbf{p}) |\nu(\mathbf{p})\rangle$, is inserted into expression (2.15). By recalling that the annihilation operator in the modified Heisenberg picture (2.7) is given by $\hat{c}_{\mathbf{k}}(\tau) = e^{\hat{K}\tau} \hat{c}_{\mathbf{k}}(0) e^{-\hat{K}\tau}$ the expression then boils down to [5]

$$\mathcal{G}(\mathbf{k}, \tau) = \sum_{\nu} |\langle \nu | \hat{c}_{\mathbf{k}}^{\dagger} | \text{vac} \rangle|^2 e^{-(\xi_{\nu} - \xi_{\text{vac}})\tau}, \quad \tau \geq 0. \quad (2.16)$$

Here it has been used that ξ_{vac} is the vacuum energy, i.e. $\hat{K} |\text{vac}\rangle = \xi_{\text{vac}} |\text{vac}\rangle$. For the Fröhlich Hamiltonian to be considered later, $\xi_{\text{vac}} = 0$ and will therefore be ignored in the remaining calculation. Rather than working with some unknown set $\{\nu\}$, it is more convenient to parametrize using the frequency. This is done by introducing the spectral density function

$$g_{\mathbf{k}}(\omega) \equiv \sum_{\nu} \delta(\omega - \xi_{\nu}) |\langle \nu | \hat{c}_{\mathbf{k}}^{\dagger} | \text{vac} \rangle|^2, \quad (2.17)$$

through which the single-particle Green's function is expressed as

$$\mathcal{G}(\mathbf{k}, \tau) = \int g_{\mathbf{k}}(\omega) e^{-\omega\tau} d\omega, \quad \tau \geq 0. \quad (2.18)$$

Assuming the Green's function to be that of an electron ($\hat{c}_{\mathbf{k}} \rightarrow \hat{a}_{\mathbf{k}}$), the factor $|\langle \nu | \hat{a}_{\mathbf{k}}^{\dagger} | \text{vac} \rangle|^2 = |\langle \nu | \mathbf{k} \rangle|^2$ is nothing more than the overlap of the eigenstate $|\nu\rangle$ with the free electron state of momentum \mathbf{k} . If there exist a stable eigenstate $|\nu_{0,\mathbf{k}}\rangle$ with

energy $\xi_0(\mathbf{k})$, the spectral function should contain the term $|\langle \nu_{0,\mathbf{k}} | \mathbf{k} \rangle|^2 \delta(\omega - \xi_0(\mathbf{k}))$. Being a stable state, the energy $\xi_0(\mathbf{k})$ is lower than the corresponding energy of any other possible eigenstate. According to (2.18), at imaginary times $\tau \rightarrow \infty$, the sole contribution to the single-particle Green's function should come from this stable state. That is,

$$\mathcal{G}(\mathbf{k}, \tau \rightarrow \infty) = Z_0(\mathbf{k}) e^{-\xi_0(\mathbf{k})\tau}, \quad (2.19)$$

where $Z_0(\mathbf{k}) = |\langle \nu_{0,\mathbf{k}} | \mathbf{k} \rangle|^2$ is the bare-electron factor. The corresponding energy eigenvalue E_0 of the Hamiltonian \hat{H} is according to the definition of the grand canonical Hamiltonian given by

$$E_0(\mathbf{k}) = \xi_0(\mathbf{k}) + \mu. \quad (2.20)$$

This because there is only one electron present in the system in the case of a single particle Green's function. Finally, since \hat{H} is independent of μ , this must also be true for E_0 , which is the reason for this energy later being investigated rather than ξ_0 .

2.2.2 Bare single-particle Green's function

— Continue here —

An eigenstate to a bare Hamiltonian, e.g. $\hat{K}_0 = \sum_{\mathbf{k}} \xi_{\mathbf{k}}^0 \hat{c}_{\mathbf{k}}^\dagger \hat{c}_{\mathbf{k}}$, is referred to as a bare or a free state. The energies $\xi_{\mathbf{k}}^0$ are known from solving the corresponding problem in first-quantization. Reusing the previous assumptions and calculations, but \hat{K} every where replaced with \hat{K}_0 , the bare Green's function in momentum space is found to be,

$$\mathcal{G}^{(0)}(\mathbf{k}, \tau) = \sum_{\mathbf{p}} |\langle \mathbf{p} | \hat{c}_{\mathbf{k}}^\dagger | \text{vac} \rangle|^2 e^{-\xi_{\mathbf{p}}^0 \tau} \quad \tau \geq 0. \quad (2.21)$$

However, this time the eigenstates are known, and using their orthonormality, the expression of the bare single-particle Green's function simplifies to

$$\mathcal{G}^{(0)}(\mathbf{k}, \tau) = e^{-\xi^0(\mathbf{k})\tau} \quad \tau \geq 0 \quad (2.22)$$

in the limit of an infinite system.

2.3 Derivation of the Fröhlich Hamiltonian

What will happen to a dielectric medium if one introduces a charged particle, and how will this particle react to changes in the dielectric medium? These are questions which Herbert Fröhlich answered in his 1954 paper *Electrons in lattice fields* [2]. In this section the original derivation will be outlined with attention directed towards details important for the thesis.

2.3.1 Classical picture

Consider a diatomic crystal, e.g. rock salt. Such a crystal is made up out of ions which pairwise have a zero net charge as illustrated in figure 2.1. By introducing a free electron into such a crystal, the crystal will become polarized due to the electric field exerted by the electron. The polarization is then described by a set of displacement vectors, one for each lattice point. In order to simplify what follows this set of displacement vectors are treated as a continuous vector field.

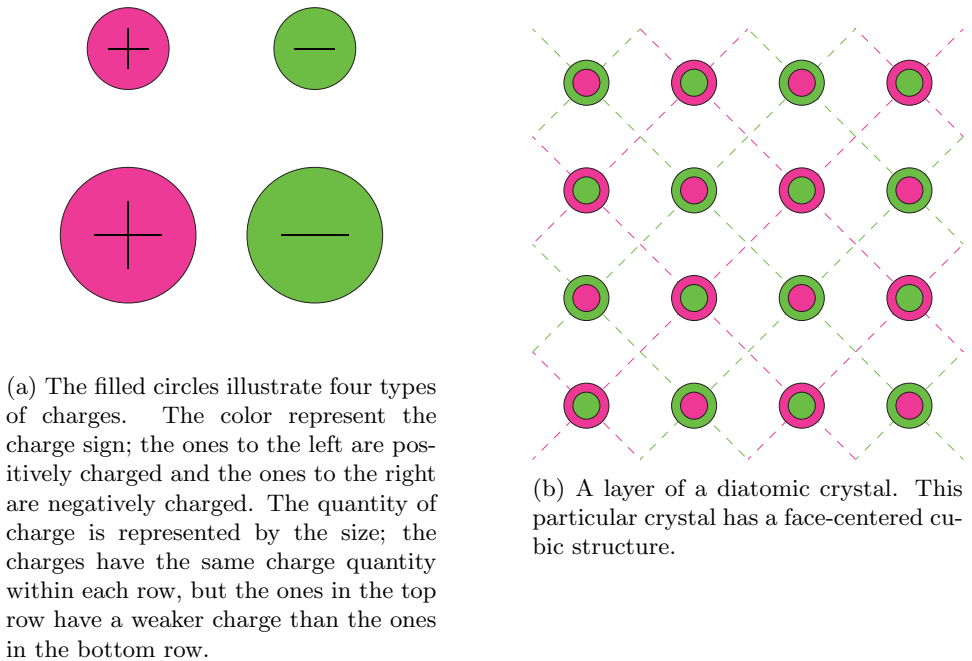


Figure 2.1

If this system is first looked at in a steady state situation, the polarization is determined solely by the dielectric permittivity ϵ_r . A handy quantity is the electric displacement field (CGS units)

$$\mathbf{D} = \mathbf{E} + 4\pi\mathbf{P} = \epsilon\mathbf{E} \quad (2.23)$$

where \mathbf{E} is the total electric field, \mathbf{P} is the polarization and $\epsilon = \epsilon_r\epsilon_0$ is the permittivity. Since the source of this field is given solely by the free electron, it may

be thought of as an external electrical field. If the electron is at position \mathbf{x}_e , the \mathbf{D} -field at a position \mathbf{x} is given by the familiar expression

$$\mathbf{D}(\mathbf{x}, \mathbf{x}_e) = -\nabla \frac{Q}{|\mathbf{x} - \mathbf{x}_e|}, \quad (2.24)$$

so that

$$\nabla \cdot \mathbf{D}(\mathbf{x}, \mathbf{x}_e) = 4\pi q \delta(\mathbf{x} - \mathbf{x}_e). \quad (2.25)$$

Here Q is the charge of the electron and the second equality is to be thought of as valid only as a distribution. In agreement with the definition of the \mathbf{D} -field the electric field due to the bound charges is defined as $\mathbf{E}_{\text{bound}} = -4\pi\mathbf{P}$ since $\mathbf{D} = \mathbf{E} + 4\pi\mathbf{P} = \mathbf{E} - \mathbf{E}_{\text{bound}} \equiv \mathbf{E}_{\text{free}}$.

The interaction energy, which is minimized when the \mathbf{D} -field is parallel to the polarization, is given by

$$E_{\text{int}} = -\int_V \mathbf{D}(\mathbf{x}, \mathbf{x}_e) \cdot \mathbf{P}(\mathbf{x}) d^3x. \quad (2.26)$$

Introducing a scalar potential to the bound electric field, $\mathbf{E}_{\text{bound}} = -\nabla\Phi$, this interaction energy may be re-expressed as

$$\begin{aligned} E_{\text{int}} &= -\frac{1}{4\pi} \int_{\Omega} \mathbf{D}(\mathbf{x}, \mathbf{x}_e) \cdot \nabla\Phi(\mathbf{x}) d^3x \\ &= -\frac{1}{4\pi} \int_{\Omega \setminus V_\varepsilon} \mathbf{D}(\mathbf{x}, \mathbf{x}_e) \cdot \nabla\Phi(\mathbf{x}) d^3x - \frac{1}{4\pi} \int_{V_\varepsilon} \mathbf{D}(\mathbf{x}, \mathbf{x}_e) \cdot \nabla\Phi(\mathbf{x}) d^3x \\ &= -\frac{1}{4\pi} \int_{\Omega \setminus V_\varepsilon} \nabla \cdot [\Phi(\mathbf{x})\mathbf{D}(\mathbf{x}, \mathbf{x}_e)] d^3x + \underbrace{\frac{1}{4\pi} \int_{\Omega \setminus V_\varepsilon} \Phi(\mathbf{x}) \nabla \cdot \mathbf{D}(\mathbf{x}, \mathbf{x}_e) d^3x}_0 \\ &\quad + \overbrace{\frac{q}{4\pi} \int_{V'_\varepsilon} \frac{1}{x^2} \frac{\partial\Phi(\mathbf{x} + \mathbf{x}_e)}{\partial x} d^3x}^{\rightarrow 0 \text{ as } \varepsilon \rightarrow 0} \\ &= \frac{Q}{4\pi} \int_{-\partial V'_\varepsilon} \Phi(\mathbf{x} + \mathbf{x}_e) \nabla \frac{1}{x} \cdot d^2\mathbf{x} \\ &= Q\Phi(\mathbf{x}_e) \end{aligned} \quad (2.27)$$

Here it has both been assumed that $\Phi(\mathbf{x})$ have a continuous first derivative as well as $\Phi(\mathbf{x})\mathbf{D}(\mathbf{x}, \mathbf{x}_e) \simeq 0$ on the boundary $\mathbf{x} \in \partial\Omega$. In order to use the divergence theorem, the singularity at \mathbf{x}_e was isolated in a spherical volume V_ε with radius $\varepsilon \rightarrow 0$ centered at \mathbf{x}_e .

From this point and onwards, a system in a steady state is no longer considered and hence the time dependence is brought back. However, the solution to the time dependent version of the model clearly must agree with the time independent quantities in the limit of steady state.

Since each lattice point in the crystal is occupied by a ion, the dynamics of the system is characterized by two time scales. That is, the time it takes to displace the

bound electrons relative their nuclei (deformation of ion) and the time it takes to displace the nucleus relative the lattice (deformation of lattice structure). These two types of deformation are illustrated in figure 2.2. Since the electrons are significantly lighter than their nuclei, the ion deformation time is expected to be much smaller than the time it takes to deformation the lattice. Denoting these timescales as t_{uv} and t_{ir} respectively, this translates to $t_{uv} \ll t_{ir}$ or $\omega_{uv} \gg \omega_{ir}$, where $\omega \propto 1/t$ is the corresponding characteristic frequency. The subscripts of course indicate that frequencies lie in the ultraviolet and infrared region respectively. The total deformation, due to these two types of deformations, may then be expressed as $\mathbf{P} = \mathbf{P}_{ir} + \mathbf{P}_{uv}$.

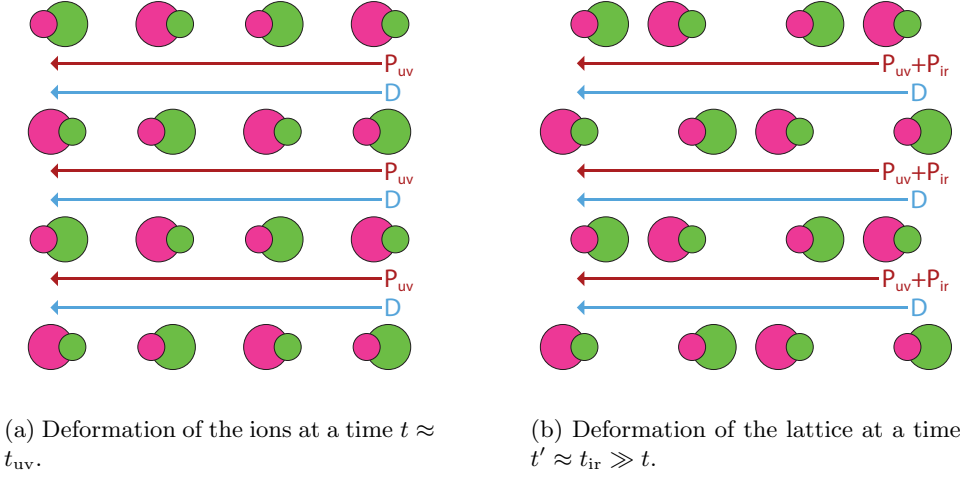


Figure 2.2

It is reasonable to further assume that each type of polarization behave as a driven harmonic oscillator, that is

$$\ddot{\mathbf{P}}_{ir}(\mathbf{x}) + \omega_{ir}^2 \mathbf{P}_{ir}(\mathbf{x}) = \frac{\mathbf{D}(\mathbf{x}, \mathbf{x}_e)}{\gamma}, \quad \ddot{\mathbf{P}}_{uv}(\mathbf{x}) + \omega_{uv}^2 \mathbf{P}_{uv}(\mathbf{x}) = \frac{\mathbf{D}(\mathbf{x}, \mathbf{x}_e)}{\delta}. \quad (2.28)$$

Here γ and δ are constants to be determined using the steady state solution

$$4\pi\mathbf{P}(\mathbf{x}) = (1 - 1/\epsilon)\mathbf{D}(\mathbf{x}, \mathbf{x}_e), \quad (2.29)$$

which follow from equation (2.23). However, since there are two unknowns to be solved for an additional relation is needed.

This second relation is the time-dependent high frequency response $\mathbf{D} = \epsilon_\infty \mathbf{E}$, where the rate of change ω_∞ of the external \mathbf{D} -field satisfies $\omega_{uv} \gg \omega_\infty \gg \omega_{ir}$. In the case of a free electron this criterion implies that the electron must be moving

extremely slowly compared to the UV timescale, but extremely quick compared to the IR timescale. Hence the UV-part of the polarization will manage to follow the changes in the \mathbf{D} -field nearly adiabatically whilst the IR-part won't have time to adapt to the changes. It is therefore reasonable to assume the latter contribution to be approximately constant as well as negligible in comparison to the former contribution, i.e. $\mathbf{P} \simeq \mathbf{P}_{\text{uv}}$. Using this last approximation together with the relation of \mathbf{D} and \mathbf{E} through ϵ_∞ , one obtains in similarity to (2.29)

$$4\pi\mathbf{P}_{\text{uv}}(\mathbf{x}) = (1 - 1/\epsilon_\infty)\mathbf{D}(\mathbf{x}, \mathbf{x}_e). \quad (2.30)$$

By subtracting (2.30) from (2.29) a similar expression for \mathbf{P}_{ir} is found to be

$$4\pi\mathbf{P}_{\text{ir}}(\mathbf{x}) = (1/\epsilon_\infty - 1/\epsilon)\mathbf{D}(\mathbf{x}, \mathbf{x}_e). \quad (2.31)$$

Further implications of the current rate of change ω_∞ are obtained by substituting $\ddot{\mathbf{P}}_{\text{uv}} \approx \omega_\infty^2 \mathbf{P}_{\text{uv}} \ll \omega_{\text{uv}}^2 \mathbf{P}_{\text{uv}}$ and $\dot{\mathbf{P}}_{\text{ir}} \approx 0$ into (2.28), which then simplifies to

$$\omega_{\text{ir}}^2 \mathbf{P}_{\text{ir}}(\mathbf{x}) = \frac{\mathbf{D}(\mathbf{x}, \mathbf{x}_e)}{\gamma}, \quad \omega_{\text{uv}}^2 \mathbf{P}_{\text{uv}}(\mathbf{x}) = \frac{\mathbf{D}(\mathbf{x}, \mathbf{x}_e)}{\delta}. \quad (2.32)$$

By finally comparing this equation to (2.30) and (2.31) the value of γ and δ , in terms of known material properties, are found to be

$$\frac{1}{\gamma} = \frac{\omega_{\text{ir}}^2}{4\pi} \left(\frac{1}{\epsilon_\infty} - \frac{1}{\epsilon} \right), \quad \frac{1}{\delta} = \frac{\omega_{\text{uv}}^2}{4\pi} \left(1 - \frac{1}{\epsilon_\infty} \right). \quad (2.33)$$

Having formulated the equation of motion for the two types of polarization, the next task is to construct one for the free electron. Since the electron was assumed to be slowly moving, one may without hesitation treat it in the non-relativistic limit. Then the only force acting on the electron is due to the bound electric field, i.e. $\mathbf{F}(\mathbf{x}_e) = q\mathbf{E}_{\text{bound}}(\mathbf{x}_e) = -q\nabla\Phi(\mathbf{x}_e)$. Thus $m\ddot{\mathbf{x}}_e = \dot{\mathbf{p}}_e = -q\nabla\Phi(\mathbf{x}_e)$ where m is an effective mass which in general is different from the electronic mass m_e . By treating \mathbf{p}_e , $\mathbf{P}_{\text{uv}}(\mathbf{x})$ and $\mathbf{P}_{\text{ir}}(\mathbf{x})$ as independent quantities, one may out of the equations of motion together with the interaction (2.27) construct the Lagrangian

$$L = \frac{\gamma}{2} \int \left[\dot{\mathbf{P}}_{\text{ir}}^2(\mathbf{x}) - \omega_{\text{ir}}^2 \mathbf{P}_{\text{ir}}^2(\mathbf{x}) \right] d^3x + \frac{\delta}{2} \int \left[\dot{\mathbf{P}}_{\text{uv}}^2(\mathbf{x}) - \omega_{\text{uv}}^2 \mathbf{P}_{\text{uv}}^2(\mathbf{x}) \right] d^3x \\ + \int \mathbf{D}(\mathbf{x}, \mathbf{x}_e) \cdot [\mathbf{P}_{\text{ir}}(\mathbf{x}) + \mathbf{P}_{\text{uv}}(\mathbf{x})] d^3x + \frac{\mathbf{p}_e^2}{2m}, \quad (2.34)$$

Performing a Legendre transformation, the Hamiltonian is found to be

$$H = \frac{\gamma}{2} \int \left[\dot{\mathbf{P}}_{\text{ir}}^2(\mathbf{x}) + \omega_{\text{ir}}^2 \mathbf{P}_{\text{ir}}^2(\mathbf{x}) \right] d^3x + \frac{\delta}{2} \int \left[\dot{\mathbf{P}}_{\text{uv}}^2(\mathbf{x}) + \omega_{\text{uv}}^2 \mathbf{P}_{\text{uv}}^2(\mathbf{x}) \right] d^3x \\ - \int \mathbf{D}(\mathbf{x}, \mathbf{x}_e) \cdot [\mathbf{P}_{\text{ir}}(\mathbf{x}) + \mathbf{P}_{\text{uv}}(\mathbf{x})] d^3x + \frac{\mathbf{p}_e^2}{2m}. \quad (2.35)$$

Since the UV-part of the polarization follows the external field nearly adiabatically, the dynamic solution \mathbf{P}_{uv} is approximately the static one with respect to

instantaneous value of \mathbf{D} -field. Hence the contribution of \mathbf{P}_{uv} to the the Hamiltonian becomes constant so that it can be removed without affecting the dynamics, giving rise merely to an energy shift. Having removed \mathbf{P}_{uv} from the theory it is no longer necessary to keep the subscript of \mathbf{P}_{ir} and ω_{ir} for differentiation purposes, therefore it is from here on omitted.

Before proceeding with the derivation, it is important to point out that the integrals in L and H are divergent. The reason for this is the polarization, which according to (2.30) and (2.31) is proportional to the \mathbf{D} -field which in turn is singular at $\mathbf{x} = \mathbf{x}_e$. This divergence is a consequence from disregarding the lattice structure when interpreting the displacements as a continuous vector field. If one were to calculate this integral, it would be necessary to express the polarization as a Fourier series and omit terms with a wave length smaller than that of the lattice constant.

At this point it is convenient to introduce here a complex vector field \mathbf{B} ,

$$\mathbf{B}(\mathbf{x}) = \sqrt{\frac{\gamma\omega}{2}} \left[\mathbf{P}(\mathbf{x}) + \frac{i}{\omega} \dot{\mathbf{P}}(\mathbf{x}) \right], \quad \mathbf{B}^*(\mathbf{x}) = \sqrt{\frac{\gamma\omega}{2}} \left[\mathbf{P}(\mathbf{x}) - \frac{i}{\omega} \dot{\mathbf{P}}(\mathbf{x}) \right], \quad (2.36)$$

so that

$$\mathbf{P}(\mathbf{x}) = \sqrt{\frac{1}{2\omega\gamma}} [\mathbf{B}^*(\mathbf{x}) + \mathbf{B}(\mathbf{x})], \quad \dot{\mathbf{P}}(\mathbf{x}) = i\sqrt{\frac{\omega}{2\gamma}} [\mathbf{B}^*(\mathbf{x}) - \mathbf{B}(\mathbf{x})]. \quad (2.37)$$

The reasons to why this field was introduced will become evident when quantizing the theory. The Hamiltonian, re-expressed in terms of the \mathbf{B} -field, transform into

$$H = \frac{\mathbf{p}_e^2}{2m} + \omega \int \mathbf{B}^*(\mathbf{x}) \cdot \mathbf{B}(\mathbf{x}) d^3x - \sqrt{\frac{1}{2\gamma\omega}} \int \mathbf{D}(\mathbf{x}, \mathbf{x}_e) \cdot [\mathbf{B}(\mathbf{x}) + \mathbf{B}^*(\mathbf{x})] d^3x. \quad (2.38)$$

By assuming the system to be cubic of size $V = l^3$, the \mathbf{B} -field and its complex conjugate may each be expressed in terms of a Fourier series

$$\mathbf{B}(\mathbf{x}) = \sum_{\mathbf{q}} \frac{\mathbf{q}}{q} b_{\mathbf{q}} \frac{e^{i\mathbf{q} \cdot \mathbf{x}}}{\sqrt{V}}, \quad \mathbf{B}^*(\mathbf{x}) = \sum_{\mathbf{q}} \frac{\mathbf{q}}{q} b_{\mathbf{q}}^* \frac{e^{-i\mathbf{q} \cdot \mathbf{x}}}{\sqrt{V}} \quad (2.39)$$

where the wave vectors are given according to (2.11). Next, by defining a scalar potential Ξ for the IR-part of the polarization as $4\pi\mathbf{P} = \nabla\Xi$ it is according to (2.27) possible to express the interaction energy between \mathbf{D} and \mathbf{P} as $Q\Xi(\mathbf{x}_e)$. Using (2.36) and (2.39) together with Ξ the expression for the Hamiltonian then becomes

$$H = \frac{\mathbf{p}_e^2}{2m} + \omega \sum_{\mathbf{q}} b_{\mathbf{q}}^* b_{\mathbf{q}} + \frac{1}{\sqrt{V}} \sum_{\mathbf{q}} V(q) [b_{\mathbf{q}}^* e^{-i\mathbf{q} \cdot \mathbf{x}_e} - b_{\mathbf{q}} e^{i\mathbf{q} \cdot \mathbf{x}_e}], \quad (2.40)$$

where both

$$V(q) = i \left(2\sqrt{2}\pi\alpha \right)^{1/2} \left(\frac{\omega^3}{m} \right)^{1/4} \frac{1}{q} \quad (2.41)$$

and the interaction parameter

$$\alpha = \frac{1}{2} \left(\frac{1}{\epsilon_\infty} - \frac{1}{\epsilon} \right) \sqrt{\frac{2m}{\omega}} Q^2 \quad (2.42)$$

has been introduced.

Here it seems as if the interaction part of the Hamiltonian is ill behaved since the $\mathbf{q} = \mathbf{0}$ term clearly is singular. This is a consequence from the periodic boundary condition which was imposed when expressing \mathbf{B} as a Fourier series. Originally the system contained only a single free electron. With a periodic boundary condition however, the system now consists of an infinite number of copies of the cube with volume V , each containing a free electron. These electrons interact with one another due to the long range Coulomb repulsion. To avoid this behavior when periodically continuing the system, one should introduce in each cube the uniform charge density $-Q/V$. Doing so would give rise to an attractive Coulomb force which for each electron would cancel the Coulomb repulsion. Such an interaction would exactly cancel the ill behaved $\mathbf{q} = \mathbf{0}$ term in the interaction part of the Hamiltonian, since the only difference would be the sign of the charge, i.e $Q \rightarrow -Q$.

2.3.2 Quantization

In order to quantize the theory, it is of utter importance to construct a set of canonical coordinates p_i and q_i for which the commutation relations are. Using (2.28) and (2.35), it is easy to verify that $\phi_i(\mathbf{x}, t)_i = [\mathbf{P}(\mathbf{x}, t)]_i$ and $\pi_i(\mathbf{x}, t) = \gamma[\dot{\mathbf{P}}(\mathbf{x}, t)]_i$ obey Hamilton's field equations

$$\dot{\phi}_i = \frac{\delta H}{\delta \pi_i}, \quad \dot{\pi}_i = -\frac{\delta H}{\delta \phi_i} \quad (2.43)$$

and thus constitutes a set of canonical field coordinates. By then employing a restricted canonical transformation $q_i = q_i(\phi, \pi)$, $p_i = p_i(\phi, \pi)$, one obtains the following set of canonical coordinates

$$q_{\mathbf{k}} = \sqrt{\frac{1}{2\omega\gamma}} [b_{\mathbf{k}}^* + b_{\mathbf{k}}], \quad p_{\mathbf{k}} = i\sqrt{\frac{\gamma\omega}{2}} [b_{\mathbf{k}}^* - b_{\mathbf{k}}]. \quad (2.44)$$

It is pretty straight forward to verify that this is in fact true. Using (2.37) and (2.39) together with the expressions for the sets of canonical coordinates one may

express ϕ, π in terms of $q_{\mathbf{k}}, p_{\mathbf{k}}$ and vice versa,

$$\begin{aligned}
 q_{\mathbf{k}} &= \frac{1}{\sqrt{V}} \int \frac{\mathbf{k}}{k} \cdot \left[\frac{1}{\omega\gamma} \pi(\mathbf{x}) \sin \mathbf{k} \cdot \mathbf{x} + \phi(\mathbf{x}) \cos \mathbf{k} \cdot \mathbf{x} \right] d^3x \\
 p_{\mathbf{k}} &= \frac{1}{\sqrt{V}} \int \frac{\mathbf{k}}{k} \cdot [\pi(\mathbf{x}) \cos \mathbf{k} \cdot \mathbf{x} - \omega\gamma \phi(\mathbf{x}) \sin \mathbf{k} \cdot \mathbf{x}] d^3x \\
 \phi(\mathbf{x}) &= \frac{1}{\sqrt{V}} \sum_{\mathbf{k}} \frac{\mathbf{k}}{k} \left[q_{\mathbf{k}} \cos \mathbf{k} \cdot \mathbf{x} - \frac{1}{\omega\gamma} p_{\mathbf{k}} \sin \mathbf{k} \cdot \mathbf{x} \right] \\
 \pi(\mathbf{x}) &= \frac{1}{\sqrt{V}} \sum_{\mathbf{k}} \frac{\mathbf{k}}{k} [\omega\gamma q_{\mathbf{k}} \sin \mathbf{k} \cdot \mathbf{x} + p_{\mathbf{k}} \cos \mathbf{k} \cdot \mathbf{x}] .
 \end{aligned} \tag{2.45}$$

Then, by showing that these coordinates satisfy the relations [14]

$$\begin{aligned}
 \left(\frac{\delta q_{\mathbf{k}}}{\delta \phi_i} \right)_{\phi, \pi} &= \left(\frac{\partial \pi_i}{\partial p_{\mathbf{k}}} \right)_{q, p} & \left(\frac{\delta q_{\mathbf{k}}}{\delta \pi_i} \right)_{\phi, \pi} &= - \left(\frac{\partial \phi_i}{\partial p_{\mathbf{k}}} \right)_{q, p} \\
 \left(\frac{\delta p_{\mathbf{k}}}{\delta \pi_i} \right)_{\phi, \pi} &= \left(\frac{\partial \phi_i}{\partial q_{\mathbf{k}}} \right)_{q, p} & \left(\frac{\delta p_{\mathbf{k}}}{\delta \phi_i} \right)_{\phi, \pi} &= - \left(\frac{\partial \pi_i}{\partial q_{\mathbf{k}}} \right)_{q, p}
 \end{aligned} \tag{2.46}$$

proves that the transformation used, and the set of coordinates $q_{\mathbf{k}}, p_{\mathbf{k}}$ obtained, both are canonical.

Before promoting these new coordinates to operators, one must symmetrize the product $b_{\mathbf{q}}^* b_{\mathbf{q}}$. Up to this point, $b_{\mathbf{q}}^*$ and $b_{\mathbf{q}}$ have been complex valued variables so that the order in which they appeared in such a product does not matter. However, due to a nonzero commutation relation when promoted to operators, this will no longer be the case. In order to not favor any of the two possible orderings, they are chosen to contribute equally, i.e. $b_{\mathbf{q}}^* b_{\mathbf{q}} = (b_{\mathbf{q}}^* b_{\mathbf{q}} + b_{\mathbf{q}} b_{\mathbf{q}}^*)/2$.

By promoting the canonical coordinates to operators and imposing Bose statistics onto $\hat{q}_{\mathbf{q}}, \hat{p}_{\mathbf{q}}$, the commutation relations follow from the corresponding poisson bracket relations of classical mechanics, i.e.

$$\begin{aligned}
 \{q_{\mathbf{k}}, p_{\mathbf{p}}\}_{\text{PB}} &= \delta_{\mathbf{k}, \mathbf{p}} \rightarrow [\hat{q}_{\mathbf{k}}, \hat{p}_{\mathbf{p}}] = i\delta_{\mathbf{k}, \mathbf{p}} \\
 \{\mathbf{x}_e[i], \mathbf{p}_e[j]\}_{\text{PB}} &= \delta_{i,j} \rightarrow [\hat{\mathbf{x}}_e[i], \hat{\mathbf{p}}_e[j]] = i\delta_{i,j} .
 \end{aligned} \tag{2.47}$$

Substituting with (2.44) into the first of these equations, and using that $[\hat{q}_{\mathbf{k}}, \hat{q}_{\mathbf{p}}] = [\hat{p}_{\mathbf{k}}, \hat{p}_{\mathbf{p}}] = 0$, one is left with the relations $[\hat{b}_{\mathbf{k}}, \hat{b}_{\mathbf{p}}^\dagger] = \delta_{\mathbf{k}, \mathbf{p}}$ and $[\hat{b}_{\mathbf{k}}, \hat{b}_{\mathbf{p}}] = 0$. Using these commutation relations the previously symmetrized terms of the Hamiltonian are rewritten as $(\hat{b}_{\mathbf{q}}^\dagger \hat{b}_{\mathbf{q}} + \hat{b}_{\mathbf{q}} \hat{b}_{\mathbf{q}}^\dagger)/2 = \hat{b}_{\mathbf{q}}^\dagger \hat{b}_{\mathbf{q}} + \frac{1}{2}$. The full Hamiltonian in quantized form then becomes

$$\hat{H} = \frac{\hat{\mathbf{p}}_e^2}{2m} + \omega \sum_{\mathbf{q}} \hat{b}_{\mathbf{q}}^\dagger \hat{b}_{\mathbf{q}} + \frac{1}{\sqrt{V}} \sum_{\mathbf{q}} V(q) \left(\hat{b}_{\mathbf{q}}^\dagger e^{-i\mathbf{q} \cdot \hat{\mathbf{x}}_e} - \hat{b}_{\mathbf{q}} e^{i\mathbf{q} \cdot \hat{\mathbf{x}}_e} \right) . \tag{2.48}$$

where the zero point energy $\omega \sum_{\mathbf{q}} \frac{1}{2}$ of the oscillating ions have been omitted.

The commutation relations satisfied by $\hat{b}_{\mathbf{q}}^\dagger$ and $\hat{b}_{\mathbf{q}}$ are the same as (2.2), implying that these operators are nothing but the creation and annihilation operators of a bosonic field. The polarization field \mathbf{P} can then be thought of as being represented by a set of harmonic oscillators each corresponding to a quantized mode of vibration in the lattice, i.e. a phonon. Since the frequency of the phonons is momentum independent they it is said to be dispersionless. For optical phonons which couple to infrared radiation, this is at low momenta a good approximation as shown in the figure 2.3.

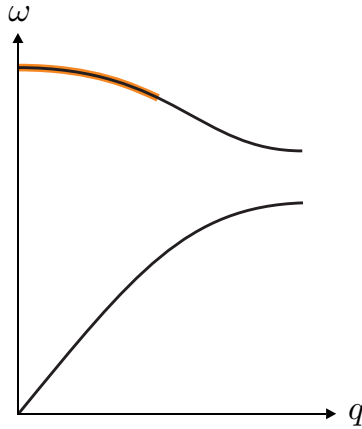


Figure 2.3: The upper and lower curves illustrate the characteristics of an optical and acoustic dispersion relation respectively. The outlined orange region suggests where the optical dispersion relation may be well approximated as momentum independent.

Having sorted out the quantization of the \mathbf{B} -field, the attention is turned towards the electron which has not yet undergone second-quantization. In order to achieve this, the recipe (2.4) is used which translates a one-body operator from first to second-quantization. By using the allowed momenta (2.11) as occupation

numbers for the electron state, one obtains

$$\begin{aligned}
\frac{\hat{\mathbf{p}}_e^2}{2m} &\rightarrow \sum_{\mathbf{p}} \frac{p^2}{2m} \hat{a}_{\mathbf{p}}^\dagger \hat{a}_{\mathbf{p}}, \\
e^{-i\mathbf{q} \cdot \hat{\mathbf{x}}_e} &\rightarrow \sum_{\mathbf{k}, \mathbf{p}} \langle \mathbf{k} | e^{-i\mathbf{q} \cdot \hat{\mathbf{x}}_e} | \mathbf{p} \rangle \hat{a}_{\mathbf{k}}^\dagger \hat{a}_{\mathbf{p}} \\
&= \sum_{\mathbf{k}, \mathbf{p}} \langle \mathbf{k} | \left[\int |\mathbf{x}\rangle \langle \mathbf{x}| d^3x \right] e^{-i\mathbf{q} \cdot \hat{\mathbf{x}}_e} \left[\int |\mathbf{y}\rangle \langle \mathbf{y}| d^3y \right] | \mathbf{p} \rangle \hat{a}_{\mathbf{k}}^\dagger \hat{a}_{\mathbf{p}} \\
&= \sum_{\mathbf{k}, \mathbf{p}} \hat{a}_{\mathbf{k}}^\dagger \hat{a}_{\mathbf{p}} \int d^3x \frac{e^{-i\mathbf{k} \cdot \mathbf{x}}}{\sqrt{V}} e^{-i\mathbf{q} \cdot \mathbf{x}} \frac{e^{i\mathbf{p} \cdot \mathbf{x}}}{\sqrt{V}} \\
&= \sum_{\mathbf{k}, \mathbf{p}} \hat{a}_{\mathbf{k}}^\dagger \hat{a}_{\mathbf{p}} \delta(\mathbf{k} + \mathbf{q} - \mathbf{p}) \\
&= \sum_{\mathbf{p}} \hat{a}_{\mathbf{p}-\mathbf{q}}^\dagger \hat{a}_{\mathbf{p}}
\end{aligned} \tag{2.49}$$

and similarly

$$e^{i\mathbf{q} \cdot \hat{\mathbf{x}}_e} \rightarrow \sum_{\mathbf{p}} \hat{a}_{\mathbf{p}+\mathbf{q}}^\dagger \hat{a}_{\mathbf{p}}. \tag{2.50}$$

Substituting with this into the Hamiltonian and using that interaction term is symmetric with respect to \mathbf{q} , the fully second-quantized Hamiltonian becomes

$$\hat{H} = \sum_{\mathbf{p}} \frac{p^2}{2m} \hat{a}_{\mathbf{p}}^\dagger \hat{a}_{\mathbf{p}} + \omega \sum_{\mathbf{q}} \hat{b}_{\mathbf{q}}^\dagger \hat{b}_{\mathbf{q}} + \frac{1}{\sqrt{V}} \sum_{\mathbf{q}, \mathbf{p}} V(q) \left(\hat{b}_{\mathbf{q}}^\dagger - \hat{b}_{-\mathbf{q}} \right) \hat{a}_{\mathbf{p}-\mathbf{q}}^\dagger \hat{a}_{\mathbf{p}}. \tag{2.51}$$

The grand canonical Hamiltonian \hat{K} , which is used extensively in the finite temperature field theory, is obtained by adding chemical potentials to \hat{H} . But, since there is no conservation law regarding the number of phonons it must be the case that $\mu_{\text{phonon}} = 0$. Thus

$$\hat{K} = \sum_{\mathbf{p}} \left(\frac{p^2}{2} - \mu \right) \hat{a}_{\mathbf{p}}^\dagger \hat{a}_{\mathbf{p}} + \sum_{\mathbf{q}} \hat{b}_{\mathbf{q}}^\dagger \hat{b}_{\mathbf{q}} + \frac{1}{\sqrt{V}} \sum_{\mathbf{q}, \mathbf{p}} V(q) \left(\hat{b}_{\mathbf{q}}^\dagger - \hat{b}_{-\mathbf{q}} \right) \hat{a}_{\mathbf{p}-\mathbf{q}}^\dagger \hat{a}_{\mathbf{p}} \tag{2.52}$$

where for convenience $m = \omega = 1$ has been used.

2.4 Perturbation theory

Assume the Hamiltonian to be time-independent in the Schrödinger picture and expressible as the sum $\hat{K} = \hat{K}_0 + \hat{K}_1$, where \hat{K}_1 contains the interactions of the theory without which the problem would be exactly solvable. If this interaction is

weak enough, it is reasonable to treat it perturbatively by expanding with respect to some small interaction parameter α . In order to do so it is necessary to introduce yet a new picture, the interaction picture. In the finite temperature formalism, operators in the interaction picture are related to the ones in the Schrödinger picture through $\hat{O}_I(\tau) = e^{\hat{K}_0\tau} \hat{O}_S e^{-\hat{K}_0\tau}$. Within this picture, it is possible to express the ensemble average of a τ -ordered product of operators by the perturbation series

$$\begin{aligned} & \text{Tr}\{\hat{\rho}_G T_\tau[\hat{A}_K(\tau_a) \hat{B}_K(\tau_b) \cdots \hat{F}_K(\tau_f)]\} \\ &= \\ & \frac{\sum_{n=0}^{\infty} \frac{(-1)^n}{n!} \int_0^\beta d\tau_1 \cdots \int_0^\beta d\tau_n \text{Tr}\left\{e^{-\beta\hat{K}_0} T_\tau[\hat{K}_1(\tau_1) \cdots \hat{K}_1(\tau_n) \hat{A}(\tau_a) \hat{B}(\tau_b) \cdots \hat{F}(\tau_f)]\right\}}{\sum_{n=0}^{\infty} \frac{(-1)^n}{n!} \int_0^\beta d\tau_1 \cdots \int_0^\beta d\tau_n \text{Tr}\left\{e^{-\beta\hat{K}_0} T_\tau[\hat{K}_1(\tau_1) \cdots \hat{K}_1(\tau_n)]\right\}}. \end{aligned} \quad (2.53)$$

In both the nominator and denominator of the expression above, there is the frequently appearing factor

$$\text{Tr}\{e^{-\beta\hat{K}_0} T_\tau[\hat{A} \hat{B} \cdots \hat{F}]\}. \quad (2.54)$$

It was first proved by Matsubara [13] that this factor could be rewritten as the sum of all possible permutations of contractions $\hat{A} \hat{B} \cdots \hat{F} \equiv \text{Tr}\{\hat{\rho}_{G0} T_\tau[\hat{A} \hat{B}]\}$ amongst the product of operators $\hat{A} \hat{B} \cdots \hat{F}$. Here $\hat{\rho}_{G0}$ is the bare statistical operator, defined in accordance with $\hat{\rho}_G$ but having the full Hamiltonian replaced by the noninteracting part only. In the case of a creation and an annihilation operator, the contraction,

$$\hat{c}_{\mathbf{k}}(\tau) \hat{c}_{\mathbf{k}}^\dagger(\tau') = \text{Tr}\{\hat{\rho}_{G0} T_\tau[\hat{c}_{\mathbf{k}}(\tau) \hat{c}_{\mathbf{k}}^\dagger(\tau')]\} = \mathcal{G}^{(0)}(\mathbf{k}, \tau), \quad (2.55)$$

is nothing but the definition of the bare propagator in momentum space (2.14). All other types of contractions amongst such operators turn out to be zero, i.e.

$$\hat{c}_{\mathbf{k}}(\tau) \hat{c}_{\mathbf{k}}(\tau') = \hat{c}_{\mathbf{k}}^\dagger(\tau) \hat{c}_{\mathbf{k}}^\dagger(\tau') = \hat{c}_{\mathbf{k}}(\tau) \hat{c}_{\mathbf{p}}^\dagger(\tau') = 0 \quad \forall \quad \mathbf{k} \neq \mathbf{p}. \quad (2.56)$$

Hence only a small part of all terms in (2.54) survive, and these are the ones which may be represented pictorially in terms of Feynman diagrams. Further the denominator of (2.53) will serve to precisely cancel out any unconnected diagram part from the nominator. What is left of the perturbations series is then an infinite number of connected Feynman diagrams which are easily constructed from a set of Feynman rules.

2.4.1 Diagrammatic analysis

The constituents of the resulting Feynman diagrams are easily obtained just by analyzing the Hamiltonian (2.52). Using the vacuum ground state ensemble, the

bare electronic and phononic propagators, referred to as $\mathcal{G}^{(0)}$ and $\mathcal{D}^{(0)}$ respectively, are given according to (2.22) and represented as

$$0 \xrightarrow{\mathbf{p}} \tau = \mathcal{G}^{(0)}(\mathbf{p}, \tau) = \exp \left\{ - \left(\frac{p^2}{2} - \mu \right) \tau \right\} \quad \tau \geq 0, \quad (2.57)$$

$$0 \text{ --- } \mathbf{q} \text{ --- } \tau = \mathcal{D}^{(0)}(\mathbf{q}, \tau) = \exp \{ -\tau \} \quad \tau \geq 0. \quad (2.58)$$

Since any propagator going backwards in time is identically zero, it is possible to use the convention that the momentum is carried in the direction of increased time, which throughout this paper will be towards the right. Then, by examining the interaction part of the Hamiltonian, the possible vertices and their contribution are found out to be

$$\begin{array}{c}
 \text{Diagram: } \xrightarrow{\mathbf{p}} \bullet \xrightarrow{\mathbf{p}-\mathbf{q}} \quad \text{--- } \mathbf{q} \text{ ---} \quad \xrightarrow{\mathbf{p}-\mathbf{q}} \bullet \xrightarrow{\mathbf{p}} \\
 \text{Equation: } = \frac{V(\mathbf{q})}{\sqrt{V}}
 \end{array} \quad (2.59)$$

with $V(\mathbf{q})$ as defined in (2.41).

In this thesis only the electronic single-particle Green's function will be studied in terms of Feynman diagrams. Hence the operators $\hat{A} \hat{B} \cdots \hat{F}$ in the perturbation series (2.53) are replaced by $\hat{a}_{\mathbf{p}} \hat{a}_{\mathbf{p}}^{\dagger}$ as to coincide with the definition (2.14) of $\mathcal{G}(\mathbf{p}, \tau)$. In order to construct the relevant diagrams, the Feynman rules [11] dictate:

1. Draw all topologically distinct diagrams with $2n + 1$ electron lines and n phonon lines.
2. With each particle line associate a factor $\mathcal{G}^{(0)}$ in case of an electron, and $\mathcal{D}^{(0)}$ in case of a phonon.
3. Each vertex contributes with the factor $V(\mathbf{q})/\sqrt{V}$, where \mathbf{q} is the momentum of the phonon connected to this vertex.
4. Conserve the total momentum at every vertex.

5. The external legs should both be assigned the external momentum \mathbf{p} of the interacting Green's function $\mathcal{G}(\mathbf{p}, \tau)$. The ingoing external leg should start at the imaginary time 0 and the outgoing external leg should terminate at τ .
6. For each of the n internal momenta, sum over all allowed momentum values.
7. For each of the n internal imaginary times, integrate from 0 to β .
8. Multiply each diagram with the factor $(-1)^n$.

In this thesis the single-particle Green's function will be studied in the limit $V \rightarrow \infty$. Hence the sums over internal momenta should be replaced according to

$$\frac{1}{V} \sum_{\mathbf{k}} \cdots \rightarrow \int \frac{d^3 k}{(2\pi)^3} \cdots \quad (2.60)$$

Further more this will be studied at $T = 0$ implying that the upper limit of the imaginary time integrals becomes infinite.

Since the ground state ensemble is equal to that of vacuum, the propagators become identically zero for negative imaginary times. Because of this, the contribution from diagrams containing tadpoles, electron loops or similar structures vanish. This is illustrated in figure 2.4.

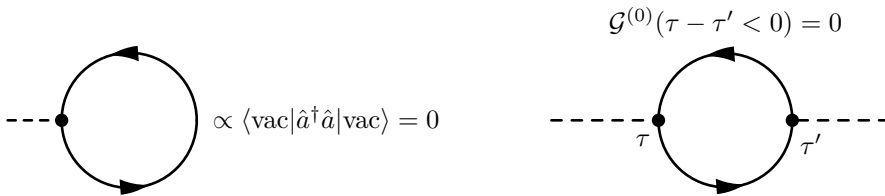


Figure 2.4: A tadpole and an electron loop both of which are equal to zero due to the ground state ensemble of vacuum.

Then the only contributing diagrams are those where all electron propagators follow after one another in a line, and phonon propagators spawn and die on the

vertices on that line. That is,

$$\begin{aligned}
 \mathcal{G}(\mathbf{p}, \tau) = & 0 \longrightarrow \mathbf{p} \longrightarrow \tau + 0 \longrightarrow \mathbf{p} \longrightarrow \tau_1 \xrightarrow{\mathbf{p}-\mathbf{q}} \tau_2 \xrightarrow{\mathbf{p}} \tau \\
 & + 0 \longrightarrow \mathbf{p} \longrightarrow \tau_1 \xrightarrow{\mathbf{p}-\mathbf{q}} \tau_2 \xrightarrow{\mathbf{p}} \tau_3 \xrightarrow{\mathbf{p}-\mathbf{k}} \tau_4 \xrightarrow{\mathbf{p}} \tau \\
 & + 0 \longrightarrow \mathbf{p} \longrightarrow \tau_1 \xrightarrow{\mathbf{p}-\mathbf{q}} \tau_2 \xrightarrow{\mathbf{p}-\mathbf{q}-\mathbf{k}} \tau_3 \xrightarrow{\mathbf{p}-\mathbf{k}} \tau_4 \xrightarrow{\mathbf{p}} \tau \\
 & + 0 \longrightarrow \mathbf{p} \longrightarrow \tau_1 \xrightarrow{\mathbf{p}-\mathbf{q}} \tau_2 \xrightarrow{\mathbf{p}-\mathbf{q}-\mathbf{k}} \tau_3 \xrightarrow{\mathbf{p}-\mathbf{q}} \tau_4 \xrightarrow{\mathbf{p}} \tau \\
 & + \dots
 \end{aligned}$$

It is obvious that the contribution from each diagram is nonzero only when the times are ordered chronologically, i.e. $0 = \tau_0 \leq \tau_1 \leq \tau_2 \leq \dots \leq \tau_{2n-1} = \tau$. Because if this was not the case at least one propagator would propagate backwards in time and contribute with a factor of zero. Thus it is only meaningful to carry out the integrals such that this chronologization constraint is fulfilled.

Another important property of these diagrams is that they all carry a positive definite contribution to \mathcal{G} . This since the value of a propagator always is larger than or equal to zero, and the sign from the factor $(-1)^n$ cancel the i^{2n} contained within $V(\mathbf{q})^{2n}$.

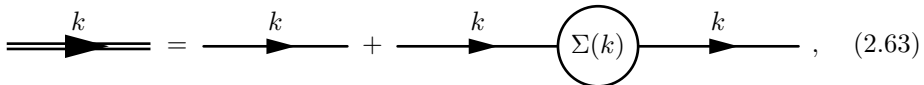
Since the Hamiltonian is isotropic, there will be no preferred direction of momenta. Hence the single particle Green's function will only be dependent on the magnitude of the external momentum $p = |\mathbf{p}|$, i.e. $\mathcal{G} = \mathcal{G} = \mathcal{G}(\alpha, \mu, p, \tau)$.

2.4.2 Dyson equation

Working at zero temperature allows for a full Fourier representation of the single-particle Green's function, i.e.

$$G(\mathbf{x}, \tau) = \frac{1}{(2\pi)^4} \int d^3k \int d\omega e^{i(\mathbf{k} \cdot \mathbf{x} - \omega\tau)} G(\mathbf{k}, \omega); \quad G = \mathcal{G}, \mathcal{D}, \mathcal{G}^{(0)}, \mathcal{D}^{(0)}. \quad (2.62)$$

It so happens to be more pleasant working in \mathbf{k} - ω space for a lot of reasons but what will be of importance here is the conservation of total four momentum $k = (\omega, \mathbf{k})$ at all vertices in a Feynman diagram. In that way the external legs of a diagram no longer depend upon any internal variables and may then be factored out from the nasty integral expression. Hence it is convenient to express the interacting single-particle Green's function, here depicted as a double line, in terms of the self-energy $\Sigma(k)$ as



$$\text{Double line } k = \text{Single line } k + \text{Single line } k \circlearrowleft \Sigma(k) \text{ Single line } k, \quad (2.63)$$

where

$$\begin{aligned}
 \Sigma(k) = & \text{---} \bullet \xrightarrow{k-q} \bullet \text{---} + \text{---} \bullet \xrightarrow{k-q} \bullet \text{---} \xrightarrow{k} \bullet \text{---} + \text{---} \bullet \xrightarrow{k-s} \bullet \text{---} \xrightarrow{k} \bullet \text{---} \\
 & + \text{---} \bullet \xrightarrow{k-q} \bullet \xrightarrow{k-q-s} \bullet \xrightarrow{k-s} \bullet \text{---} \\
 & + \text{---} \bullet \xrightarrow{k-q} \bullet \xrightarrow{k-q-s} \bullet \xrightarrow{k-q} \bullet \text{---} + \dots
 \end{aligned}$$

(2.64)

A related quantity is the proper self-energy $\Sigma^*(k)$, which is made up by a subset of the self-energy diagrams. These diagrams are said to be irreducible, meaning that they cannot be split in two by cutting only one propagator. Examples of such diagrams are the first, third and fourth diagram in (2.64). The second diagram in the same expression can be split in half by cutting the electronic propagator with four-momenta k and is then said to be a reducible diagram. With this definition of the proper self-energy, the self-energy is nothing but

$$\Sigma(k) = \Sigma^*(k) + \begin{array}{c} \Sigma^*(k) \\ \uparrow k \end{array} + \begin{array}{c} \Sigma^*(k) \\ \uparrow k \end{array} \Sigma^*(k) + \begin{array}{c} \Sigma^*(k) \\ \uparrow k \end{array} \Sigma^*(k) \Sigma^*(k) + \dots \quad (2.65)$$

By inserting (2.65) into (2.63), factoring out $\mathcal{G}^{(0)}(k)\Sigma^*(k)$ from every diagram but the bare propagator and identifying what is left with $\mathcal{G}(k)$, one obtains a self consistent expression for $\mathcal{G}(k)$ known as Dyson's equation,

$$\text{double line } k = \text{single line } k + \text{double line } k \circ \Sigma^*(k) \text{ single line } k \quad (2.66)$$

Hence the equation for $\mathcal{G}(k)$ in terms of $\mathcal{G}^{(0)}(k)$ and $\Sigma^*(k)$ becomes

$$\mathcal{G}(k) = \frac{1}{1/\mathcal{G}^{(0)}(k) - \Sigma^*(k)}. \quad (2.67)$$

2.5 Monte Carlo Methods

The Monte Carlo method [15, 16] studies models of systems by stochastic computer simulations. Such a simulation rely on repeated sampling of (pseudo-)random numbers in order to obtain results for models which in principle might be either deterministic or stochastic. In physics-related problems this method is often used in order to sample a sequence of states of a physical system whose probability is given in accordance to a model Hamiltonian. Expectation values of interest may then be approximated by appropriately constructed sample means.

Usually the state space of the system at hand is too large to fully cover during a Monte Carlo simulation which will lead to statistical noise in calculated system properties. A lot of this noise may be suppressed by sampling states which represent the system well. This is known as importance sampling.

2.5.1 Markov processes, detailed balance and ergodicity

In order to sample states of the system a Markov process is used. Given an initial state x such a process will generate a new state x' on random, i.e. if the Markov process repeatedly was given the state x the new state x' would not be the same every time. The probability $P(x|x')$ of generating a state x' given x is referred to as a transition probability. In order to be a Markov process there are two criteria which the transition probabilities must fulfill; they are not allowed to change with time and they may only depend on the properties of the current states x and x' . During the course of a Monte Carlo simulation the Markov process is repeatedly fed the system state in order to generate a sequence of states. When the simulation have run for a long enough time, the frequency for which a particular state is generated will be given by a distribution corresponding to the design of the transition probabilities. When this has happened one say that the process has reached an equilibrium and the distribution has become stationary. However, in order for the succession of generated states to match the pursued probability distribution when equilibrium has been reached, it is necessary that the conditions of ergodicity and detailed balance are satisfied.

Starting with the condition of ergodicity, this is the requirement that the Markov process should be able to reach any state of the system starting from any other state in a finite simulation time. This is equal to saying that there must be at least one path of non-zero transition probabilities between any two states. This is illustrated in figure 2.5. If the process would not be ergodic, some states would never be sampled, no matter how long the simulation was running. The equilibrium distribution of the Markov process would then be such that some states would have a zero probability mass, which in general would not agree with the true distribution of the simulated physical system.

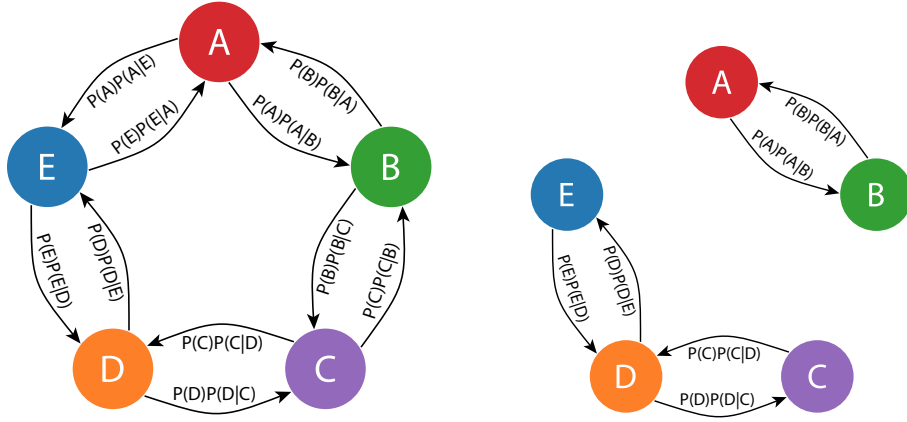


Figure 2.5: Illustrated is a state space consisting of the five possible states A, B, C, D and E, for which two Markov processes are constructed. For these processes all transitions which have a non-zero probability are depicted with an arrow. It is then clear that the Markov process to the left satisfy ergodicity whilst the one to the right does not.

Detailed balance is the requirement that the net flow of probability between any two states is exactly zero, i.e.

$$P(x) P(x|x') = P(x') P(x'|x) \quad (2.68)$$

where $P(x)$ is the probability of the system being in state x . Imposing such a condition on the transition probabilities it can be shown [16] that the Markov process must approach a simple equilibrium for which the stationary distribution is $\pi(x)$. Hence dynamics such a limit cycles are forbidden by this condition.

2.5.2 Metropolis-Hastings algorithm

The Metropolis-Hastings algorithm is a Markov chain Monte Carlo method for obtaining a sequence of random samples from a probability distribution for which direct sampling would be difficult. Briefly speaking, this algorithm is able to draw samples from any distribution $P(x)$ given that it is possible to compute the value of a function $f(x)$ which is proportional to the probability density function $\rho(x)$ of the distribution $P(x)$. The Metropolis-Hastings algorithm suggests constructing transition probabilities $P(x|x')$ in order to design a Markov process for which the stationary distribution $\pi(x)$ is chosen to be $P(x)$.

The starting point to derive the Metropolis-Hastings algorithm is to separate the transitional probabilities into two parts; the proposal $W(x|x')$ and acceptance-rejection $A(x|x')$. Here $W(x|x')$ is the conditional probability distribution of proposing state x' given state x and similarly $A(x|x')$ is the conditional probability distribution of accepting the proposed state x' given x . Expressing the transitional probability as a product of these two parts, i.e. $P(x|x') = W(x|x') A(x|x')$, the criteria of detailed balance (2.68) might be rewritten as

$$\frac{A(x|x')}{A(x'|x)} = \frac{P(x)}{P(x')} \frac{W(x'|x)}{W(x|x')} . \quad (2.69)$$

In order to fulfill the condition above, it is common to use the Metropolis choice for the acceptance,

$$A(x|x') = \min \left(1, \frac{P(x)}{P(x')} \frac{W(x'|x)}{W(x|x')} \right) = \min \left(1, \frac{f(x)}{f(x')} \frac{W(x'|x)}{W(x|x')} \right) , \quad (2.70)$$

where the proportionality between the density of P and f has been used in order to reach the last equality. The new state x' is then accepted according to $A(x|x')$. In practice this is achieved by sampling a uniform random number $a \in [0, 1]$ and accepting the proposed transition if $A(x|x') > a$, otherwise the transition is rejected. In case of the proposed state x' being rejected, the current state x is to be thought of as having been sampled yet again.

In order for the Markov process to cover as much of state space as possible, it is important to construct the proposal distributions in such a way that the acceptance ratios become as large as possible. If this is not the case the process will spend an unnecessary amount of time being rejected leaving the current state.

Chapter 3

Diagrammatic Monte Carlo

In this chapter the general idea behind the diagrammatic Monte Carlo method is first discussed and then illustrated with three examples. The bare scheme for directly simulating the single-particle Green's function \mathcal{G} of the polaron is then implemented, followed by the implementation of the bare scheme for simulating the proper self-energy Σ^* of \mathcal{G} . After that the latter scheme is boldified. Finally the ground state energy E_0 and the Z_0 -factor of the polaron are calculated and presented.

3.1 General idea

Diagrammatic Monte Carlo (from here on abbreviated DMC) is a numerical method developed by Prokof'ev et al. [5] which allows to simulate quantities $Q(\{y\})$ in terms of convergent diagrammatic series, i.e. sums of integrals with an ever increasing number of integration variables

$$Q(\{y\}) = \sum_{n=0}^{\infty} \sum_{\xi_n} \int dx_1 \dots dx_n D_n(\xi_n, \{y\}, x_1, \dots, x_n). \quad (3.1)$$

Here $\{y\}$ is a set of external variables and ξ_n (not to be confused with the energy eigenvalues ξ_ν of the grand canonical Hamiltonian \hat{K}) indexes the different integrands of order n which are given by the function D_n . Terms corresponding to $n = 0$ are understood as being known functions of the external variables. In case of a discrete internal variable x_i , the corresponding integral is exchanged in favor of a sum.

The method is based on the Metropolis-Hastings algorithm and samples integrands from the integral series in the $(\xi_n, \{y\}, x_1, \dots, x_n)$ parameter space. That is, a random walk is performed between the different integrands in the integral series, as well as between the possible values of the integration variables. In this

random walk it is also permissible to include one or more of the external variables. Since the terms at $n = 0$ are known functions it is then possible to calculate the value of Q by keeping track of the frequency by which these terms are sampled, as well as the length of the sequence of sampled terms.

To clarify any ambiguities, the main idea behind the DMC method will next be demonstrated by a few simple examples.

Example 1

In this example the task is to compute $1 + C$, where for convenience it is assumed that $C > 1$ is a constant. The integral series (3.1) will then contain merely two constant zeroth order terms, making the parameter space discrete with the two possibilities $\xi_0 = 0$ and $\xi_0 = 1$ corresponding to the terms 1 and C respectively.

To follow the recipe of the Metropolis-Hastings algorithm, the function D_n is regarded as proportional to the probability density function

$$\rho(x) = \frac{D_n(x)}{\sum_y D_n(y)} = \frac{D_n(x)}{1 + C} ; \quad x \in \{\xi_0 = 0, \xi_0 = 1\}, \quad (3.2)$$

allowing it to be substituted against f in (2.70) so that a sequence of ξ_0 's may be sampled from the corresponding probability distribution P . Since there are only the two states 1 and C in parameter space, there can be at most four types of transitions amongst them. By introducing the corresponding transition probabilities: $P(1|C)$, $P(C|1)$, $P(1|1)$ and $P(C|C)$, the Markov process to be simulated may then be illustrated as in figure (3.1).

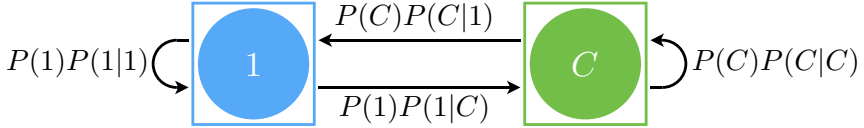


Figure 3.1: An illustration of the constructed Markov process for sampling the states $\xi_0 = 0$ and $\xi_1 = 1$ referred to as 1 and C respectively.

To simplify matters, the proposal distributions $W(1|C)$, $W(1|1)$, $W(C|1)$ and $W(C|C)$ are all chosen to have the same probability of $1/2$. Then, according to (2.70), the acceptance-rejection ratios will be given by $A(1|1) = A(1|C) = A(C|C) = 1$ and $A(C|1) = 1/C$. By keeping track of how many times $\xi_0 = 0$ appears in the generated sequence, lets say N_0 times, as well as the the total length N of the sequence, it is possible to calculate $1 + C$. This since

$$N_0 \propto \rho(1) \propto 1, \quad N - N_0 \propto \rho(C) \propto C \quad \Rightarrow \quad \frac{N_0}{N - N_0} = \frac{1}{C} \quad (3.3)$$

so that

$$1 + C = 1 + \frac{N - N_0}{N_0}. \quad (3.4)$$

Example 2

In this second example the task is to compute the sum $1 + \int_a^b x \, dx$. Instead of having two zeroth order terms as in the first example, there is now a zeroth and first order term. This implies that the parameter space is no longer completely discrete with merely two possible states. Similarly to the first example, the zeroth order term is still represented in parameter space by the state $\xi_0 = 0$. On the other hand, the first order term corresponds to the infinite number of states $(\xi_1 = 0, x \in [a, b])$. This notation of the states in parameter space is a little cumbersome, however, by assuming $b > a > 1$ it is possible to create a one-to-one mapping which maps $\xi_0 = 0$ and $(\xi_1 = 0, x \in [a, b])$ onto $x = 1$ and $x \in [a, b]$ respectively. Again the function D_n is regarded as proportional the probability density function

$$\rho(x) = \frac{D_n(x)}{\sum_y D_n(y)} = \frac{D_n(x)}{1 + \int_a^b x \, dx} ; \quad x \in \{1\} \cup [a, b]. \quad (3.5)$$

in order for the Markov process to generate states according to the probability distribution P corresponding to this choice of ρ . To cover the whole parameter space so that ergodicity is satisfied, it is more than sufficient to consider four types of transitions with corresponding transition probabilities $P(1|1)$, $P(1|x)$, $P(x|1)$ and $P(x|x')$. Here it is understood that $x, x' \in [a, b]$ and thus corresponds to a state of the first order term. This Markov process may be illustrated as figure 3.2.

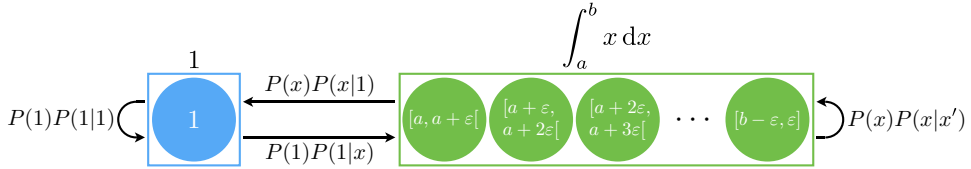


Figure 3.2: An illustration of the constructed Markov process for sampling the states 1 and x .

In order to construct proposal distributions to or from the first order term, it is convenient to introduce the collection of states referred to as f containing all states $x \in [a, b]$. Using this notation, the proposal distributions are chosen to be

$$\begin{aligned} W(1|1) &= \frac{1}{2} & W(1|x) &= W(1|f) U_{a,b}(x) = \frac{1}{2} \frac{1}{b-a} \\ W(x|1) &= W(f|1) = \frac{1}{2} & W(x|x') &= W(f|f) U_{a,b}(x') = \frac{1}{2} \frac{1}{b-a}. \end{aligned} \quad (3.6)$$

The quantities $W(1|1)$, $W(1|f)$, $W(f|1)$ and $W(f|f)$ are simply the probability of proposing a state corresponding to a certain term in the integral series and have been set equally probable. Also $U_{a,b}(x) = [b-a]^{-1}$ is the uniform probability

distribution on the interval $[a, b]$ from which x is sampled. Then, from the proposal distributions follow the acceptance rations

$$\begin{aligned} A(1|1) &= 1 & A(1|x) &= \min\left(1, [b-a]x\right) \\ A(x|1) &= \min\left(1, [b-a]^{-1}x^{-1}\right) & A(x|x') &= \min\left(1, x^{-1}x'\right). \end{aligned} \quad (3.7)$$

If then $x = 1$ appears N_0 number of times in the sequence of states with length N , it follows from (3.3) and (3.4) that

$$1 + \int_a^b x \, dx = 1 + \frac{N - N_0}{N_0}. \quad (3.8)$$

Example 3

In this third and final example, the task is to compute

$$1 + \int_a^b dx e^{-x} + \int_{a'}^{b'} dy \int_{a''}^{b''} dz e^{-y-z}, \quad (3.9)$$

which is more similar to the actual problem. This integral sum consists of a zeroth, first and second order term. By assuming that $b > a > 1$, a one-to-one mapping similar to the one used in the previous example may be preformed here as well. Again the zeroth and first order terms are chosen to be represented by $x = 1$ and $x \in [a, b]$ respectively, whilst the second order term is to be represented by $x = (y, z) \in [a', b'] \times [a'', b'']$.

Analogously to the former examples the function D_n is normalizable and may thus be thought of as a non-normalized probability density function. Hence a Markov process is used to generate a sequence of parameter space states from a probability distribution P corresponding to D_n . This time the Markov process is designed to have the seven types of transitions illustrated in figure 3.3.

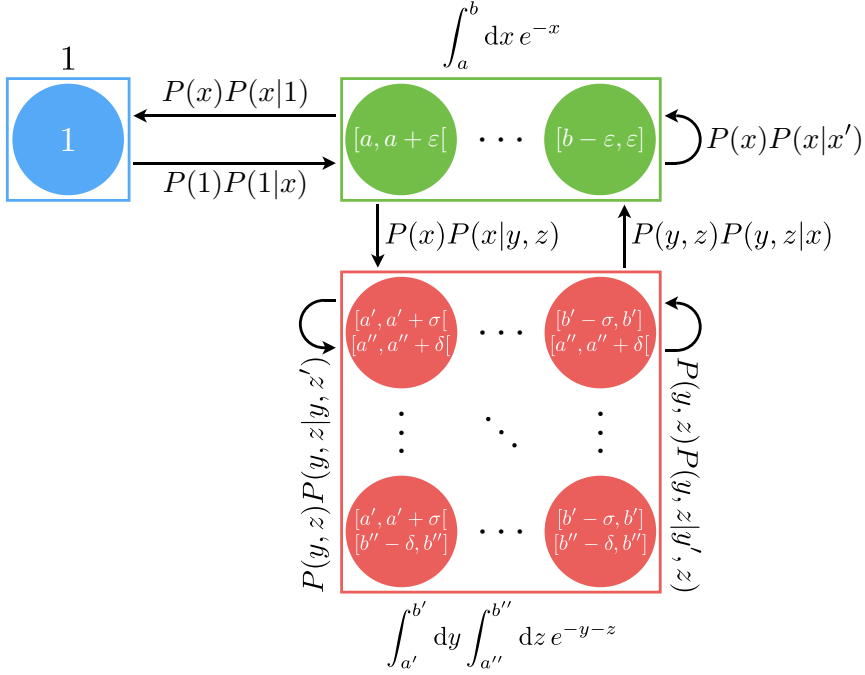


Figure 3.3: An illustration of the constructed Markov process for sampling the states 1, x and (y, z) .

In order to construct transition probabilities it is convenient to introduce the collection of states f and ff . These contain all states in parameter space corresponding the first and second order term respectively. The transition probabilities are then chosen as

$$\begin{aligned}
 W(1|x) &= W(1|f) U_{a,b}(x) & W(x|y, z) &= W(f|ff) U_{a',b'}(y) U_{a'',b''}(z) \\
 W(x|1) &= W(f|1) & W(y, z|y', z) &= W(ff|ff) W(ff|y') U_{a',b'}(y') \\
 W(y, z|x) &= W(ff|f) U_{a,b}(x) & W(y, z|y, z') &= W(ff|ff) W(ff|z') U_{a'',b''}(z') \\
 W(x|x') &= W(f|f) U_{a,b}(x'), & &
 \end{aligned} \tag{3.10}$$

where

$$\begin{aligned}
 W(1|f) &= 1 \\
 W(f|1) &= W(f|f) = W(f|ff) = \frac{1}{3} \\
 W(ff|f) &= W(ff|ff) = W(ff|y') = W(ff|z') = \frac{1}{2}.
 \end{aligned} \tag{3.11}$$

The discrete proposal distributions $W(ff|y')$ and $W(ff|z')$ correspond to choosing to update either the y or the z part of the total parameter state. Having all of this

information it is then trivial to calculate the acceptance ratios, which become

$$\begin{aligned}
W(1|x) &= \min\left(1, \frac{1}{3}[b-a]e^{-x}\right) \\
W(x|1) &= \min\left(1, 3[b-a]^{-1}e^x\right) \\
W(x|x') &= \min\left(1, e^{x-x'}\right) \\
W(x|y, z) &= \min\left(1, \frac{2}{3}[b'-a'] [b''-a''] [b-a]^{-1} e^{x-y-z}\right) \\
W(y, z|x) &= \min\left(1, \frac{3}{2}[b'-a']^{-1} [b''-a'']^{-1} [b-a] e^{y+z-x}\right) \\
W(y, z|y', z') &= \min\left(1, e^{y-y'}\right) \\
W(y, z|y, z') &= \min\left(1, e^{z-z'}\right).
\end{aligned} \tag{3.12}$$

By defining N_0 and N in accordance to what was done in the previous example, the value of the sum is then approximated by

$$1 + \int_a^b dx e^{-x} + \int_{a'}^{b'} dy \int_{a''}^{b''} dz e^{-y-z} = 1 + \frac{N - N_0}{N_0}. \tag{3.13}$$

3.2 Bare scheme for simulating \mathcal{G}

The task at hand is now to implement the DMC method in order to calculate the electronic single-particle Green's function $\mathcal{G}(\alpha, \mu, \mathbf{p}, \tau)$. The integrals series (3.1) will then be nothing but the diagrammatic series (2.61), with the external parameters $\{y\} = \{\alpha, \mu, \mathbf{p}, \tau\}$. The integration variables x_i 's must therefore correspond to the internal imaginary times and momenta, where the internal momenta are chosen to be those of the phonon propagators. Representing the internal momenta in spherical coordinates $\mathbf{q} = (q \sin \theta \cos \varphi, q \sin \theta \sin \varphi, q \cos \theta)$, the momentum integrals should be replaced according to

$$\int \frac{d^3 q}{(2\pi)^3} \rightarrow \int_{q=0}^{\infty} \int_{\theta=0}^{\pi} \int_{\varphi=0}^{2\pi} \frac{q^2 \sin \theta dq d\theta d\varphi}{(2\pi)^3}. \tag{3.14}$$

The beauty of this is realized when recalling that each phonon brings with it a factor $V(q)^2 \propto q^{-2}$, whose momentum dependence exactly cancel with scale factor of the spherical coordinates.

The expression corresponding the first order diagram then becomes

$$\begin{aligned}
& - \int_0^\tau d\tau_2 \int_0^{\tau_2} d\tau_1 \int_0^\infty dq \int_0^\pi d\theta \int_0^{2\pi} d\varphi \left[\mathcal{G}^{(0)}(\mathbf{p}, \tau_1) \mathcal{G}^{(0)}(\mathbf{p} - \mathbf{q}, \tau_2 - \tau_1) \right. \\
& \quad \left. \tilde{\mathcal{D}}^{(0)}(\mathbf{q}, \tau_2 - \tau_1) \mathcal{G}^{(0)}(\mathbf{p}, \tau - \tau_2) \right],
\end{aligned} \tag{3.15}$$

where $\tilde{\mathcal{D}}^{(0)}(\mathbf{q}, \tau)$ is a phonon propagator which has absorbed the factor $q^2 \sin \theta (2\pi)^{-3}$ originating from the integral, the interaction potential $V(q)^2$ along with the factor -1 from the Feynman rules. Thus

$$\tilde{\mathcal{D}}^{(0)}(\mathbf{q}, \tau) = \frac{2\sqrt{2}\pi\alpha}{(2\pi)^3} \sin \theta \exp\{-\tau\} \quad (3.16)$$

which is a quantity always larger than or equal to zero. The integrand of each and every integral in the integral series will be entirely made up out of $\mathcal{G}^{(0)}$'s and $\tilde{\mathcal{D}}^{(0)}$'s which implies that every contribution to \mathcal{G} is a positive contribution. This will simplify the DMC implementation since it won't be necessary to calculate what sign each sampled parameter space state comes with.

The external parameters \mathbf{p} and τ will be the only ones allowed to change during the Markov process. Including α and/or μ would cause the parameter space to increase and the statistics to be spread out. Thus more computation time would be needed to calculate quantities to the same level of certainty as having α and μ fixed.

3.2.1 Implementation

The value of the propagator \mathcal{G} will be computed at the discrete set of points $\mathbf{p}_i = \Delta p(0.5 + i) \hat{\mathbf{e}}_z$ and $\tau_j = \Delta\tau(0.5 + j)$ where $i = 0, 1, 2, \dots, N-1$, $j = 0, 1, 2, \dots, M-1$ and the resolution is chosen in terms of $\Delta p = p_{\max}/N$ and $\Delta\tau = \tau_{\max}/M$. To calculate $\mathcal{G}(\mathbf{p}_i, \tau_j) = \mathcal{G}_{i,j}$, both a bin N_0 and a two dimensional histogram N are used, even though \mathbf{p} and τ will be continuous variables in the Markov process. The bin $N_{i,j}$ of the histogram will then be covering the range $p \in [p_i - \Delta p, p_i + \Delta p]$ and $\tau \in [\tau_j - \Delta\tau, \tau_j + \Delta\tau]$ of the external parameter values, where $\Delta x \equiv \Delta x/2$ is introduced for a more convenient notation. The value of every bin in the histogram along with N_0 are initially put to zero. Then, each time a parameter space state is sampled, it will be checked whether or not this state belongs to the zeroth order term $\mathcal{G}^{(0)}(\mathbf{p}, \tau)$. If this is the case, the value of N_0 is increased by unity, if not, the bin in the histogram according to the external parameters is instead increased by unity. By doing this, the quantities N_0 and $N_{i,j}$ can be shown to be proportional to

$$\begin{aligned} N_0 &\propto \int_0^{N\Delta p} dp \int_0^{M\Delta p} d\tau \mathcal{G}^{(0)}(\mathbf{p}, \tau) \\ &= \Delta p \Delta\tau \sum_{k,l} \mathcal{G}^{(0)}(\mathbf{p}_k, \tau_l) + \mathcal{O}([\Delta p]^3 + [\Delta\tau]^3) \end{aligned} \quad (3.17)$$

and

$$\begin{aligned}
 N_{i,j} &\propto \int_{p_i - \Delta p}^{p_i + \Delta p} dp \int_{\tau_j - \Delta \tau}^{\tau_j + \Delta \tau} d\tau \left[\mathcal{G}(\mathbf{p}, \tau) - \mathcal{G}^{(0)}(\mathbf{p}, \tau) \right] \\
 &= \Delta p \Delta \tau \left[\mathcal{G}(\mathbf{p}_i, \tau_j) - \mathcal{G}^{(0)}(\mathbf{p}_i, \tau_j) \right] + \mathcal{O}([\Delta p]^3 + [\Delta \tau]^3)
 \end{aligned} \tag{3.18}$$

respectively. Omitting the errors due to discretization, the interacting electronic propagator is then found to be

$$\mathcal{G}(\mathbf{p}_i, \tau_j) = \mathcal{G}^{(0)}(\mathbf{p}_i, \tau_j) + N_{i,j} \frac{\sum_{k,l} \tilde{\mathcal{G}}^{(0)}(\mathbf{p}_k, \tau_l)}{N_0}. \tag{3.19}$$

On the other hand, if the external momentum were to be held fixed at \mathbf{p}_0 , the value of \mathcal{G} at the set of imaginary times $\{\tau_j\}$ would similarly become

$$\mathcal{G}(\mathbf{p}_0, \tau_j) = \mathcal{G}^{(0)}(\mathbf{p}_0, \tau_j) + N_j \frac{\sum_l \mathcal{G}^{(0)}(\mathbf{p}_0, \tau_l)}{N_0}, \tag{3.20}$$

where the histogram N in such a case would be one dimensional.

Since the vertex contribution now is obtain in the $\tilde{\mathcal{D}}^{(0)}$'s, the start and endpoint of a propagator which might or might not connect to other propagators, are referred to as nodes. Each node is given an imaginary time where the leftmost and rightmost nodes have $\tau_0 = 0$ and $\tau_{2n+1} = \tau$ respectively whilst the other nodes have times in between in such a way that the chronologization constraint is fulfilled. Having the imaginary time stored within the nodes, the only variable needed to be stored within the propagators is their momentum.

Code-wise each node, $\tilde{\mathcal{D}}^{(0)}$ and $\mathcal{G}^{(0)}$ is an instance of their corresponding class. Each propagator have a reference to both the start and endpoint node, and similarly the nodes have information about to which propagators they are attached. Further more the $\mathcal{G}^{(0)}$'s are stored in a chronologically ordered list whilst the $\tilde{\mathcal{D}}^{(0)}$'s are stored in an unordered list.

3.2.2 Update procedures

What remains to be discussed is how the sampling of states in parameter space occurs. As the name Diagrammatic Monte Carlo suggest, the diagrammatic representation of the integral series will be used. That is, the function D_n in the integral series (3.1) is to be thought of as a Feynman diagram (without the integrals). The random walk, which is used to simulate the Markov process, will thus be in terms of such diagrams. It is then important that each and every such diagram must be possible to reach in order to cover all of parameter space so that ergodicity is satisfied. To make sure that this actually is the case, a set of update procedures [5] have been constructed, each of which has a probability p_i of being selected during the Markov process.

Change of diagram length in time, type 1

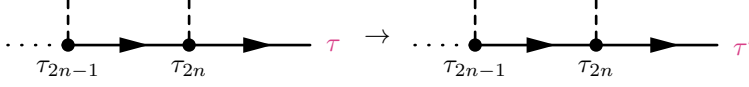


Figure 3.4: The only affected parameter is the highlighted imaginary time of the end point node.

This update procedure merely changes the external imaginary time parameter τ , which is nothing but the diagram length in time. In the first update type this is achieved by altering the time of the end point node in the diagram, i.e. $\tau \rightarrow \tau'$, as illustrated in figure 3.4. The only affected quantity of such an update will be the value of the very last $\mathcal{G}^{(0)}$ in the diagram so that

$$\frac{D_n(\tau')}{D_n(\tau)} = \frac{\mathcal{G}^{(0)}(\mathbf{p}, \tau' - \tau_{2n})}{\mathcal{G}^{(0)}(\mathbf{p}, \tau - \tau_{2n})} = \frac{\exp \left\{ - \left(\frac{p^2}{2} - \mu \right) \tau' \right\}}{\exp \left\{ - \left(\frac{p^2}{2} - \mu \right) \tau \right\}}. \quad (3.21)$$

Now consider an exponential distribution on the interval $[\tau_{2n}, \tau_{\max}]$ with rate parameter $\lambda = p^2/2 - \mu$ of which the density is

$$\rho(\tau) = \frac{\lambda e^{-\lambda(\tau - \tau_{2n})}}{1 - e^{-\lambda(\tau_{\max} - \tau_{2n})}}. \quad (3.22)$$

By sampling τ' from such a distribution, the ratio $W(\tau'|\tau)/W(\tau|\tau')$ will be the inverse of D'_n/D_n . Hence the acceptance ratio $A(\tau|\tau')$ of this update procedure becomes unity so that any proposed τ' always is accepted.

Change of diagram length in time, type 2

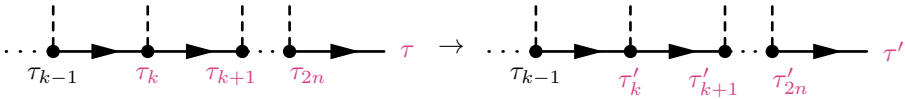


Figure 3.5: The highlighted τ 's are the parameters affected by this update.

This update procedure also changes the external imaginary time parameter, although it does so in a slightly different manner by letting any $\mathcal{G}^{(0)}$ in the diagram be lengthen or shortened in time, not just the last one. This is achieved using an

uniform probability to pick any but the leading node in the diagram to assign a new imaginary time τ'_k from the interval $[\tau_{k-1}, \tau_{\max} - (\tau - \tau_k)]$. In order to only modify the length of the electronic propagator just in front of the chosen node, every node proceeding this node must clearly have the difference $\tau'_k - \tau_k$ added to its time. This is illustrated in figure 3.5.

This update does not merely affect the one $\mathcal{G}^{(0)}$, but phonon propagators with start and end points on different sides of the chosen node would also have their length modified by the difference $\tau'_k - \tau_k$. If there are m such phonons, the quota of the diagram values become

$$\begin{aligned} \frac{D_n(\tau')}{D_n(\tau)} &= \frac{\mathcal{G}^{(0)}(\mathbf{p}, \tau_k - \tau_{k-1}) \prod_{i=0}^{m-1} \tilde{\mathcal{D}}^{(0)}(\mathbf{q}_i, \Delta\tau_i)}{\mathcal{G}^{(0)}(\mathbf{p}, \tau'_k - \tau_{k-1}) \prod_{j=0}^{m-1} \tilde{\mathcal{D}}^{(0)}(\mathbf{q}_j, \Delta\tau_j + [\tau'_k - \tau_k])} \\ &= \frac{\exp\left\{-\left(\frac{p^2}{2} - \mu + m\right)\tau'_k\right\}}{\exp\left\{-\left(\frac{p^2}{2} - \mu + m\right)\tau_k\right\}}, \end{aligned} \quad (3.23)$$

where $\Delta\tau_i$ is the length in time of the i th phonon propagator. By sampling the τ'_k from an exponential distribution with rate parameter $\lambda = p^2/2 - \mu + m$, the acceptance ration for this update procedure also becomes unity.

This second version of the change of diagram length update procedure is more complex than the first one, and may therefore be chosen less often. In a worst case scenario the complexity scales as $\mathcal{O}(n)$, due to figuring out the number of phonons m just discussed. Only one of the procedures changing the length of the diagram would be sufficient, but having an over complete set of update procedures is necessarily not something negative and could potentially enhance the statistics.

Change of external momentum

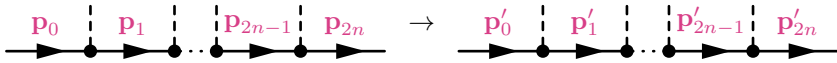


Figure 3.6: This update procedure changes the momentum of every $\mathcal{G}^{(0)}$ in the diagram by the external momentum difference $\mathbf{p}' - \mathbf{p}$. Surely it must be the case that $\mathbf{p}_0 = \mathbf{p}_{2n} = \mathbf{p}$ and the same is of course true for the primed momenta as well.

Since there is no preferred direction of the Hamiltonian (2.51), the Green's function \mathcal{G} becomes dependent merely upon the magnitude of the external momentum \mathbf{p} . This update procedure is thus constructed to keep the direction constant while

changing only the magnitude $p \rightarrow p'$. In order to satisfy momentum conservation at each vertex, the $\mathcal{G}^{(0)}$'s are chosen to absorb the external momentum difference $\mathbf{p}' - \mathbf{p}$ leaving the value of the $\tilde{\mathcal{D}}^{(0)}$'s constant. This is illustrated in figure 3.6. The ratio of the diagram value after to before such an update then becomes

$$\begin{aligned} \frac{D_n(\mathbf{p}')}{D_n(\mathbf{p})} &= \frac{\prod_{i=0}^{2n} \mathcal{G}^{(0)}(\mathbf{p}'_i, \tau_{i+1} - \tau_i)}{\prod_{j=0}^{2n} \mathcal{G}^{(0)}(\mathbf{p}_j, \tau_{j+1} - \tau_j)} \\ &= \exp \left\{ -\frac{1}{2} \sum_{i=0}^{2n} \left([\mathbf{p}_i + (\mathbf{p}' - \mathbf{p})]^2 - p_i^2 \right) (\tau_{i+1} - \tau_i) \right\} \\ &= \exp \left\{ -\frac{\tau}{2} ([p' - p]^2 + 2\langle \mathbf{p} \rangle_{0,2n} \cdot [\mathbf{p}' - \mathbf{p}]) \right\} \end{aligned} \quad (3.24)$$

where the mean electronic momentum is defined as

$$\langle \mathbf{p} \rangle_{k,l} \equiv \sum_{i=k}^l \frac{\tau_{i+1} - \tau_i}{\tau} \mathbf{p}_i. \quad (3.25)$$

By sampling $p' \in [0, p_{\max}]$ using a truncated half-normal distribution whose corresponding normal distribution would have the standard deviation $\sigma = 1/\sqrt{\tau}$, the quotient of the proposal distributions takes the value

$$\frac{W(\mathbf{p}'|\mathbf{p})}{W(\mathbf{p}|\mathbf{p}')} = \exp \left\{ -\frac{\tau}{2} (p^2 - p'^2) \right\} \quad (3.26)$$

so that the acceptance ratio is found to be

$$\begin{aligned} A(p|p') &= \min \left(1, \exp \left\{ -(\mathbf{p}' - \mathbf{p}) \cdot (\langle \mathbf{p} \rangle_{0,2n} - \mathbf{p}) \tau \right\} \right) \\ &= \min \left(1, \exp \left\{ -(p' - p) (\langle p_z \rangle_{0,2n} - p) \tau \right\} \right). \end{aligned} \quad (3.27)$$

In the final equality the vectors has ben represented in a Cartesian coordinate system with the z -axis parallel to the external momentum. On average $\langle p_z \rangle_{0,2n}$ should not differ too much from p implying that the acceptance ration should be close to unity most of the time.

Change of transferred momentum magnitude

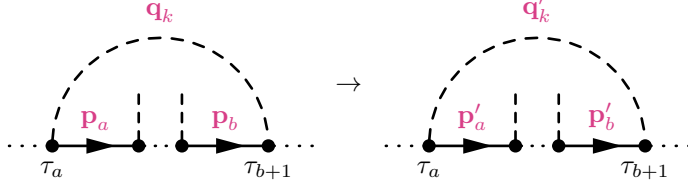


Figure 3.7: The momentum transferred via an internal phonon propagator is updated. In order obey momentum conservation at every vertex, electronic propagators beneath the phonon arc absorb the momentum difference.

This update procedure is similar to that of the external momentum, the main difference of course being that the magnitude of momentum transferred via a phonon propagator is updated rather than the external momentum. In order to achieve this, a $\tilde{\mathcal{D}}^{(0)}$ is uniformly randomly selected and assigned a new momentum magnitude $q_k \rightarrow q'_k$ while keeping the direction fixed. In order to conserve momentum at the two vertices connected to the phonon propagator, the $\mathcal{G}^{(0)}$'s located beneath the phonon arc should absorb the momentum difference $\mathbf{q}_k - \mathbf{q}'_k$. This is illustrated in figure 3.7. Since the $\tilde{\mathcal{D}}^{(0)}(\mathbf{q}, \tau)$'s does not depend on the magnitude $q = |\mathbf{q}|$, one has that

$$\begin{aligned}
 \frac{D_n(\mathbf{q}'_k)}{D_n(\mathbf{q}_k)} &= \frac{\prod_{i=a}^b \mathcal{G}^{(0)}(\mathbf{p}'_i, \tau_{i+1} - \tau_i)}{\prod_{j=a}^b \mathcal{G}^{(0)}(\mathbf{p}_j, \tau_{j+1} - \tau_j)} \\
 &= \exp \left\{ -\frac{1}{2} \sum_{i=a}^b \left([\mathbf{p}_i + (\mathbf{q}_k - \mathbf{q}'_k)]^2 - p_i^2 \right) (\tau_{i+1} - \tau_i) \right\} \\
 &= \exp \left\{ -\frac{\tau_{b+1} - \tau_a}{2} ([q_k - q'_k]^2 + 2\langle \mathbf{p} \rangle_{a,b} \cdot [\mathbf{q}_k - \mathbf{q}'_k]) \right\},
 \end{aligned} \tag{3.28}$$

which indeed is similar to (3.24). Following in the footsteps of the previous update procedure, $q'_k \in [0, \infty[$ is sampled from a half-normal distribution whose corresponding normal distribution would have the standard deviation $\sigma = 1/\sqrt{\tau_{b+1} - \tau_a}$. The acceptance ration is then found to be,

$$A(\mathbf{q}_k | \mathbf{q}'_k) = \min \left(1, \exp \left\{ -(\mathbf{q}_k - \mathbf{q}'_k) \cdot (\langle \mathbf{p} \rangle_{a,b} + \mathbf{q}_k) [\tau_{b+1} - \tau_a] \right\} \right). \tag{3.29}$$

It is reasonable to assume that on average, $\langle \mathbf{p} \rangle_{a,b} + \mathbf{q}_k$ does not differ too much from the external momentum \mathbf{p} . Hence this update procedure should have an acceptance

ration close to unity at low external momenta whilst performing worse at higher external momenta.

Change of transferred momentum direction

This update procedure changes the direction $(\theta_k, \varphi_k) \rightarrow (\theta'_k, \varphi'_k)$ of the momentum transferred via a phonon propagator. As in the previous update procedure, the electronic propagators below the phonon arc absorb the momentum difference $\mathbf{q}_k - \mathbf{q}'_k$ which again is illustrated in figure 3.7. This time, since $\tilde{\mathcal{D}}^{(0)} \propto \sin \theta$ the ratio of the diagram values becomes slightly different

$$\begin{aligned} \frac{D_n(\mathbf{q}'_k)}{D_n(\mathbf{q}_k)} &= \frac{\sin \theta'_k \prod_{i=a}^b \mathcal{G}^{(0)}(\mathbf{p}'_i, \tau_{i+1} - \tau_i)}{\sin \theta_k \prod_{j=a}^b \mathcal{G}^{(0)}(\mathbf{p}_j, \tau_{j+1} - \tau_j)} \\ &= \frac{\sin \theta'_k}{\sin \theta_k} \exp \left\{ -\frac{\tau_{b+1} - \tau_a}{2} ([\mathbf{q}_k - \mathbf{q}'_k]^2 + 2\langle \mathbf{p} \rangle_{a,b} \cdot [\mathbf{q}_k - \mathbf{q}'_k]) \right\}. \end{aligned} \quad (3.30)$$

By sampling the azimuthal angle uniformly on the interval $\varphi'_k \in [0, 2\pi]$, and the polar angle $\theta'_k \in [0, \pi]$ from a probability distribution whose density $\rho(\theta'_k) = \frac{1}{2} \sin \theta'_k$, one obtains the acceptance ratio

$$A(\mathbf{q}_k | \mathbf{q}'_k) = \min \left(1, \exp \left\{ -\frac{\tau_{b+1} - \tau_a}{2} ([\mathbf{q}_k - \mathbf{q}'_k]^2 + 2\langle \mathbf{p} \rangle_{a,b} \cdot [\mathbf{q}_k - \mathbf{q}'_k]) \right\} \right). \quad (3.31)$$

Vertex shift in time

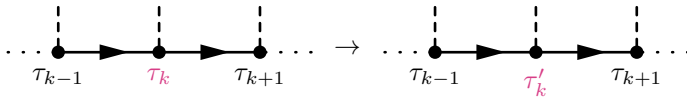


Figure 3.8: The imaginary time of internal node k is updated.

This update procedure changes the imaginary time $\tau_k \rightarrow \tau'_k$ of a randomly chosen internal node whilst keeping the chronological ordering, i.e. $\tau_{k-1} < \tau'_k < \tau_{k+1}$. The procedure is illustrated in figure 3.8 and, as easily may be seen, does only affect the three propagators connected to the selected node. Hence

$$\begin{aligned} \frac{D_n(\tau'_k)}{D_n(\tau_k)} &= \frac{\mathcal{G}^{(0)}(\mathbf{p}_{k-1}, \tau'_k - \tau_{k-1}) \mathcal{G}^{(0)}(\mathbf{p}_k, \tau_{k+1} - \tau'_k) \tilde{\mathcal{D}}^{(0)}(\mathbf{q}_k, \pm(\tau_l - \tau'_k))}{\mathcal{G}^{(0)}(\mathbf{p}_{k-1}, \tau'_k - \tau_{k-1}) \mathcal{G}^{(0)}(\mathbf{p}_k, \tau_{k+1} - \tau_k) \tilde{\mathcal{D}}^{(0)}(\mathbf{q}_k, \pm(\tau_l - \tau_k))} \\ &= \exp \left\{ -\left[\frac{p_{k-1}^2}{2} - \frac{p_k^2}{2} \mp 1 \right] (\tau' - \tau) \right\}. \end{aligned} \quad (3.32)$$

Here the upper sign is used if $\tau_l > \tau_k$, meaning that the phonon propagator is leaving to node l from node k . If instead $\tau_l < \tau_k$, the lower sign should be used and the situation becomes the opposite. By sampling τ'_k from the interval $[\tau_{k-1}, \tau_{k+1}]$ using an exponential distribution with rate parameter $\lambda = p_{k-1}^2/2 - p_k^2/2 \mp 1$, the acceptance ration becomes unity.

Change of diagram structure

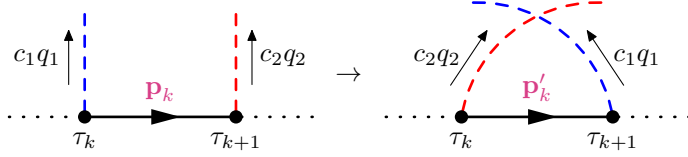


Figure 3.9: The diagram structure is modified by interchanging the phonon propagators connected to two neighboring nodes.

This update procedure, as illustrated in figure 3.9, interchange the two phonon propagators connected to a pair of randomly selected neighboring nodes. In order to conserve momentum, the $\mathcal{G}^{(0)}$ connected to both of the selected nodes must absorb the momentum difference $\mathbf{p}'_k - \mathbf{p}_k = c_1 \mathbf{q}_1 - c_2 \mathbf{q}_2$. Here the c_i tells whether the $\tilde{\mathcal{D}}_i^{(0)}$ is propagating towards the node to be swapped ($c_i = -1$) or if it is propagating away from ($c_i = 1$). The ratio of the diagram value prior to and after the update then becomes

$$\begin{aligned} \frac{D_n(\xi'_n)}{D_n(\xi_n)} &= \frac{\tilde{\mathcal{D}}^{(0)}(\mathbf{q}_1, c_1[\tau_i - \tau_{k+1}]) \tilde{\mathcal{D}}^{(0)}(\mathbf{q}_2, c_2[\tau_j - \tau_k]) \mathcal{G}^{(0)}(\mathbf{p}'_k, \tau_{k+1} - \tau_k)}{\tilde{\mathcal{D}}^{(0)}(\mathbf{q}_1, c_1[\tau_i - \tau_k]) \tilde{\mathcal{D}}^{(0)}(\mathbf{q}_2, c_2[\tau_j - \tau_{k+1}]) \mathcal{G}^{(0)}(\mathbf{p}_k, \tau_{k+1} - \tau_k)} \\ &= \exp \left\{ - \left[\frac{(\mathbf{p}_k + c_1 \mathbf{q}_1 - c_2 \mathbf{q}_2)^2}{2} - \frac{p_k^2}{2} - c_1 + c_2 \right] (\tau_{k+1} - \tau_k) \right\}. \end{aligned} \quad (3.33)$$

Other than the pair of neighboring nodes to be selected, there are no further sampling of parameters needed for this update procedure. By performing the selection of the nodes using a uniform distribution, $W(\xi_n|\xi'_n) = W(\xi'_n|\xi_n)$ and the update procedure should then be accepted according to

$$A(\xi_n|\xi'_n) = \min \left(1, \frac{D_n(\xi'_n)}{D_n(\xi_n)} \right). \quad (3.34)$$

Change of diagram order

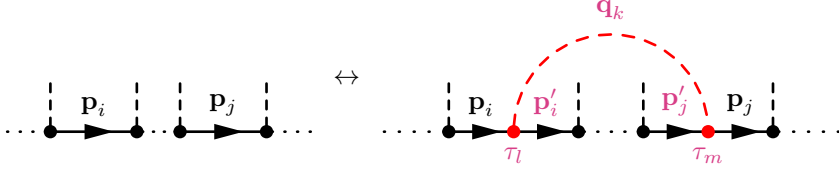


Figure 3.10: An illustration of the change of diagram order procedure.

This final update procedure which is illustrated in figure 3.10, is the only one which changes the order of the diagram at hand. To increase the diagram order, an electronic propagator $\mathcal{G}_i^{(0)}$ is selected on random and then split at a time τ_l , which is sampled uniformly on the interval $[\tau_i, \tau_{i+1}]$. After this, another imaginary time τ_m is sampled on the interval $\tau_m \in [\tau_l, \tau]$ using an exponential distribution with a rate parameter $\lambda = 1$. The $\mathcal{G}_j^{(0)}$ which happen to occupy the imaginary time τ_m is split in twice at that point as well. For each of the two times τ_l and τ_m , a node is inserted so that the loose ends of the $\mathcal{G}^{(0)}$'s have something to connect to. The two newly introduced nodes are then further connected to a new phonon propagator $\tilde{\mathcal{D}}^{(0)}$, for which the momentum \mathbf{q}_k is sampled according to the *change of transferred momentum* procedures introduced earlier. In order to obey momentum conservation at each node, the $\mathcal{G}^{(0)}$'s under the newly added phonon arc have their momentum subtracted by \mathbf{q}_k . In this way, the probability distribution of increasing the diagram order becomes

$$\begin{aligned}
 W(n|n+1) &= P_R(n) \frac{1}{2n+1} \frac{1}{\tau_{i+1} - \tau_i} \frac{e^{-(\tau_m - \tau_l)}}{1 - e^{-(\tau - \tau_l)}} \frac{\sin \theta_k}{2} \frac{1}{2\pi} \\
 &\times \sqrt{\frac{2(\tau_m - \tau_l)}{\pi}} \exp \left\{ -\frac{q_k^2}{2} (\tau_m - \tau_l) \right\}.
 \end{aligned} \tag{3.35}$$

Here $P_R(n)$ is the probability of choosing to raise the diagram order once having selected the *change of diagram order* procedure. Of course the corresponding probability of choosing to lower the diagram order is then nothing but $1 - P_R(n)$. Further

more, the ratio of the diagram value prior to and after the update is realized to be

$$\begin{aligned} \frac{D_{n+1}}{D_n} &= \tilde{\mathcal{D}}^{(0)}(\mathbf{q}_k, \tau_m - \tau_l) \frac{\prod_{i=l}^{m-1} \mathcal{G}^{(0)}(\mathbf{p}_i - \mathbf{q}_k, \tau_{i+1} - \tau_i)}{\prod_{i=l}^{m-1} \mathcal{G}^{(0)}(\mathbf{p}_i, \tau_{i+1} - \tau_i)} \\ &= \frac{2\sqrt{2}\pi\alpha}{(2\pi)^3} \sin \theta_k \exp \left\{ - \left[\frac{q_k^2}{2} + 1 - \langle \mathbf{p} \rangle_{l,m-1} \cdot \mathbf{q}_k \right] (\tau_m - \tau_l) \right\}. \end{aligned} \quad (3.36)$$

The procedure of lowering the diagram order is much more simplistic; it is only necessary to randomly pick a $\tilde{\mathcal{D}}^{(0)}$ which is to be removed. Hence $W(n+1|n) = (1 - P_R(n+1)) [n+1]^{-1}$, and by introducing the quantity

$$\begin{aligned} R(n|n+1) &= \frac{D_{n+1}}{D_n} \frac{W(n+1|n)}{W(n|n+1)} \\ &= \frac{1 - P_R(n+1)}{P_R(n)} \frac{\alpha}{\sqrt{\pi}} \frac{2n+1}{n+1} \frac{\tau_{i+1} - \tau_i}{\sqrt{\tau_m - \tau_l}} \\ &\times \left[1 - e^{-(\tau - \tau_l)} \right] \exp \left\{ [\langle \mathbf{p} \rangle_{l,m-1} \cdot \mathbf{q}_k] (\tau_m - \tau_l) \right\}, \end{aligned} \quad (3.37)$$

the acceptance ratios may be expressed as

$$A(n|n+1) = \min(1, R(n|n+1)) \quad , \quad A(n+1|n) = \min(1, 1/R(n|n+1)) \quad . \quad (3.38)$$

By requiring that

$$\frac{1 - P_R(n+1)}{P_R(n)} = \frac{\sqrt{\pi}}{2\alpha} \quad \Rightarrow \quad P_R(n) = P_R = \left[1 + \frac{\sqrt{\pi}}{2\alpha} \right]^{-1} \quad (3.39)$$

these acceptance ratios become independent of the coupling constant α and less dependent of the diagram order n

Clearly it should not be possible to lower the diagram order any further than $n = 0$. Also, one could think of implementing a maximum order n_{\max} for which the diagram order should not be able to rise above. To achieve this, it is extremely important not to set $P_R = 1$ and $P_R = 0$ at $n = 0$ and $n = n_{\max}$ respectively, since this would ruin the detailed balance. Rather one should approach this by simply refusing such an update. For example, if the procedure to increase the diagram order happen to be chosen when $n = n_{\max}$, it should be refused and a new update procedure chosen instead.

3.2.3 Results

Here follow some results obtained when simulating \mathcal{G} using the bare scheme update procedures described above. The external momentum \mathbf{p} has been fixed during these

simulations in order to not spread out the statistics over external parameters for which the data would not have been shown.

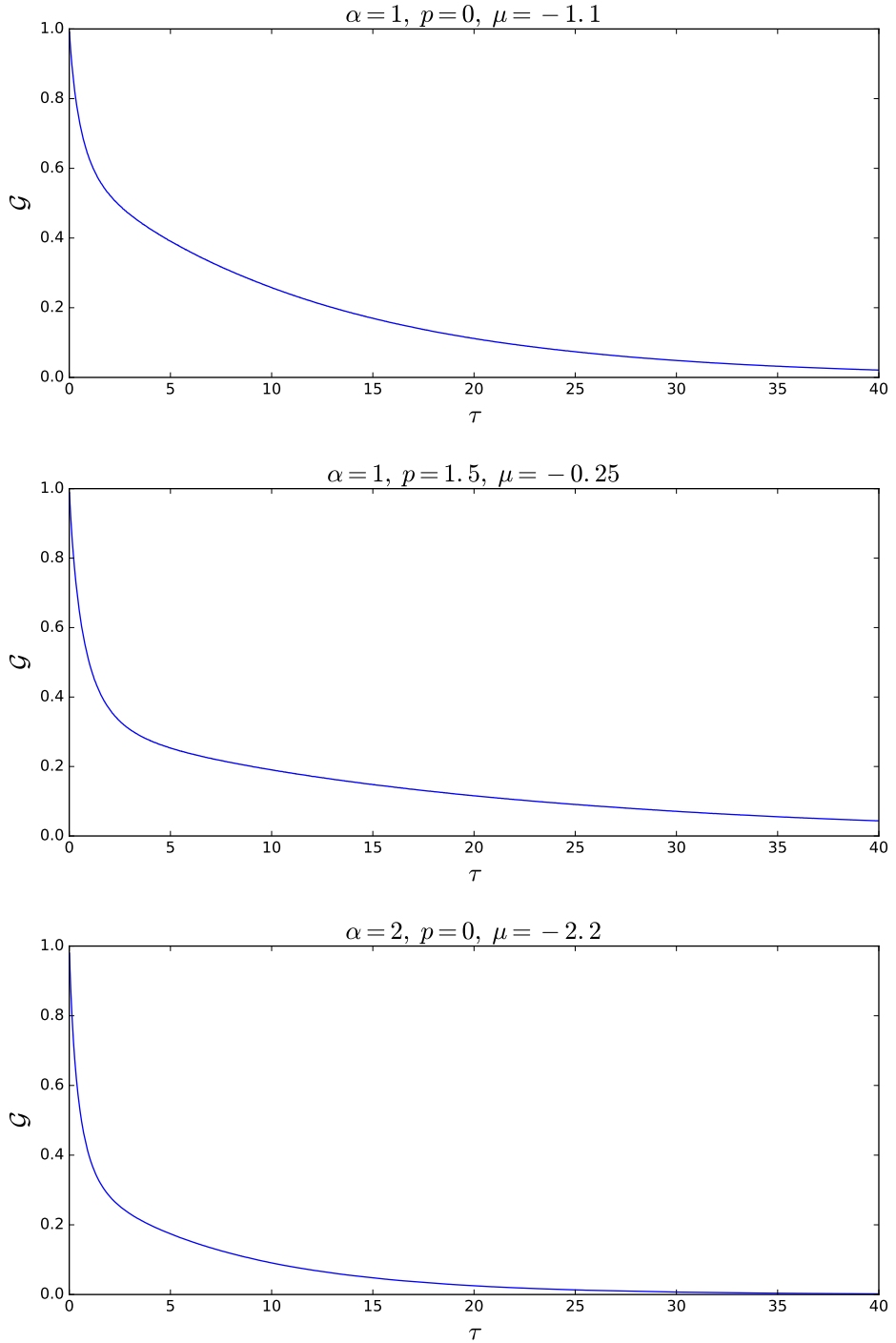


Figure 3.11: The acquired value of $\mathcal{G}(p = 0, \tau)$ after 80 minutes of core time. Here $\tau_{max} = 40$ and $\Delta\tau = 0.02$ has been used.

τ	$\mathcal{G}(0, 1, -1.1)$	$\mathcal{G}(1.5, 1, -0.25)$	$\mathcal{G}(0, 2, -2.2)$
0.01	0.9906	0.9881	0.9797
1.01	0.6242	0.4938	0.3922
2.01	0.5225	0.3631	0.2808
3.01	0.4673	0.3066	0.2314
4.01	0.4259	0.2745	0.1993
5.01	0.3907	0.2528	0.1738
6.01	0.359	0.2365	0.1524
7.01	0.3301	0.223	0.1339
8.01	0.3041	0.2113	0.1176
9.01	0.2797	0.2003	0.1031
10.01	0.2573	0.1902	0.09057
11.01	0.2374	0.1806	0.07967
12.01	0.2175	0.1715	0.07009
13.01	0.2003	0.1635	0.0617
14.01	0.1844	0.1552	0.05428
15.01	0.1695	0.1476	0.04763
16.01	0.156	0.1409	0.04189
17.01	0.1436	0.1341	0.03696
18.01	0.1319	0.1276	0.03243
19.01	0.1213	0.1216	0.02866
20.01	0.1116	0.1157	0.02498
21.01	0.1025	0.1103	0.02211
22.01	0.09434	0.1051	0.01937
23.01	0.08689	0.09985	0.01701
24.01	0.07983	0.09523	0.01492
25.01	0.07363	0.0909	0.01322
26.01	0.06764	0.08651	0.01168
27.01	0.06217	0.0825	0.01027
28.01	0.05718	0.07844	0.009083
29.01	0.05272	0.07471	0.007966
30.01	0.04861	0.07102	0.007016
31.01	0.04458	0.06742	0.006182
32.01	0.04098	0.06404	0.005393
33.01	0.03794	0.06131	0.004762
34.01	0.03482	0.05836	0.00411
35.01	0.0319	0.05525	0.003671
36.01	0.02945	0.05269	0.003204
37.01	0.02723	0.05022	0.002901
38.01	0.02509	0.04788	0.002536
39.01	0.02288	0.04576	0.002207
39.99	0.02102	0.04357	0.001962

Table 3.1: Some values of $\mathcal{G}(p, \alpha, \mu)$ from the plots in figure 3.11.

3.3 Bare scheme for simulating Σ^*

Rather than calculating $\mathcal{G}(\mathbf{p}, \tau)$ directly using DMC, it is also possible to instead simulate the proper self-energy $\Sigma^*(\mathbf{p}, \tau)$, from which the electronic propagator then is calculated using the Dyson equation (2.67). In order to do this, the random walk must now cover diagrams without external legs but also be able to reach the bare propagator $\mathcal{G}^{(0)}$ for normalization purposes. This is easily accomplished by a slight modification of some of the update procedures introduced in the previous section, and will be discussed in more detail shortly.

However, before that, it is important to realize that no longer all types of diagrams of order $n > 0$ should be binned. That is, to calculate Σ^* it is critical that the histogram merely have contributions from irreducible diagrams. Then, in similarity to (3.19) and (3.20) the value of Σ^* is obtained in terms of N_0 and N in the following way

$$\Sigma^*(\mathbf{p}_i, \tau_j) = N_{i,j} \frac{\sum_{k,l} \mathcal{G}^{(0)}(\mathbf{p}_k, \tau_l)}{N_0}, \quad \Sigma^*(\mathbf{p}_0, \tau_j) = N_j \frac{\sum_l \mathcal{G}^{(0)}(\mathbf{p}_0, \tau_l)}{N_0}. \quad (3.40)$$

An easy way to check whether or not a diagram is irreducible, is to store the current momentum of every $\mathcal{G}^{(0)}$ present in the diagram within a hash table. If one or more momenta are found to be equal to that of the external momentum, the diagram must clearly be reducible and should thus not be binned. Since the complexity of a search in a hash table is $\mathcal{O}(1)$, this implementation should not limit the performance of the algorithm. To recapitulate, all self-energy diagrams (together with the bare propagator for normalization purposes) should be sampled, but only proper ones are allowed to increment the bins values $N_{i,j}$ of the histogram.

3.3.1 Update procedures

Returning to the update procedures, there are only two which need to be modified in order to incorporate(?) the changes required for this new scheme. The others stay the same but might have some trivial change of notation for quantities, such as $\langle \mathbf{p} \rangle_{0,2n} \rightarrow \langle \mathbf{p} \rangle_{0,2n-1}$ in the case of the *change of external momentum* procedure.

Change of diagram length in time, type 1

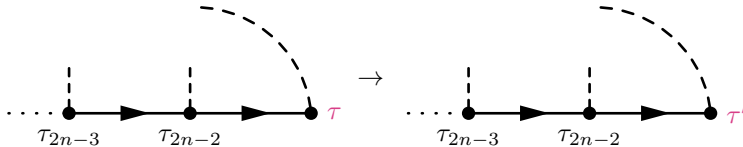


Figure 3.12: An illustration of the first kind of update procedure for changing the length of a diagram without external legs.

At $n > 0$, there is now a phonon propagator connected to the end point node of the diagram as depicted in figure 3.12. Thus, in accordance with the *change of diagram length in time, type 2* update procedure,

$$\frac{D_n(\tau')}{D_n(\tau)} = \exp \left\{ - \left[\frac{p^2}{2} - \mu + 1 \right] (\tau' - \tau) \right\}. \quad (3.41)$$

To maintain the acceptance ratio at unity, the only modification needed is to change the rate parameter of the distribution from which τ' is sampled, i.e. $\lambda \rightarrow \lambda' = \lambda + 1$.

Change of diagram order

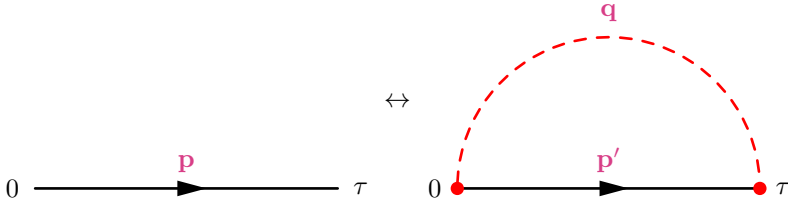


Figure 3.13: An illustration of the change of diagram order procedure between zeroth and first order diagrams.

In order to prevent generating diagrams with external legs, it is necessary only to modify the transition between a zeroth and a first order diagram. Instead of sampling two times where new nodes then will be inserted for the phonon to connect to, the already existing start and end point node of diagram will be used. This is illustrated in figure 3.13. Other than that this transition is no different from the ordinary *change of diagram order* update procedure so that

$$W(n = 0 | n = 1) = P_R \frac{\sin \theta_k}{2} \frac{1}{2\pi} \sqrt{\frac{2\tau}{\pi}} \exp \left\{ - \frac{q_k^2}{2} \tau \right\}. \quad (3.42)$$

The acceptance ratio may therefore be expressed as previously in (3.38) with

$$\begin{aligned} R(n = 0 | n = 1) &= \frac{D_{n=1}}{D_{n=0}} \frac{W(n = 1 | n = 0)}{W(n = 0 | n = 1)} \\ &= \frac{1 - P_R}{P_R} \frac{\alpha}{\sqrt{\pi}} \frac{1}{\sqrt{\tau}} \exp \{ [\langle \mathbf{p} \rangle_{l,m-1} \cdot \mathbf{q}_k - 1] \tau \}. \end{aligned} \quad (3.43)$$

The transitions between diagrams of order $n > 0$, as introduced in section 3.2.2, can not add any external legs since both the start and end point node of the diagram will be connected to phonons. However, there are now $2n - 1$ rather than $2n + 1$

number of $\mathcal{G}^{(0)}$'s to chose from when sampling the starting point time of the phonon propagator. Hence the " $2n + 1$ " in equation (3.35) and (3.37) should be replaced by " $2n - 1$ " to incorporate this.

3.3.2 The divergent diagram

It can be shown that the first order self-energy diagram $\Sigma^{*(1)}(\mathbf{p}, \tau)$ is proportional to $1/\sqrt{\tau}$ and thus diverges when $\tau \rightarrow 0$. It is not possible to capture such a behavior using a histogram since the function to be approximated has a too large second derivative in the vicinity of the singularity. To show this, consider the mean value of a function $f(x)$ on the interval $x_i - \Delta x < x < x_i + \Delta x$ (again $\Delta x \equiv \Delta x/2$ has been used) with $f(x_i)$ expanded in terms of the small parameter Δx , i.e.

$$\begin{aligned}
 & \frac{1}{\Delta x} \int_{x_i - \Delta x}^{x_i + \Delta x} f(t) dt \\
 &= \frac{1}{\Delta x} \int_{x_i - \Delta x}^{x_i + \Delta x} f(x_i + [t - x_i]) dt \\
 &= \frac{1}{\Delta x} \int_{x_i - \Delta x}^{x_i + \Delta x} [f(x_i) + f'(x_i)[t - x_i] + \frac{1}{2}f''(x_i)[t - x_i]^2 + \dots] dt \\
 &= f(x_i) + \frac{1}{24}f''(x_i)[\Delta x]^2 + \mathcal{O}([\Delta x]^4).
 \end{aligned} \tag{3.44}$$

In order for this mean value to be well approximated by $f(x_i)$, it is required that $f''(x_i)[\Delta x]^2 \ll f(x_i)$. However, in the case of $f(x) = 1/\sqrt{x}$ and $x_i = \Delta x$ this is not the case, no matter the size of Δx , since $f''(x_i)[\Delta x]^2 = 3\sqrt{2}/\sqrt{\Delta x}$ whilst $f(x_i) = 2/\sqrt{\Delta x}$. The ability of a histogram to approximate the function $1/\sqrt{x}$ in the vicinity of $x = 0$ is illustrated in figure 3.14.

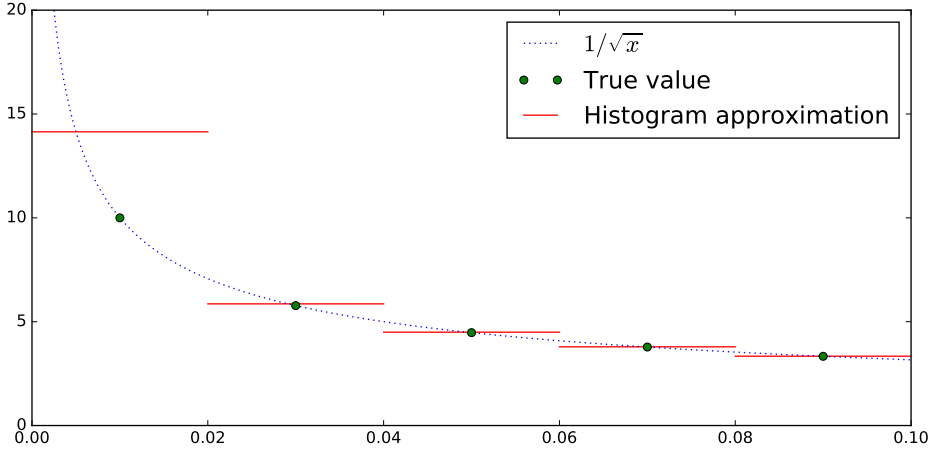


Figure 3.14: The function $1/\sqrt{x}$ approximated by a histogram with bin size $\Delta x = 0.02$ in the vicinity of $x = 0$. As can be seen, the approximative value at $x = 0.01$ is quite far off from the true one.

The true value of the first order self-energy diagram at zero external momentum is

$$\Sigma^{*(1)}(\mathbf{p} = \mathbf{0}, \tau) = \frac{\alpha}{\sqrt{\pi}} \frac{e^{-(1-\mu)\tau}}{\sqrt{\tau}} \quad \tau \geq 0. \quad (3.45)$$

When approximating this function with a histogram of bin size $\Delta\tau$, the value of the bin corresponding to τ_i becomes

$$\begin{aligned} \langle \Sigma^{*(1)}(\mathbf{p} = \mathbf{0}) \rangle_j &= \frac{1}{\Delta\tau} \int_{\tau_j - \Delta\tau}^{\tau_j + \Delta\tau} \Sigma^{*(1)}(\mathbf{p} = \mathbf{0}, t) dt \\ &= \frac{1}{\Delta\tau} \frac{\alpha}{\sqrt{1-\mu}} \left[\operatorname{erf} \left\{ \sqrt{(1-\mu)(\tau_j + \Delta\tau)} \right\} - \operatorname{erf} \left\{ \sqrt{(1-\mu)(\tau_j - \Delta\tau)} \right\} \right]. \end{aligned} \quad (3.46)$$

However, for external momentum $\mathbf{p} \neq \mathbf{0}$ it seems next to impossible to find an analytical expression of $\Sigma^{*(1)}(\mathbf{p}, \tau)$ due to cumbersome integrals. Nevertheless, by the usage of Monte Carlo integration these integrals may be calculated to an extremely good precision in a matter of seconds.

In order to find out whether a value of $\Sigma^{*(1)}(\mathbf{p}_i, \tau_j)$ should be calculated using DMC or Monte Carlo integration, it is reasonable to look at the difference $\Delta\Sigma_j^{*(1)} = \langle \Sigma^{*(1)}(\mathbf{p} = \mathbf{0}) \rangle_j - \Sigma^{*(1)}(\mathbf{p} = \mathbf{0}, \tau_j)$. For times $\tau_j < \tau_{\text{threshold}}$ where this difference is larger than a threshold value ε , Monte Carlo integration should be used, otherwise

DMC will be sufficient. The DMC code written during this master project has the threshold set to $\varepsilon = 0.001$. In table 3.2 the value of $\Delta\Sigma_j^{*(1)}$ is given for the first six j 's.

j	0	1	2	3	4	5	6
$\Delta\Sigma_j^{*(1)}$	2.34	0.0486	0.0133	0.0058	0.00314	0.00193	0.00129

Table 3.2: Here $\Delta\Sigma_j^{*(1)}$ is calculated for different values of j . The parameters used are $\alpha = 1$, $\mu = -1.1$ and $\Delta\tau = 0.02$.

It is crucial that there will be no contribution from $\Sigma^{*(1)}$ to the histogram N for times where it is calculated using Monte Carlo integration. However, to avoid such a double contribution it is as simple as to not bin a first order self-energy diagram if the length τ of which belongs to a bin $N_{i,j}$ of time $\tau_j < \tau_{\text{threshold}}$.

3.3.3 Results

Here follow some results obtained when simulating Σ^* using the bare scheme update procedures described above. Again the external momentum \mathbf{p} has been kept fixed during these simulations.

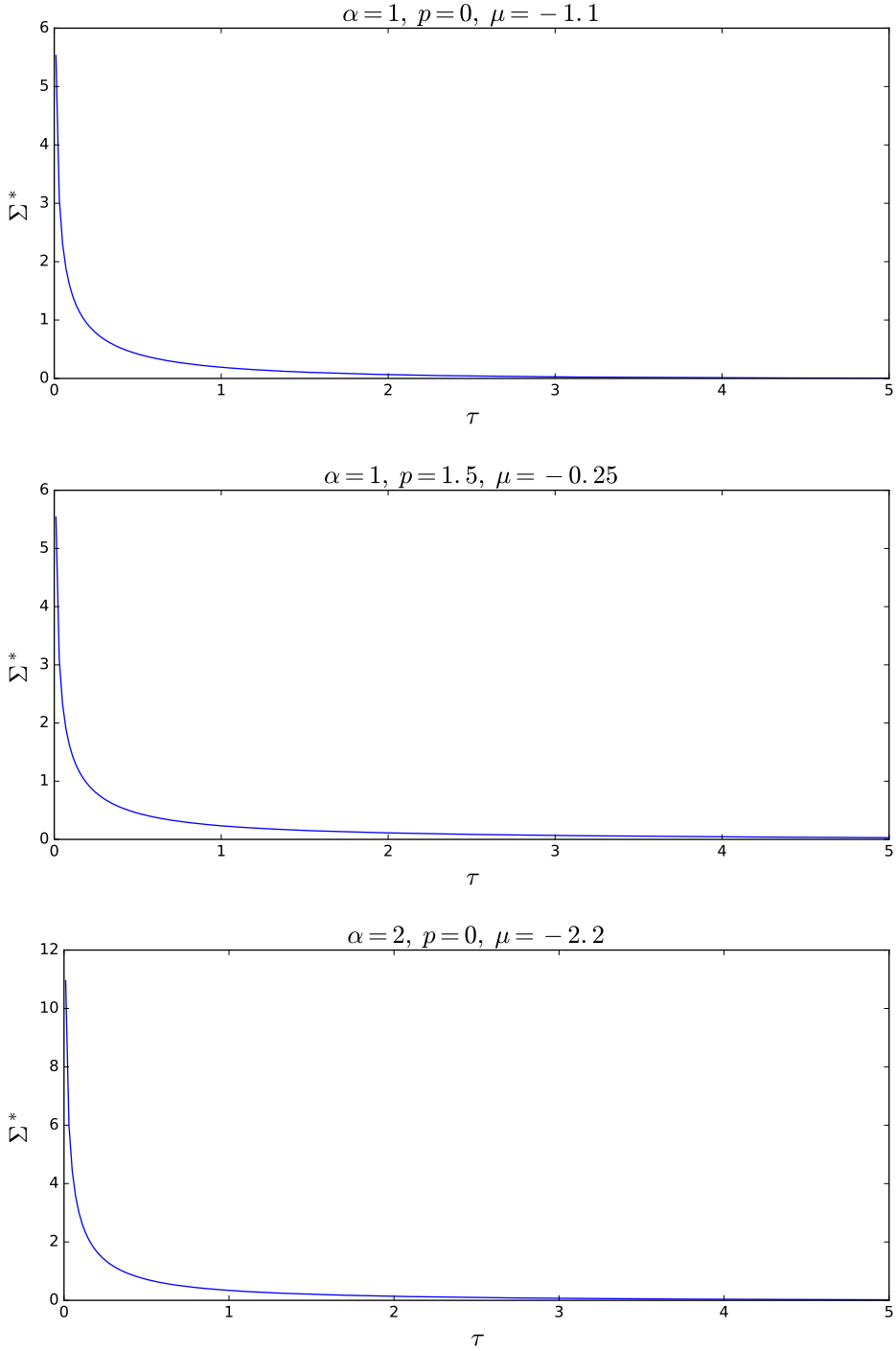


Figure 3.15: The acquired value of $\Sigma^*(p=0, 0 \leq \tau \leq 5)$ after 80 minutes of core time. Here $\tau_{max} = 40$ and $\Delta\tau = 0.02$ has been used.

τ	$\Sigma^*(0, 1, -1.1)$	$\Sigma^*(1.5, 1, -0.25)$	$\Sigma^*(0, 2, -2.2)$
0.01	5.531	5.537	10.96
0.21	0.892	0.9145	1.591
0.41	0.5063	0.5362	0.8721
0.61	0.3417	0.3757	0.5845
0.81	0.2484	0.2877	0.4318
1.01	0.1889	0.2312	0.3366
1.21	0.1481	0.1924	0.2724
1.41	0.1184	0.1638	0.2249
1.61	0.09575	0.1419	0.1887
1.81	0.07845	0.1248	0.1613
2.01	0.0643	0.1114	0.1377
2.21	0.05323	0.0994	0.1191
2.41	0.04421	0.08949	0.103
2.61	0.03667	0.08083	0.08986
2.81	0.03072	0.07354	0.07825
3.01	0.02576	0.06704	0.06804
3.21	0.02159	0.06117	0.05961
3.41	0.01814	0.05634	0.05227
3.61	0.01523	0.05141	0.046
3.81	0.01287	0.04739	0.04028
4.01	0.0109	0.04374	0.03547
4.21	0.009089	0.04027	0.03091
4.41	0.007704	0.03723	0.02729
4.61	0.006375	0.03454	0.02392
4.81	0.00551	0.03193	0.02108
4.99	0.004662	0.02981	0.01871

Table 3.3: Some values of $\Sigma^*(p, \alpha, \mu)$ from the plots in figure 3.15.

3.3.4 Numerically implementing Dyson equation

It is not entirely trivial how to implement Dyson equation when having to use a discrete Fourier transform. First of all, the proper self-energy must be transformed into frequency space, but due to the singularity at $\tau = 0$ it is not preferable to transform this quantity directly. However, knowing the analytical expression of this singular contribution, it can then be subtracted from the self-energy so that the discrete Fourier transform may be applied only to the resulting regular expression. The singular part is then Fourier transformed analytically and once in ω -space it is added to the transformed regular expression. That is,

$$\Sigma^*(\mathbf{p}_i, \omega_j) = \mathcal{F}_{\text{DFT}} \{ \Sigma^*(\mathbf{p}_i, \tau_j) - \Sigma^*_{\text{singular}}(\mathbf{p}_i, \tau_j) \} + \Sigma^*_{\text{singular}}(\mathbf{p}_i, \omega_j), \quad (3.47)$$

which is possible due to the linearity of the Fourier transform. A possible choice of the singular part is $\Sigma_{\text{singular}}^*(\mathbf{p}_i, \tau_j) = \Sigma^{*(1)}(\mathbf{p} = \mathbf{0}, \tau_j)$ for which the expression is (3.45) and thus

$$\Sigma_{\text{singular}}^*(\mathbf{p}_i, \omega_j) = \frac{\alpha}{\sqrt{1 - \mu + i\omega_j}}. \quad (3.48)$$

Having the proper self-energy in momentum and frequency space, Dyson equation is given by (2.67). However, it is not possible to directly transform back to $\mathcal{G}(\mathbf{p}_i, \tau_j)$ using the inverse discrete Fourier transform. This has to do with the fact that $\mathcal{G}(\mathbf{p}, \omega)$ falls off as $1/\omega$ when $\omega \rightarrow \infty$, which is too slow. Instead one may transform the difference

$$\Delta\mathcal{G}(\mathbf{p}, \omega) = \mathcal{G}(\mathbf{p}, \omega) - \mathcal{G}^{(0)}(\mathbf{p}, \omega) = \frac{\Sigma^*(\mathbf{p}, \omega)}{(i\omega + \xi(\mathbf{p}) - \Sigma^*(\mathbf{p}, \omega))(i\omega + \xi(\mathbf{p}))} \quad (3.49)$$

which has the proportionality $\Delta\mathcal{G}(\mathbf{p}, \omega \rightarrow \infty) \propto \omega^{-5/2}$ because $\Sigma^*(\mathbf{p}, \omega \rightarrow \infty) \propto \omega^{-1/2}$ and thus falls off fast enough. This ω dependence will also have the consequence that any high frequency noise present in $\Sigma^*(\mathbf{p}, \tau)$ will be greatly suppressed when transforming back the difference $\Delta\mathcal{G}$ to τ -space. Then, since also the inverse Fourier transform is linear, it follows that

$$\mathcal{F}_{DFT}^{-1} \{ \Delta\mathcal{G}(\mathbf{p}_i, \omega_j) \} = \Delta\mathcal{G}(\mathbf{p}_i, \tau_j) = \mathcal{G}(\mathbf{p}_i, \tau_j) - \mathcal{G}^{(0)}(\mathbf{p}_i, \tau_j). \quad (3.50)$$

The interacting electronic propagator in τ -space is finally obtained by

$$\mathcal{G}(\mathbf{p}_i, \tau_j) = \mathcal{G}^{(0)}(\mathbf{p}_i, \tau_j) + \Delta\mathcal{G}(\mathbf{p}_i, \tau_j). \quad (3.51)$$

In figure 3.16 the relative difference between the \mathcal{G}_{Σ^*} obtained using Dyson equation and the directly simulated \mathcal{G} is plotted against τ for both $\Delta\tau = 0.02$ and $\Delta\tau = 0.01$. As can be seen the difference is smaller than the size of $\Delta\tau$ in both cases. The agreement also seems to improve somewhat linearly with smaller $\Delta\tau$, the drawback is however more noise since there is less statistics contributing to each bin N_j .

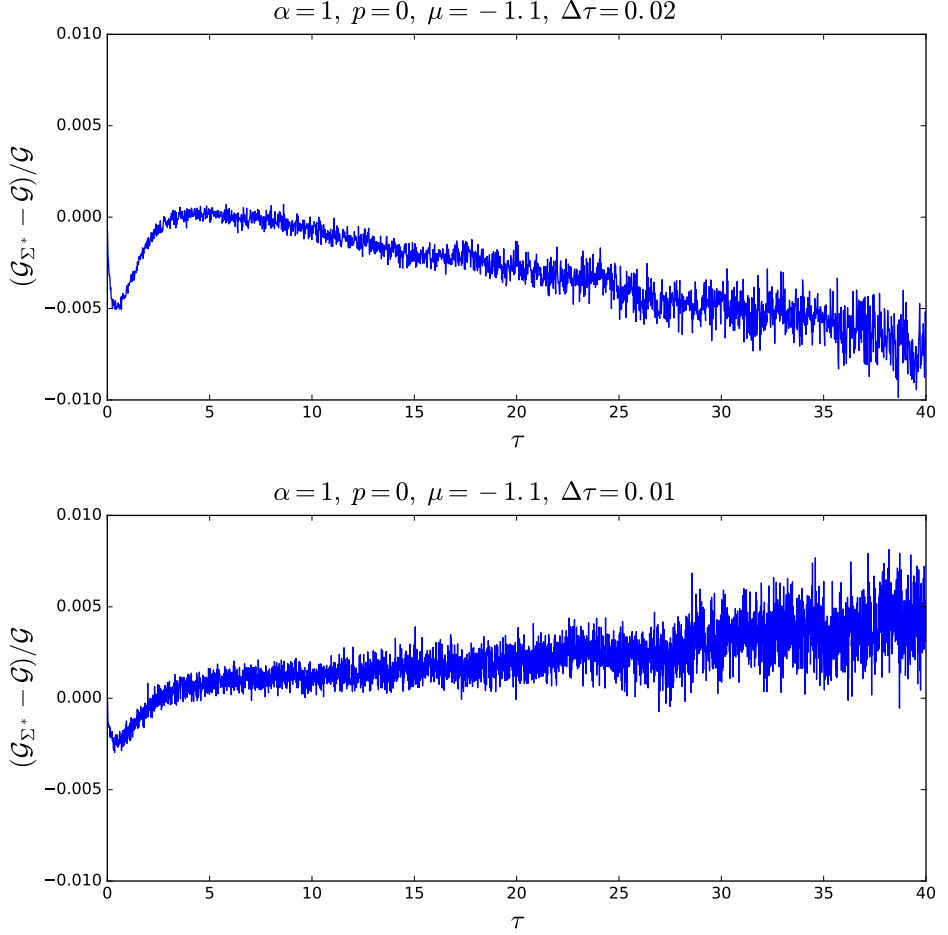


Figure 3.16: The relative difference between \mathcal{G}_{Σ^*} obtained using Dyson equation and the directly simulated \mathcal{G} . For each of these simulations a core time of 24 hours has been used.

3.4 Bold-line scheme

The bold-line scheme [17] is a self consistent scheme making use of bold-line tricks iteratively in order to partially or fully sum up a diagram series. Dyson equation is one such bold-line trick and is the only one to be investigated in this thesis.

Here the propagator $\mathcal{G}_{k+1} = \mathcal{G}^{(0)} + \Delta\mathcal{G}_{k+1}$ is obtained when employing Dyson equation to the $k + 1^{\text{th}}$ calculated self-energy S_{k+1} of the self consistent scheme. Rather than using the bare propagator when calculating S_{k+1} , the \mathcal{G}_k computed

in the previous iteration of the scheme is instead used. The constraint for which diagrams are allowed to contribute the self-energy of this scheme is thus stronger in order to prevent double counting. During the first iteration, when no propagator previously have been calculated, the bare one is used, i.e. $\mathcal{G}_0 = \mathcal{G}^{(0)}$. Given an appropriate choice of parameters, this scheme will converge so that $S_{m+1} \simeq S_m$ for some m . In practice, as will be shown, this convergence will happen after 4 or so iterations.

3.4.1 Skeleton diagrams

In order for certain diagrams to not contribute more than once to the \mathcal{G}_k , it is necessary to narrow down the class of allowed diagrams to a subclass of the proper self-energy diagrams, referred to as skeleton diagrams [18]. This class of diagrams is characterized by the lack of insertions, i.e. diagram parts which act like self-energies to some of the constituents of the diagram. It is easily realized, that the skeleton diagrams in the series of \mathcal{G} are particularly easy to identify. That is, if the phonon propagators of a self-energy diagram are entirely interconnected, the diagram is a skeleton one. Here interconnected phonon propagator is referred to those who intersect with at least another one when they are all drawn on one side of the straight line of electronic propagators, as done throughout this paper. This is illustrated in figure 3.17.

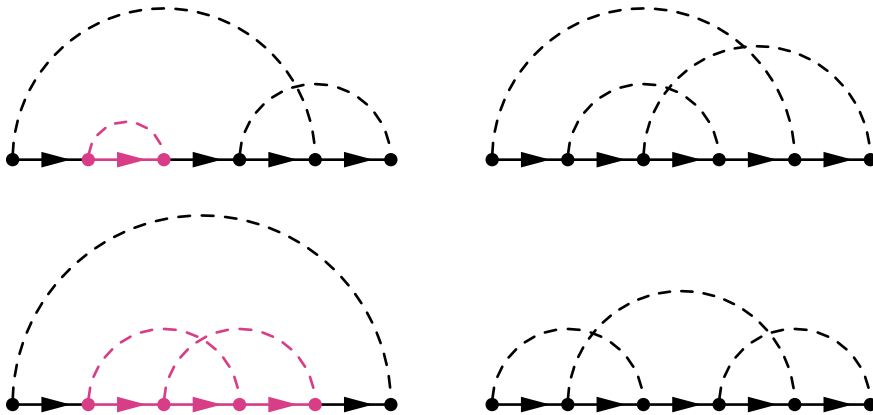


Figure 3.17: The diagrams to the right belong to the class of skeleton diagrams whilst the ones to the left merely belong to the class of proper self-energy diagrams. The insertions of the proper self-energy diagrams are here highlighted.

Even by restricting to merely a subset of skeleton diagrams, bounded by the diagram order $n \leq n_{\max}$, the range of diagrams contributing to \mathcal{G}_k will grow extremely fast with the bold-line iteration k . This will now be demonstrated in the case of $n_{\max} = 1$.

First iteration

$$\begin{aligned}
 S_1 &= \text{---} \bullet \text{---} \bullet \text{---} \\
 \mathcal{G}_1 &= \text{---} \text{---} \text{---} \\
 &= \text{---} \text{---} + \text{---} \bullet \text{---} \bullet \text{---} + \text{---} \bullet \text{---} \bullet \text{---} \bullet \text{---} \bullet \text{---} + \dots
 \end{aligned}
 \tag{3.52}$$

The diagrams are as follows:
 S_1 : A horizontal line with two black dots. A dashed arc connects the two dots above the line.
 \mathcal{G}_1 : A red arrow pointing to the right, formed by two parallel lines.
The expansion shows a sequence of diagrams: a single red arrow, followed by a red arrow with a dashed arc above it, followed by a red arrow with two dashed arcs above it, and so on.

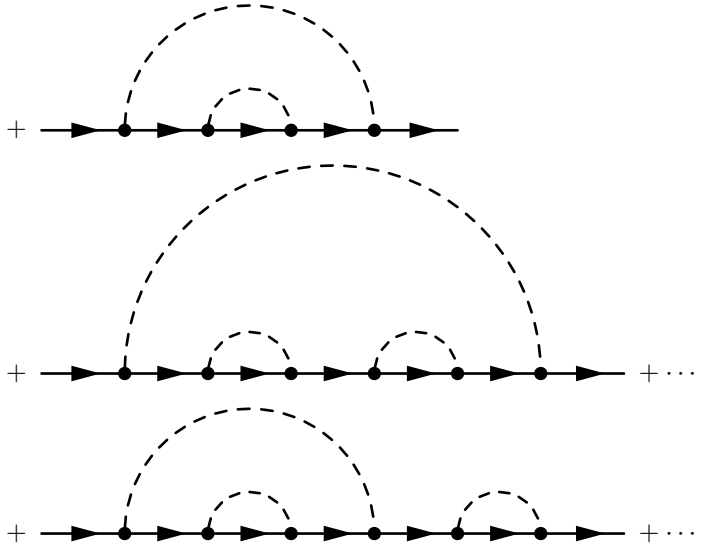
Second iteration

$$\begin{aligned}
 S_2 &= \text{---} \bullet \text{---} \bullet \text{---} \\
 \mathcal{G}_2 &= \text{---} \text{---} \text{---} \\
 &= \text{---} \text{---} + \text{---} \bullet \text{---} \bullet \text{---} + \text{---} \bullet \text{---} \bullet \text{---} \bullet \text{---} \bullet \text{---} + \dots
 \end{aligned}$$

The diagrams are as follows:
 S_2 : A horizontal line with two black dots. A dashed arc connects the two dots above the line.
 \mathcal{G}_2 : A blue arrow pointing to the right, formed by two parallel lines.
The expansion shows a sequence of diagrams: a single blue arrow, followed by a blue arrow with a dashed arc above it, followed by a blue arrow with two dashed arcs above it, and so on.

By substituting with \mathcal{G}_1 in terms of the diagram series (3.52) into the diagram series of \mathcal{G}_2 , this series, expressed in terms of the bare constituents, becomes

$$\mathcal{G}_2 = \mathcal{G}_1$$



Third iteration

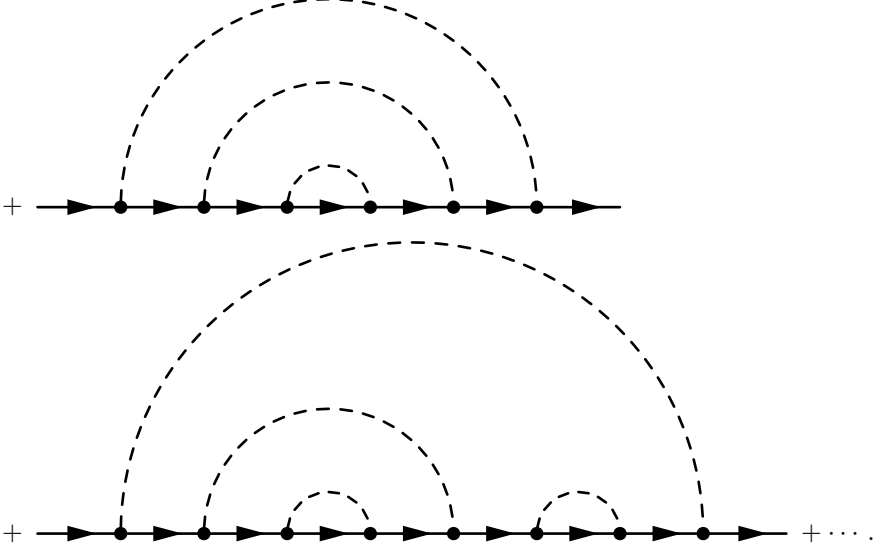
$$S_3 = \text{diagram with two dots, a dashed arc, and a magenta arrow pointing right}$$

$$\mathcal{G}_3 = \text{diagram with two dots and a blue arrow pointing right}$$

$$= \text{diagram with one dot and arrow} + \text{diagram with two dots, dashed arc, and blue arrow} + \text{diagram with three dots, two dashed arcs, and blue arrow} + \dots$$

Similarly to before, by substituting with \mathcal{G}_2 into \mathcal{G}_3 , one obtains

$$\mathcal{G}_3 = \mathcal{G}_2$$



Already at this point, a wide range of diagrams contribute to \mathcal{G}_3 . However, even if one continues this iterative process, a skeleton diagram in which the phonon propagators intersect won't be encountered in the series.

3.4.2 Implementation and update procedures

The diagram update procedures, for bold-line iterations $k > 1$, need to be altered in order to account for the replacement of the bare propagators within the diagram in favor of \mathcal{G}_k . However, rather than expressing \mathcal{G}_k in terms of the difference $\Delta\mathcal{G}_k$ to the bare propagator, it is more convenient to work with an additional imaginary phase $\varphi_k(\mathbf{p}, \tau)$, so that

$$\mathcal{G}_k(\mathbf{p}, \tau) = e^{\varphi_k(\mathbf{p}, \tau)} \mathcal{G}^{(0)}(\mathbf{p}, \tau). \quad (3.53)$$

This phase is defined through

$$\varphi(\mathbf{p}, \tau) = -\tau \Delta\xi_k(p_l, \tau_m) \quad (3.54)$$

where $\Delta\xi_k$ is an additional energy

$$\Delta\xi_k(\mathbf{p}_i, \tau_j) = \frac{1}{\tau_j} \log \frac{\mathcal{G}^{(0)}(\mathbf{p}_i, \tau_j)}{\mathcal{G}_k(\mathbf{p}_i, \tau_j)}. \quad (3.55)$$

In equation (3.54), p_l and τ_m are chosen to obey $p_l - \Delta p \leq p \leq p_l + \Delta p$ and $\tau_m - \Delta\tau \leq \tau \leq \tau_m + \Delta\tau$ respectively where the reader again is reminded of the definition

$\Delta x = \Delta x/2$. However, in the case of momentum magnitudes $p > p_{N-1} + \Delta p$, it is natural to use p_{N-1} . During the discretization it is then important to chose a large enough cutoff momentum p_{\max} in order for the true $G_k(\mathbf{p}, \tau)$ to be reasonably approximated by $e^{\varphi_k(\mathbf{p}, \tau)} \mathcal{G}^{(0)}(\mathbf{p}, \tau)$ at momentum magnitudes $p > p_{N-1} + \Delta p$. Otherwise \mathcal{G}_k might not converge to the true interacting propagator \mathcal{G} .

Now, with $\mathcal{G}_k(\mathbf{p}, \tau)$ defined in this way, the only modification needed in order for the update procedures to reflect the change $\mathcal{G}^{(0)} \rightarrow \mathcal{G}_k$, is to multiply the quotient of the diagram values D'/D with the factor

$$\frac{D'}{D} \rightarrow \frac{D'}{D} \exp \left\{ \sum_{a \in A} \varphi(\mathbf{p}_a, \tau_a) - \sum_{b \in B} \varphi(\mathbf{p}_b, \tau_b) \right\}. \quad (3.56)$$

Here B and A is the set of affected electronic propagators before and after the update procedure respectively.

But wait, there is more. Update procedures involving the sampling of imaginary times from an exponential distribution with momentum dependent rate parameter must further be slightly modified in order to improve the otherwise disastrous statistics. This since the quota $W(\tau'_l|\tau_l)/W(\tau_l|\tau'_l) = \exp\{-\lambda(\tau_l - \tau'_l)\}$, for certain differences $\tau_l - \tau'_l$, poorly mimics the ratio $D(\tau'_l)/D(\tau_l)$ due to the choice of rate parameter $\lambda(\mathbf{p})$. This is easily realized by comparing the $\mathcal{G}(\mathbf{p}, \tau)$'s in figure 3.11 to their corresponding bare propagators $\mathcal{G}^{(0)}(\mathbf{p}, \tau)$. In order to resolve this issue, one adds to the the original rate parameter the contribution $\Delta\lambda_k(\mathbf{p}_l)$, which is obtained by fitting an exponentially decaying function $C_k(\mathbf{p}_l) \exp\{-\Delta\lambda_k(\mathbf{p}_l) \tau\}$ to $\mathcal{G}_k(\mathbf{p}_l, \tau_j)/\mathcal{G}^{(0)}(\mathbf{p}_l, \tau_j)$ for each $p_l - \Delta p \leq p \leq p_l + \Delta p$. In the case of a momentum magnitude $p > p_{N-1} + \Delta p$ the $\Delta\lambda$ corresponding to p_{N-1} is used.

Finally, after each bold-line iteration, when calculating the value of $S_{k+1}(\mathbf{p}_i, \tau_j)$ from $N_{i,j}$, it is important to normalize using \mathcal{G}_k rather than the bare propagator $\mathcal{G}^{(0)}$. Hence, in similarity with (3.40),

$$S_{k+1}(\mathbf{p}_i, \tau_j) = N_{i,j} \frac{\sum_{l,m} \mathcal{G}_k(\mathbf{p}_l, \tau_m)}{N_0}, \quad (3.57)$$

but the only diagrams allowed to contribute to the histogram are this time the skeleton ones.

3.4.3 Results

Nine different simulations for an increasing value of the maximum diagram order n_{\max} have been carried out using the discretization $\Delta\tau = 0.02$, $\Delta p = 0.02$, $p_{\max} = 10$ and $\tau_{\max} = 60$. Depicted in figures 3.18-3.26 are the resulting values S_k 's, as well as the corresponding \mathcal{G}_k 's. The true value of the proper self-energy Σ^* and the Greens function \mathcal{G} are also outlined for comparison.

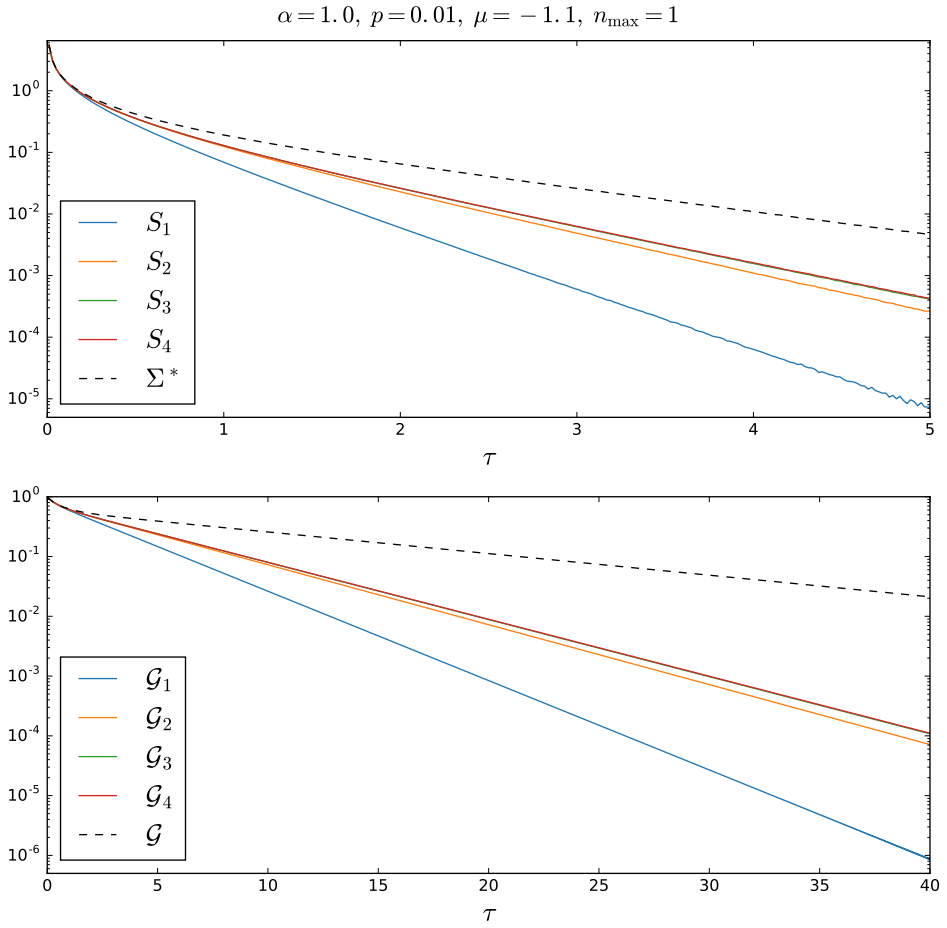


Figure 3.18: A total core time of 13 days was used for each of the four iterations in the bold-line scheme.

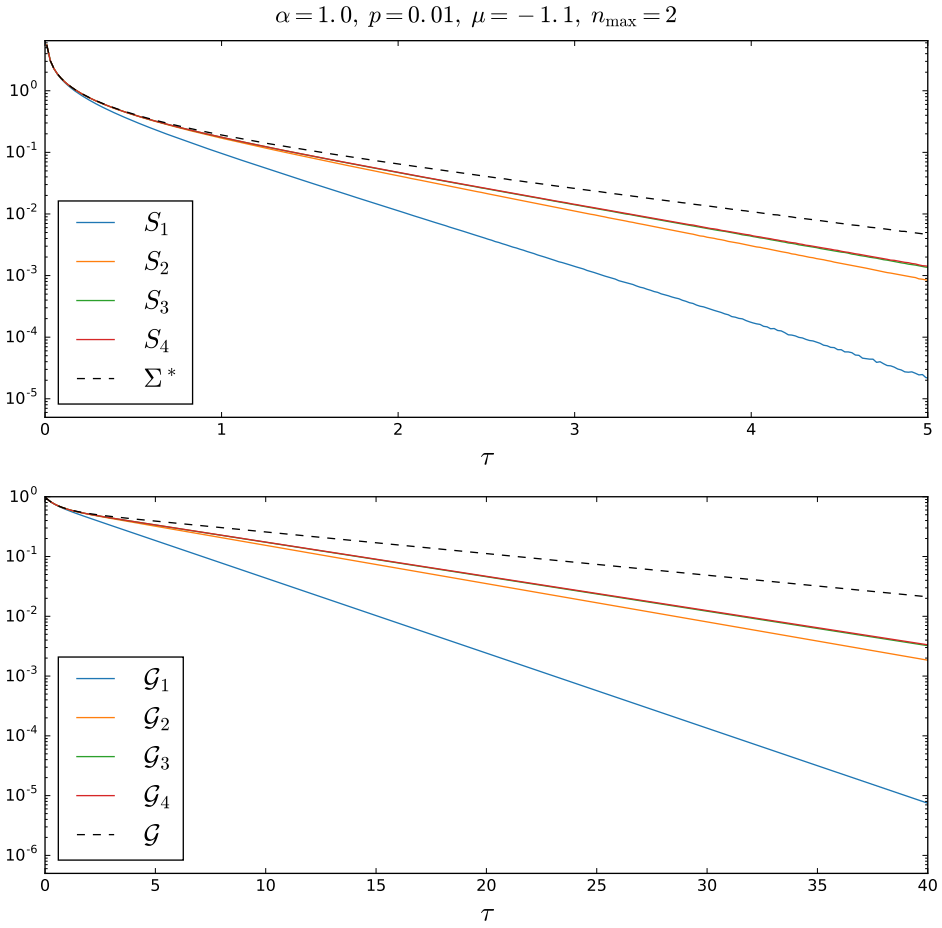


Figure 3.19: A total core time of 13 days was used for each of the four iterations in the bold-line scheme.

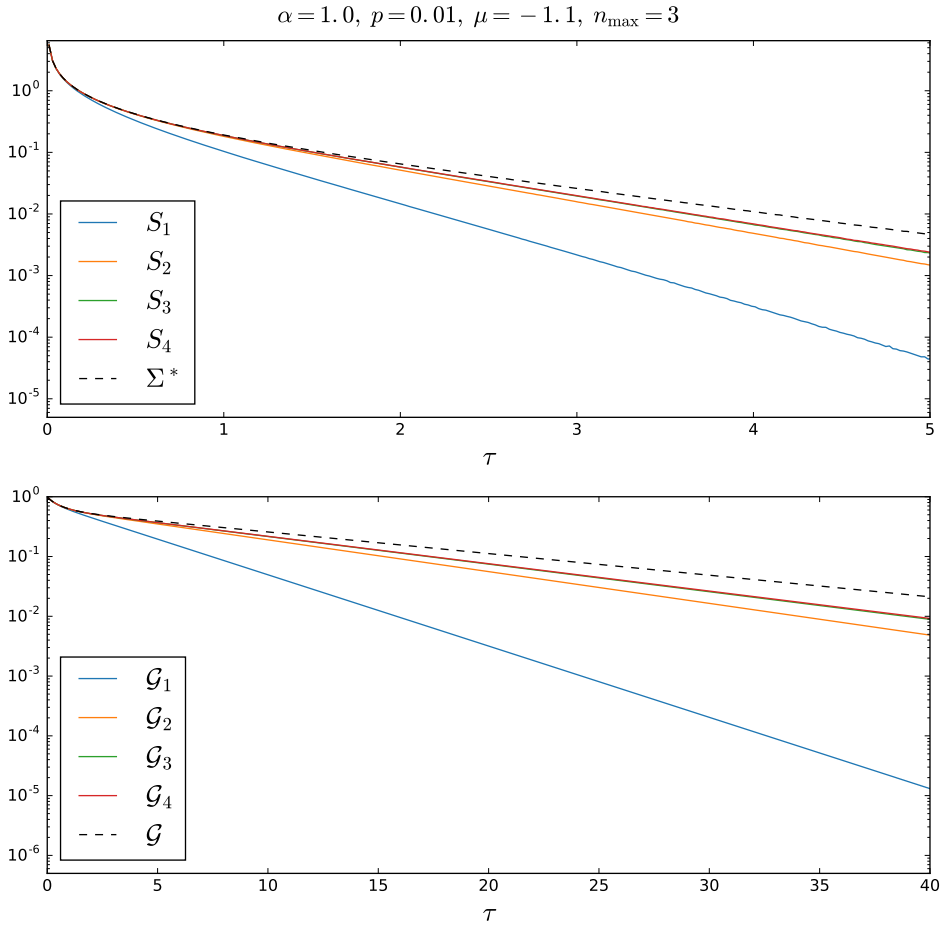


Figure 3.20: A total core time of 15 days was used for each of the four iterations in the bold-line scheme.

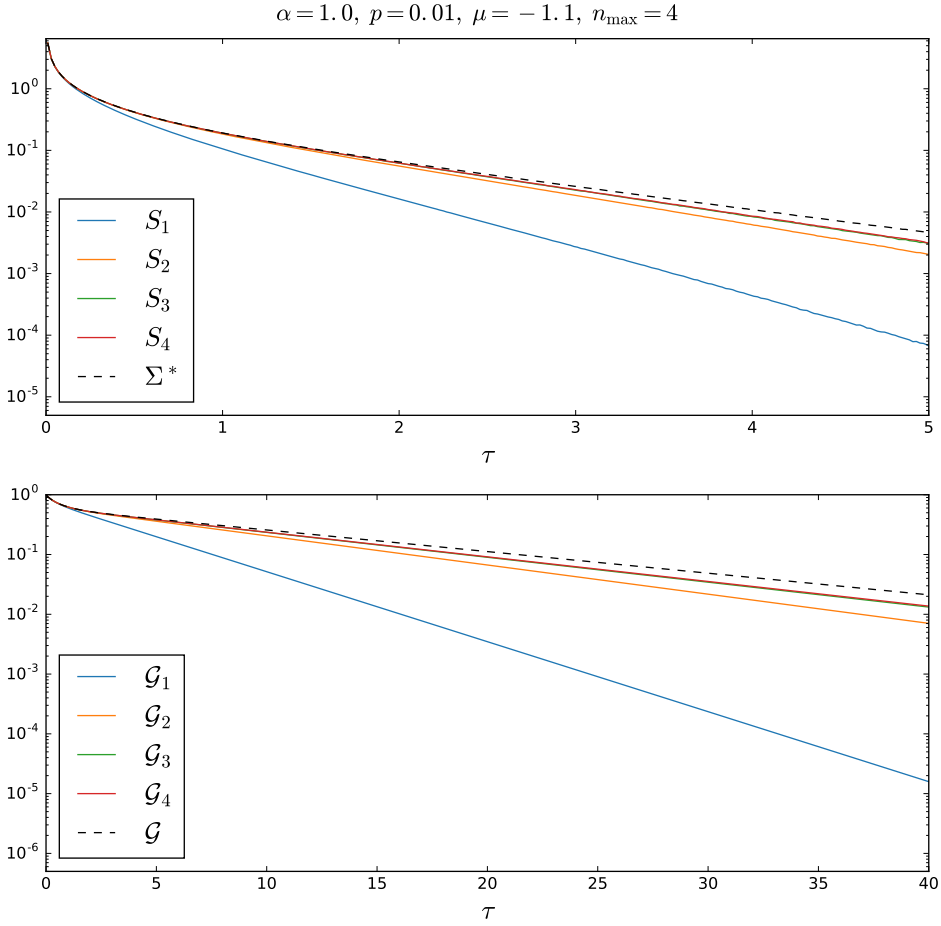


Figure 3.21: A total core time of 15 days was used for each of the four iterations in the bold-line scheme.

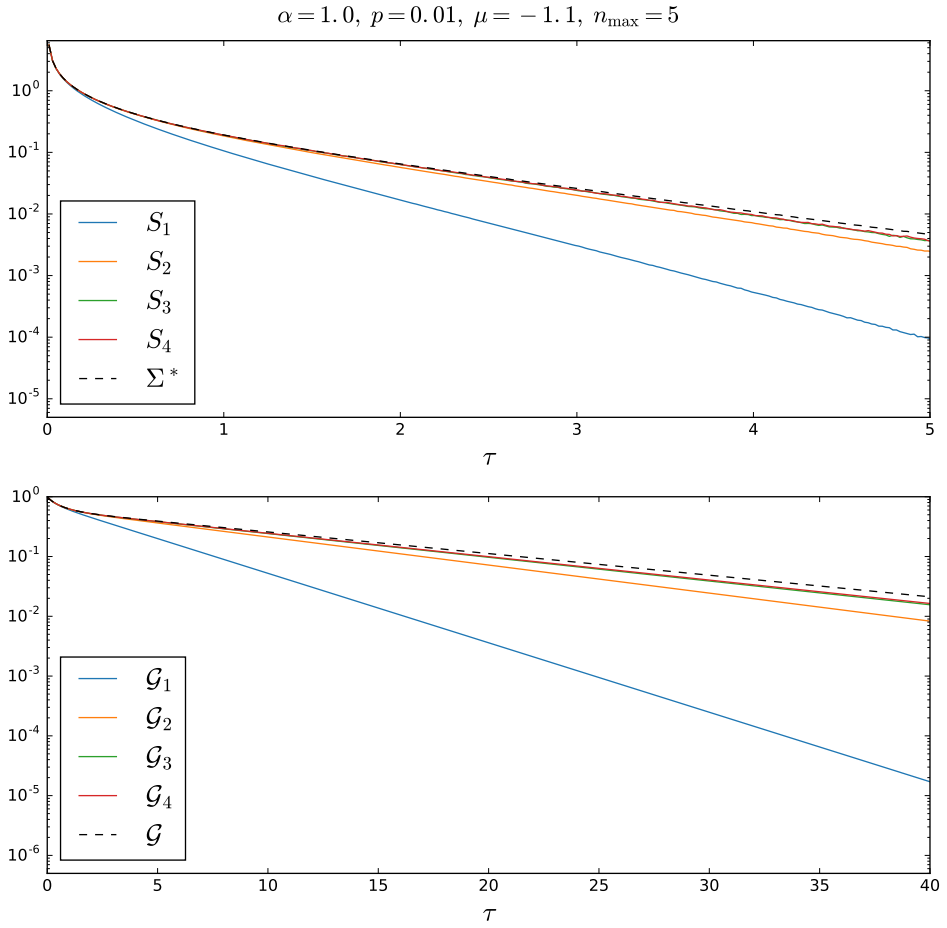


Figure 3.22: A total core time of 15 days was used for each of the four iterations in the bold-line scheme.

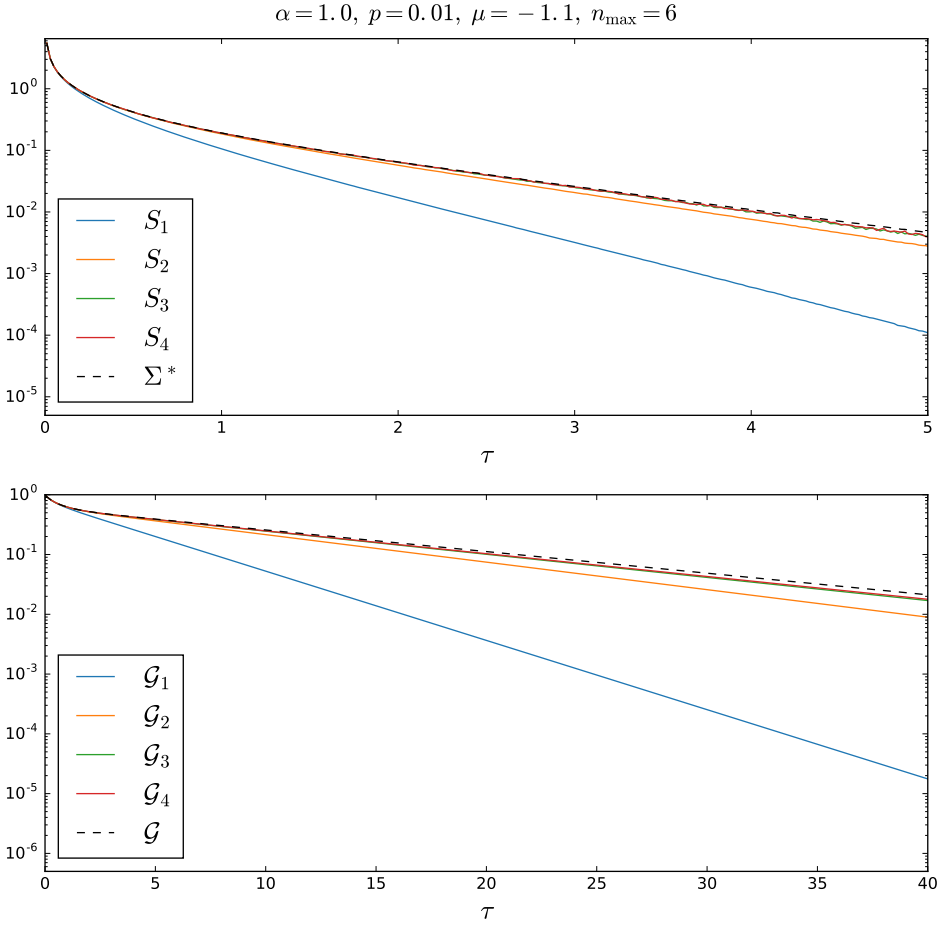


Figure 3.23: A total core time of 28 days was used for each of the four iterations in the bold-line scheme.

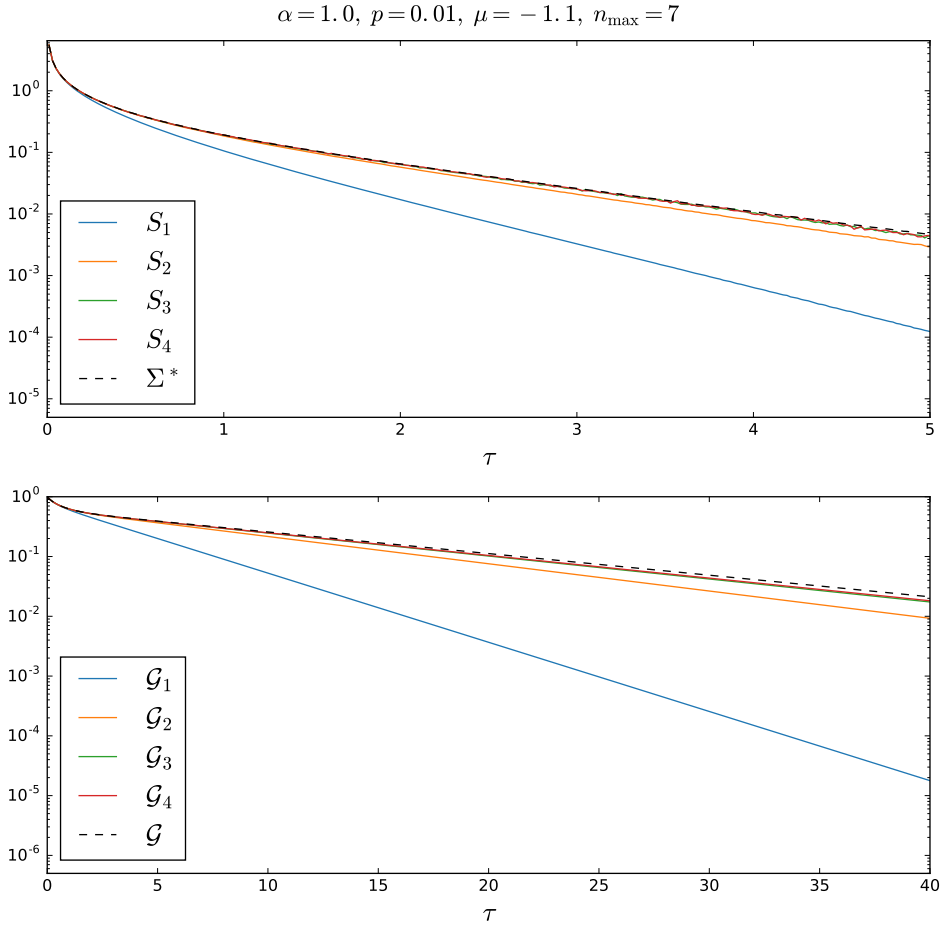


Figure 3.24: A total core time of 44 days was used for each of the four iterations in the bold-line scheme.

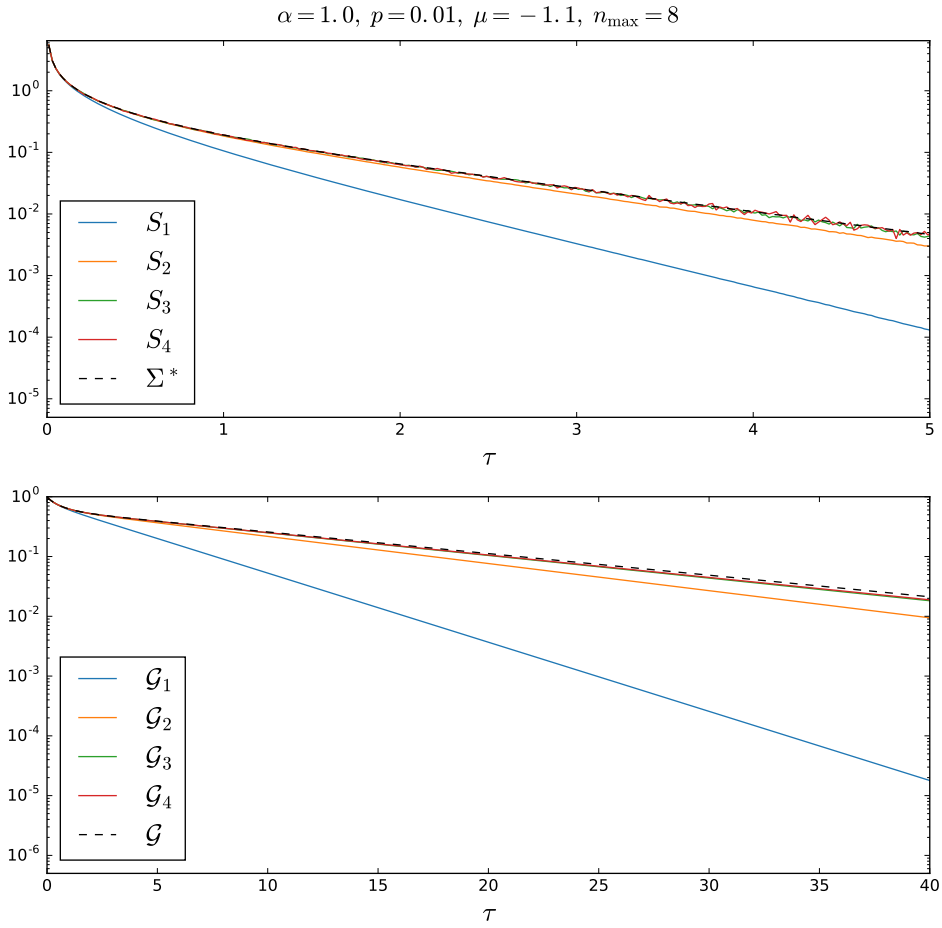


Figure 3.25: A total core time of 65 days was used for each of the four iterations in the bold-line scheme.

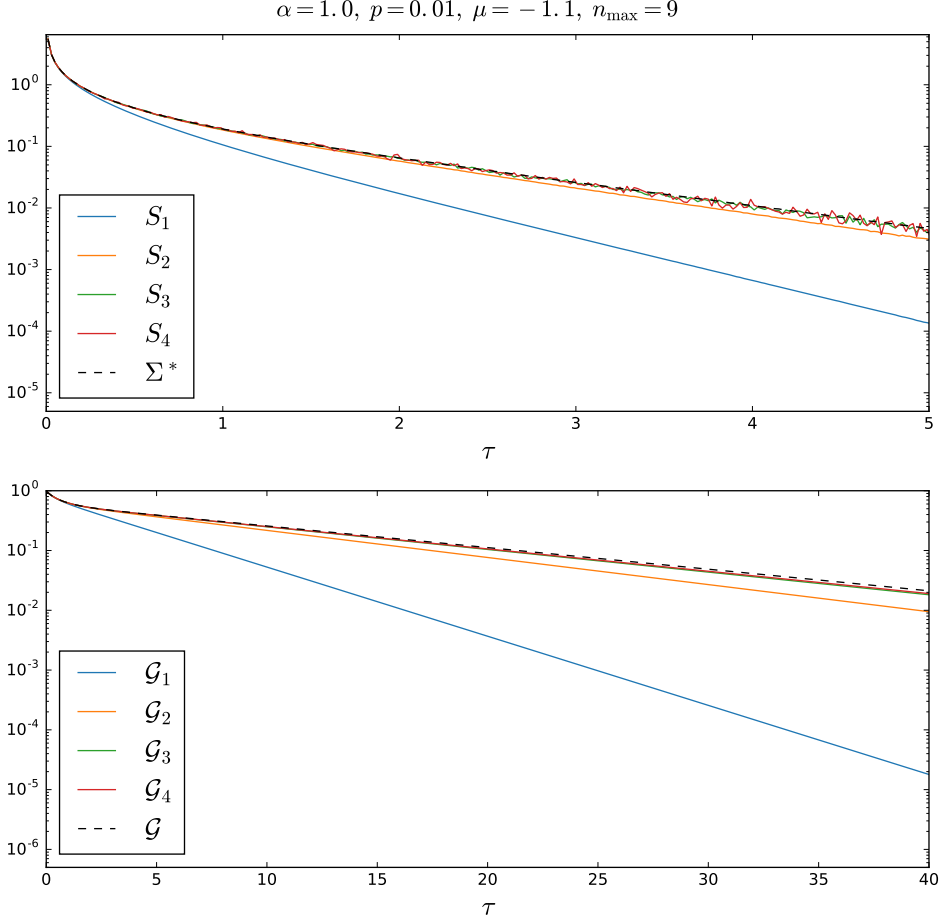


Figure 3.26: A total core time of 203 days was used for each of the four iterations in the bold-line scheme.

Evident from these figures is that S_k and \mathcal{G}_k approaches Σ^* and \mathcal{G} respectively when increasing k and n_{\max} , which is expected. However, for larger n_{\max} the statistics becomes more and more influenced by noise. The reason being that diagrams of higher order are more frequently sampled in the Monte Carlo process when \mathcal{G}_k is starting to approach the true \mathcal{G} . Hence the ration $N_{i,j}/N_0$ in equation (3.57) grows so that fluctuations within $N_{i,j}$ no longer will be suppressed in the same extent. But since the amplitude of statistical noise is inversely proportional to the square root of computation time, this noise is reduced simply by running the simulations for longer times. However it was realized that the computation time required for larger n_{\max} quickly outgrew what was possible to achieve by a single core in a fore-

seeable future, forcing the program to be parallelized using the *Message Passing Interface*. Once implemented this allowed for an immense amount of computation time to be spent performing the bold-line scheme for larger n_{\max} . Although, by inspecting figure 3.25 and 3.26 it is evident that this computation time still was not enough.

By performing a linear regression of $\log \mathcal{G}_k$ one can extract the $E_0(n_{\max}, k)$ and $Z_0(n_{\max}, k)$ according (2.19). This has been done and the result is presented in figures 3.27 and 3.28.

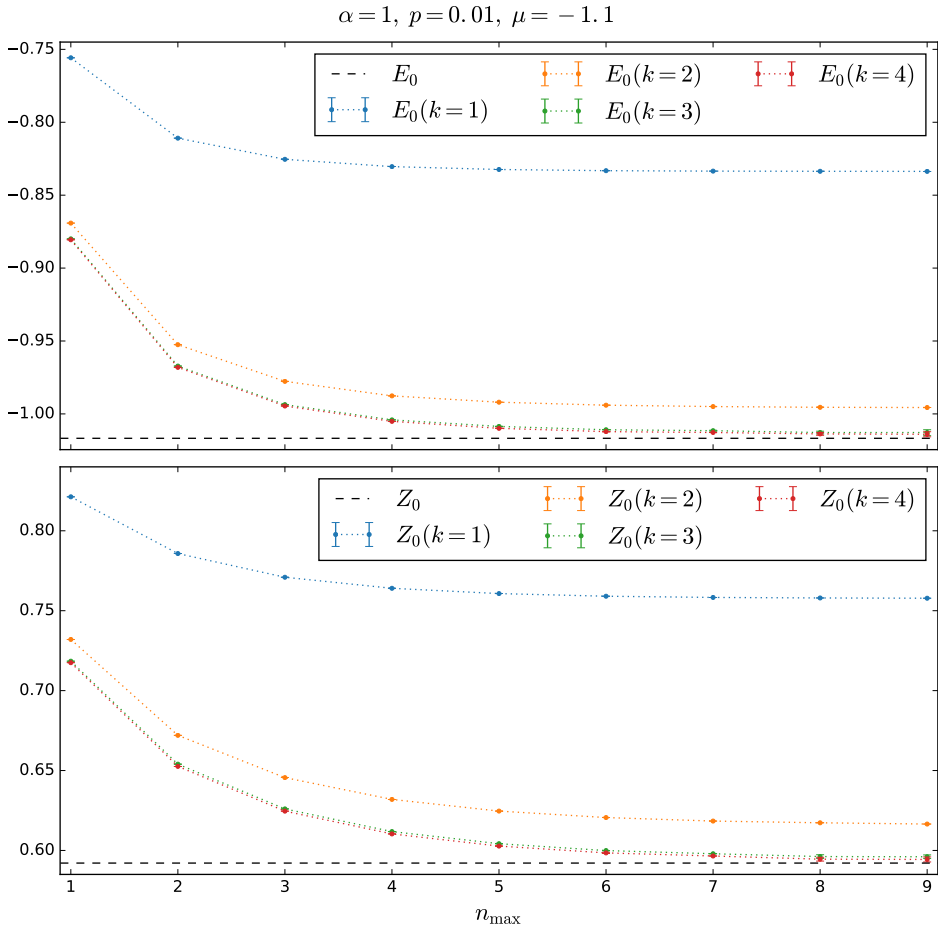


Figure 3.27: Here $E_0(n_{\max}, k)$ and $Z_0(n_{\max}, k)$ obtained from the bold-line simulations are shown next to the true values E_0 and Z_0 .

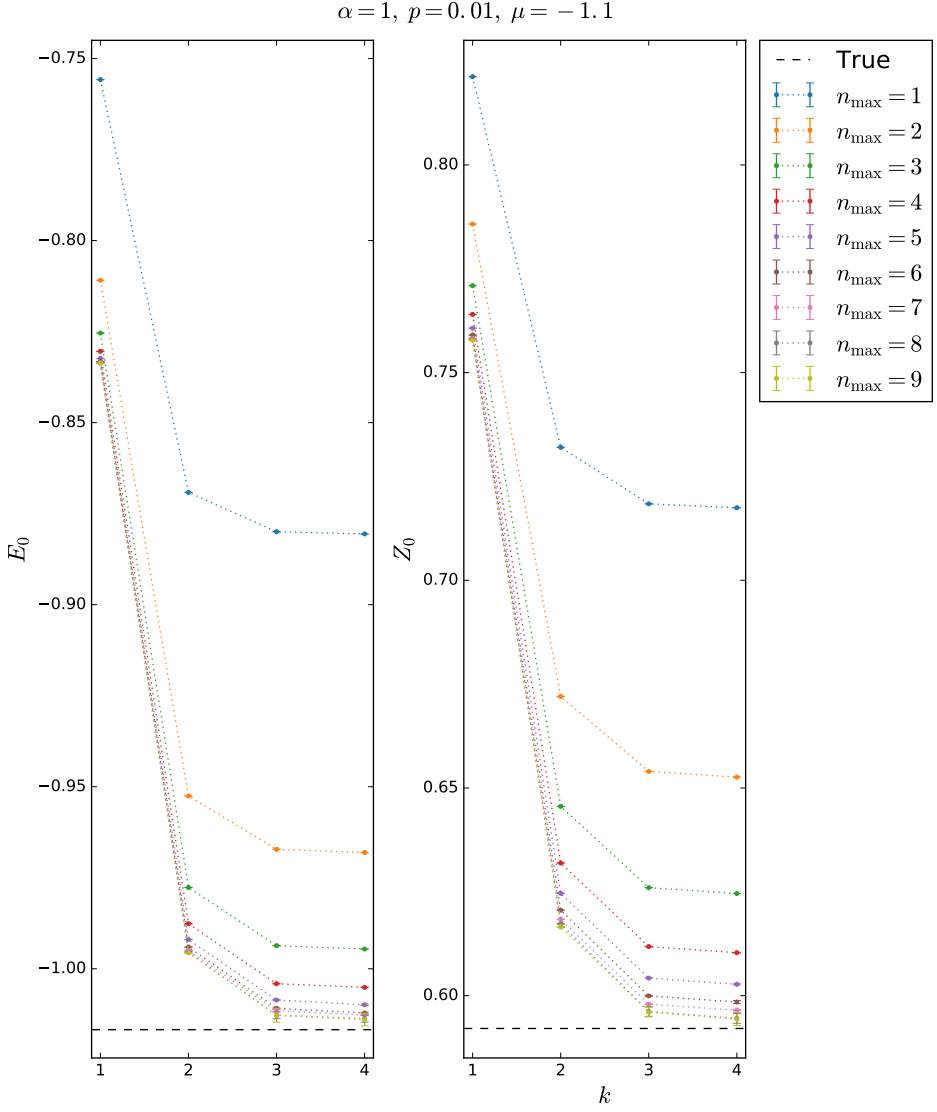


Figure 3.28: Here $E_0(n_{\max}, k)$ and $Z_0(n_{\max}, k)$ obtained from the bold-line simulations are shown next to the true values E_0 and Z_0 .

Unfortunately there was only four iterations used in the bold-line scheme, which according to figure 3.28 was not enough in order to reach a steady state value for E_0 and Z_0 . Nevertheless could this steady state not have been very far away, a fifth or perhaps a sixth iteration should probably have been sufficient for the trends to

level out. Additionally it would also have been necessary to simulate using larger n_{\max} in pursuance of convergence with the true E_0 and Z_0 . But since this would have required a monstrous amount of computation time in order for the error bars to shrink to a satisfactory size it was not carried out.

Even with these shortcomings, it is from the presented result, apparent that $E_0(n_{\max}, k)$ and $Z_0(n_{\max}, k)$ approach the true values as n_{\max} and k are increased.

3.5 Numerical Results of E_0 and Z_0

Here numerous \mathcal{G} 's have been computed through bare scheme simulations of Σ^* and E_0 and Z_0 extracted from the former. The result is presented in figures 3.29 and 3.30 but also in table 3.4. The computation time for each data point range from two to twelve core hours, providing a uncertainty of less than $5 \cdot 10^{-4}$. Further more the results are in good agreement with the ones obtained by Prokof'ev et al. [5, 19]. For comparison these numerically computed quantities are presented next to corresponding ones obtained using traditional analytical perturbative methods [2, 3, 5, 20]

$$\begin{aligned}
 E_0^{(1)}(p, \alpha) &= \frac{p^2}{2} - \alpha \frac{\sqrt{2}}{p} \arcsin \frac{p}{\sqrt{2}} \\
 E_0^{(2)}(p, \alpha) &= \frac{p^2}{2m^*} - \alpha - \frac{2}{3} \left(\frac{1}{8} - \frac{1}{3\pi} \right) \alpha^2, \quad m^* = \frac{1}{1 - \alpha/6} \\
 Z_0^{(1)}(p=0, \alpha) &= 1 - \frac{\alpha}{2}.
 \end{aligned} \tag{3.58}$$

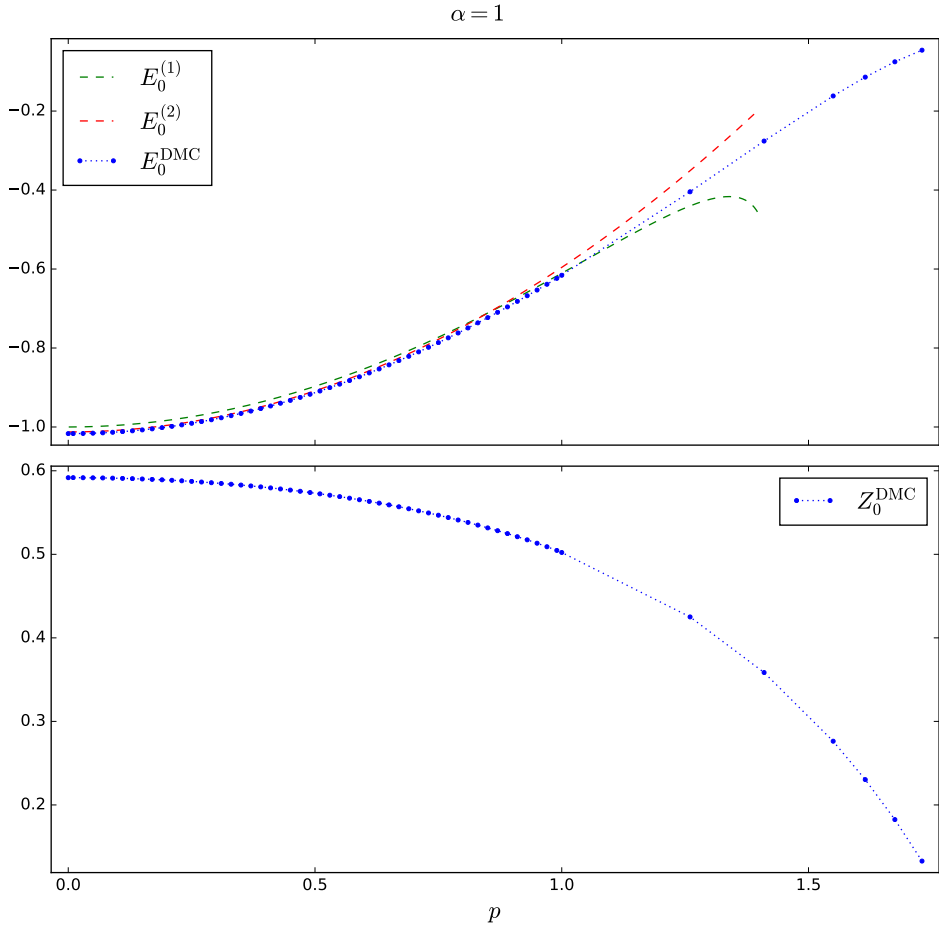


Figure 3.29: Here the numerically obtained E_0^{DMC} and Z_0^{DMC} are plotted against the external momentum magnitude p at $\alpha = 1$. The error bars are here omitted since they would not have been visible due to the low uncertainty.

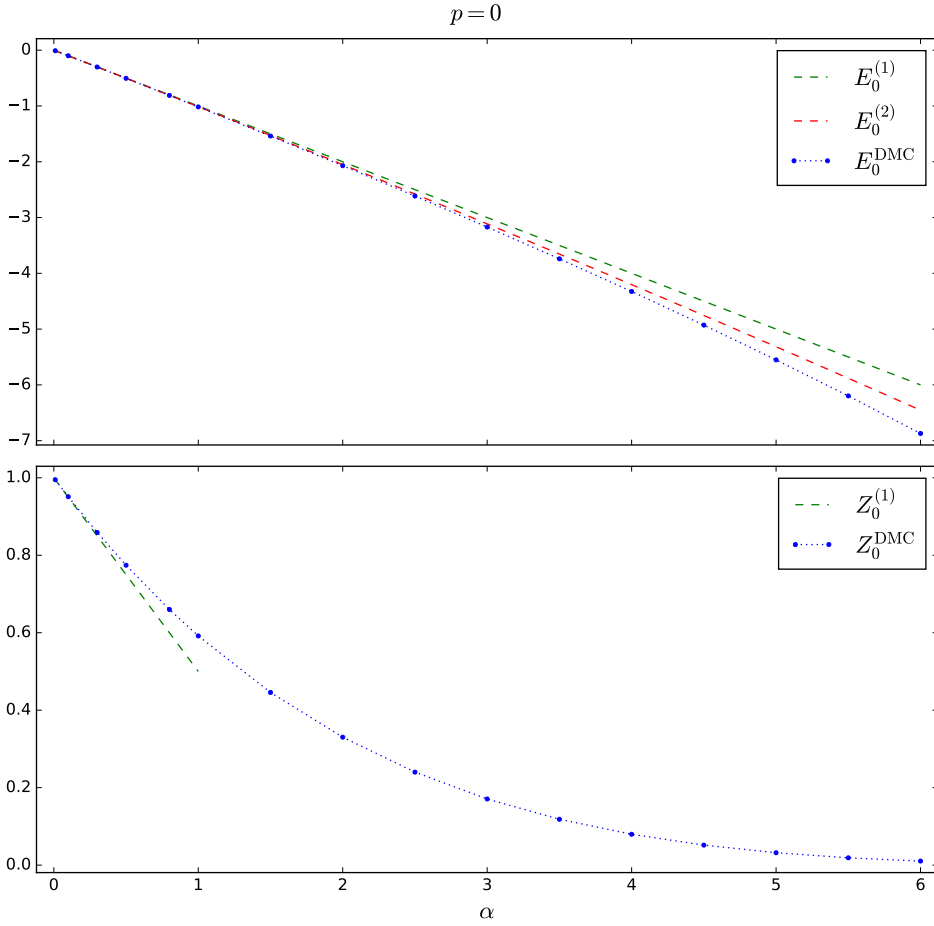


Figure 3.30: Here the numerically obtained E_0^{DMC} and Z_0^{DMC} are plotted against the interaction parameter α at $p = 0$. The error bars are here omitted since they would not have been visible due to the low uncertainty.

$\alpha = 1$			$p = 0$		
p	E_0^{DMC}	Z_0^{DMC}	α	E_0^{DMC}	Z_0^{DMC}
0	-1.0168	0.5918	0.01	-0.0100	0.9950
0.11	-1.0117	0.5909	0.1	-0.1002	0.9511
0.21	-0.9984	0.5886	0.3	-0.3015	0.8590
0.33	-0.9714	0.5839	0.5	-0.5041	0.7743
0.45	-0.9326	0.5769	0.8	-0.8107	0.6600
0.55	-0.8915	0.5691	1	-1.0168	0.5918
0.67	-0.8320	0.5569	1.5	-1.5389	0.4458
0.79	-0.7619	0.5411	2	-2.0711	0.3303
0.89	-0.6959	0.5248	2.5	-2.6147	0.2401
1	-0.6158	0.5022	3	-3.1705	0.1708
1.26	-0.4044	0.4251	3.5	-3.7403	0.1184
1.41	-0.2760	0.3585	4	-4.3256	0.0797
1.55	-0.1618	0.2763	4.5	-4.9284	0.0516
1.615	-0.1141	0.2303	5	-5.5514	0.0320
1.675	-0.0753	0.1825	5.5	-6.1976	0.0188
1.73	-0.0458	0.1328	6	-6.8709	0.0104

Table 3.4: Some of the data from figures 3.29 and 3.30.

Chapter 4

Summary and conclusions

The main focus of this thesis has been to investigate three types DMC schemes for numerically simulating the electronic single-particle Green's function of the Fröhlich Hamiltonian, also known as the Fröhlich polaron. To achieve this a program has been written in c++ which has used the Message Passing Interface in order to parallelize the code over several cores. The numerical results presented in this thesis are entirely obtained using this program.

The difference in results between the two bare schemes, one calculating \mathcal{G} and the other one the proper self-energy Σ^* of the former, is presented in figure 3.16. From this figure it is evident that the difference is decreasing with a finer discretization, i.e. a smaller $\Delta\tau$, as expected. One should also mention that the high frequency noise present in the data in this figure originates from the \mathcal{G} 's which have not been obtained using Dyson equation. As mentioned in section 3.3.4, any such noise present in $\Sigma^*(\mathbf{p}, \tau)$ will be greatly suppressed when undergoing Dyson equation.

The bold-line scheme, which is making use of Dyson equation self-consistently did not perform as well as the bare schemes. The main reason for this being the extremely poor statistics when starting to converge with the true Green's function, as is evident from figures 3.25 and 3.26. Once again the high frequency noise is seen to have been reduced significantly when comparing \mathcal{G}_k to S_k due to Dyson equation. However, the noise present in S_k was so substantial that it no longer merely made an impact to the high frequency parts of the spectrum, but lower frequency parts were also largely affected. As low frequency noise is not suppressed as much as noise of higher frequencies when performing Dyson equation, this low frequency noise made an small but noticeable imprint on the Green's function once back in the τ -space. This is what caused the relatively large uncertainty for the quantities corresponding to $n_{\max} = 8, 9$ in figures 3.27 and 3.28.

Without somehow being able to improve the statistics, it would not be meaningful to continue the bold-line scheme for larger n_{\max} since the computational cost in order to reduce the noise would be enormous (a total of 812 core days was already spent for the simulation using $n_{\max} = 9$). As mentioned in section 3.4.3,

the poor statistics arose from the fact that very little time was spent at the zeroth order diagram. Therefore the fluctuations present in the histogram N could not be reduced when divided by N_0 in (3.57). To partly resolve this one could probably have redefined $\alpha \rightarrow \alpha' = \alpha f(n)$ where $f(n) \leq 1$ would be a function of the diagram order n so that it would be less aspiring for the Markov process to sample higher order diagrams. Knowing the expression for $f(n)$ one could then have extrapolated the obtained result to the case of $f(n) = 1$ and in this way acquire result with less noise.

Even without the perfect data it would be surprising, considering figures 3.27 and 3.28, if E_0 and Z_0 of the bold-line scheme would not converge to the true values as n_{\max} and the bold-line iteration k were increased. If improvements to the code was made and this achieved, it would have been interesting to look at the effects of the discretization also for this scheme.

Pleased with the overall agreement between the different DMC schemes, both the energy E_0 and the Z_0 -factor of the polaron was computed as functions of external momentum \mathbf{p} and interaction parameter α . Since the bare scheme for Σ^* was deemed as best performing, this was the one used. The result turned out to be in excellent agreement with previous obtained data [5, 19].

During this thesis the dispersion relation of the phonons has been assumed to be dispersionless. But how would a different dispersion relation, one which is not dispersionless, affect the quantities E_0 and Z_0 ? This would have been interesting to investigate, if more time would have been available.

Bibliography

- [1] A. S. Alexandrov and J. T. Devreese, *Advances in Polaron Physics (Springer Series in Solid-State Sciences)* (Springer, 2009).
- [2] H. Fröhlich, *Electrons in lattice fields*, *Advances in Physics* **3**, 325 (1954).
- [3] R. P. Feynman, *Statistical Mechanics: A Set Of Lectures (Advanced Books Classics)* (Westview Press, 1998).
- [4] G. Iadonisi, *Polarons in Bulk Materials and Systems with Reduced Dimensionality* (IOS Press, 2006).
- [5] A. Mishchenko *et al.*, *Diagrammatic quantum Monte Carlo study of the Fröhlich polaron*, *Physical Review B* **62**, 6317 (2000).
- [6] N. Prokof'ev and B. Svistunov, *Fermi-polaron problem: Diagrammatic Monte Carlo method for divergent sign-alternating series*, *Phys. Rev. B* **77**, 020408 (2008).
- [7] E. Kozik *et al.*, *Diagrammatic Monte Carlo for correlated fermions*, *EPL (Europhysics Letters)* **90**, 10004 (2010).
- [8] E. Burovski *et al.*, *Diagrammatic quantum Monte Carlo for two-body problems: applied to excitons*, *Physical Review Letters* **87**, 186402 (2001).
- [9] S. Kulagin *et al.*, *Bold diagrammatic Monte Carlo technique for frustrated spin systems*, *Physical Review B* **87**, 024407 (2013).
- [10] H. Wimmel, *Quantum Physics & Observed Reality: A Critical Interpretation of Quantum Mechanics* (World Scientific Pub Co Inc, 1992).
- [11] A. L. Fetter and J. D. Walecka, *Quantum Theory of Many-Particle Systems* (Dover Publications, 2003).
- [12] A. A. Abrikosov, L. P. Gorkov and I. E. Dzyaloshinski, *Methods of Quantum Field Theory in Statistical Physics (Dover Books on Physics)* (Dover Publications, 2012).

- [13] T. Matsubara, *A New Approach to Quantum-Statistical Mechanics*, Progress of Theoretical Physics **14**, 351 (1955).
- [14] H. Goldstein, *Classical Mechanics (Addison-Wesley series in physics)* (Addison-Wesley, 1980).
- [15] K. Binder, *Monte Carlo Methods in Statistical Physics (Topics in Current Physics)*, Second edition. ed. (Springer, 1986).
- [16] M. E. J. Newman and G. T. Barkema, *Monte Carlo Methods in Statistical Physics* (Clarendon Press, 1999).
- [17] N. Prokof'ev and B. Svistunov, *Bold Diagrammatic Monte Carlo Technique: When the Sign Problem Is Welcome*, Phys. Rev. Lett. **99**, 250201 (2007).
- [18] R. Mattuck, *A Guide to Feynman Diagrams in the Many-Body Problem: Second Edition* Dover Books on Physics (Dover Publications, 2012).
- [19] N. V. Prokof'ev and B. V. Svistunov, *Polaron Problem by Diagrammatic Quantum Monte Carlo*, Phys. Rev. Lett. **81**, 2514 (1998).
- [20] E. Haga, *Note on the Slow Electrons in a Polar Crystal*, Progress of Theoretical Physics **11**, 449 (1954).